

REPORT DOCUMENTATION PAGE			Form Approved OMB NO. 0704-0188		
<p>The public reporting burden for this collection of information is estimated to average 1 hour per response, including the time for reviewing instructions, searching existing data sources, gathering and maintaining the data needed, and completing and reviewing the collection of information. Send comments regarding this burden estimate or any other aspect of this collection of information, including suggestions for reducing this burden, to Washington Headquarters Services, Directorate for Information Operations and Reports, 1215 Jefferson Davis Highway, Suite 1204, Arlington VA, 22202-4302. Respondents should be aware that notwithstanding any other provision of law, no person shall be subject to any penalty for failing to comply with a collection of information if it does not display a currently valid OMB control number.</p> <p>PLEASE DO NOT RETURN YOUR FORM TO THE ABOVE ADDRESS.</p>					
1. REPORT DATE (DD-MM-YYYY) 06-10-2014		2. REPORT TYPE Ph.D. Dissertation		3. DATES COVERED (From - To) -	
4. TITLE AND SUBTITLE Volume phase masks in photo-thermo-refractive glass			5a. CONTRACT NUMBER W911NF-10-1-0441		
			5b. GRANT NUMBER		
			5c. PROGRAM ELEMENT NUMBER		
6. AUTHORS Marc. A. Segall			5d. PROJECT NUMBER		
			5e. TASK NUMBER		
			5f. WORK UNIT NUMBER		
7. PERFORMING ORGANIZATION NAMES AND ADDRESSES University of Central Florida 12201 Research Parkway, Suite 501  Orlando, FL 32826 -3246			8. PERFORMING ORGANIZATION REPORT NUMBER		
9. SPONSORING/MONITORING AGENCY NAME(S) AND ADDRESS (ES) U.S. Army Research Office P.O. Box 12211 Research Triangle Park, NC 27709-2211			10. SPONSOR/MONITOR'S ACRONYM(S) ARO		
			11. SPONSOR/MONITOR'S REPORT NUMBER(S) 58500-EL-HEL.26		
12. DISTRIBUTION AVAILABILITY STATEMENT Approved for public release; distribution is unlimited.					
13. SUPPLEMENTARY NOTES The views, opinions and/or findings contained in this report are those of the author(s) and should not be construed as an official Department of the Army position, policy or decision, unless so designated by other documentation.					
14. ABSTRACT In many applications such as beam shaping, mode conversion, and phase encoding it is necessary to alter the spatial phase profile of a beam via a phase mask. Conventional techniques to accomplish this either involve surface relief profiling in thin films such as PMMA or refractive index modulation in bulk photorefractive crystals such as lithium niobate. These materials have been used extensively for the past several decades and perform admirably in low power conditions. However, in high power systems these materials will be destroyed, requiring a new means of producing phase masks. In this dissertation a method for producing robust phase masks in the bulk of photo-					
15. SUBJECT TERMS photothermorefractive glass, volume hologram, volume phase mask					
16. SECURITY CLASSIFICATION OF:			17. LIMITATION OF ABSTRACT UU	15. NUMBER OF PAGES	19a. NAME OF RESPONSIBLE PERSON Leonid Glebov
a. REPORT UU	b. ABSTRACT UU	c. THIS PAGE UU			19b. TELEPHONE NUMBER 407-823-6983

## **Report Title**

Volume phase masks in photo-thermo-refractive glass

### **ABSTRACT**

In many applications such as beam shaping, mode conversion, and phase encoding it is necessary to alter the spatial phase profile of a beam via a phase mask. Conventional techniques to accomplish this either involve surface relief profiling in thin films such as PMMA or refractive index modulation in bulk photorefractive crystals such as lithium niobate. These materials have been used extensively for the past several decades and perform admirably in low power conditions. However, in high power systems these materials will be destroyed, requiring a new means of producing phase masks. In this dissertation a method for producing robust phase masks in the bulk of photo-thermo-refractive glass is developed and successfully demonstrated.

Three main applications of phase masks were studied in detail. The first is mode conversion, where binary phase masks convert a Gaussian beam to higher order modes. The second is beam shaping, where phase masks are used as focusing elements and for optical vortex generation. Near-theoretical conversion efficiency was achieved for all elements in these cases. The third application is aberration analysis and correction. Here the degradation of volume Bragg gratings recorded in an aberrated holographic system was modeled, with the simulations indicating that correcting elements are generally necessary for high-quality production of gratings. Corrective phase masks are designed which can selectively correct one or multiple aberrations of varying magnitudes are shown.

A new type of optical element is also developed in which a phase mask is encoded into a transmitting Bragg grating. This technique combines the local phase modulation of a phase mask with the multiplexing ability of transmitting Bragg gratings, allowing for multiple phase masks to be recorded in a single element. These masks may be used at any wavelength satisfying the Bragg condition, increasing the useful wavelength regime of a single element by orders of magnitude.

VOLUME PHASE MASKS IN PHOTO-THERMO-REFRACTIVE GLASS

by

MARC A. SEGALL

B.S. Bucknell University, 2007

M.S. University of Central Florida, 2009

A dissertation submitted in partial fulfillment of the requirements  
for the degree of Doctor of Philosophy  
in the College of Optics & Photonics  
at the University of Central Florida  
Orlando, Florida

Fall Term  
2013

Major Professor: Leonid B. Glebov

## ABSTRACT

In many applications such as beam shaping, mode conversion, and phase encoding it is necessary to alter the spatial phase profile of a beam via a phase mask. Conventional techniques to accomplish this either involve surface relief profiling in thin films such as PMMA or refractive index modulation in bulk photorefractive crystals such as lithium niobate. These materials have been used extensively for the past several decades and perform admirably in low power conditions. However, in high power systems these materials will be destroyed, requiring a new means of producing phase masks. In this dissertation a method for producing robust phase masks in the bulk of photo-thermo-refractive glass is developed and successfully demonstrated.

Three main applications of phase masks were studied in detail. The first is mode conversion, where binary phase masks convert a Gaussian beam to higher order modes. The second is beam shaping, where phase masks are used as focusing elements and for optical vortex generation. Near-theoretical conversion efficiency was achieved for all elements in these cases. The third application is aberration analysis and correction. Here the degradation of volume Bragg gratings recorded in an aberrated holographic system was modeled, with the simulations indicating that correcting elements are generally necessary for high-quality production of gratings. Corrective phase masks are designed which can selectively correct one or multiple aberrations of varying magnitudes are shown.

A new type of optical element is also developed in which a phase mask is encoded into a transmitting Bragg grating. This technique combines the local phase modulation of a phase mask with the multiplexing ability of transmitting Bragg gratings, allowing for multiple phase masks to be recorded in a single element. These masks may be used at any wavelength

satisfying the Bragg condition, increasing the useful wavelength regime of a single element by orders of magnitude.

## ACKNOWLEDGMENTS

I would like to thank the numerous people who assisted in my research. Leonid Glebov was very helpful in explaining concepts, which aided me in trying to determine how to devise new optical elements. Boris Zeldovich taught me many mathematical techniques which were invaluable in designing my simulations, and the Stokes Advanced Research Computing Center provided the computational resources to actually run them. Vasile Rotar and Julien Lumeau helped me get started in the lab, and Ivan Divliansky helped push my thesis along by coming up with a plethora of possible ways we might be able to create new elements. Daniel Ott was also very helpful, working with me to run experiments and characterization procedures. I would like to thank all of the members of the PPL group for their input and advice, and I would also like to thank my family for their support and encouragement.

## TABLE OF CONTENTS

LIST OF FIGURES .....	vii
LIST OF TABLES .....	xi
CHAPTER 1: INTRODUCTION .....	1
1.1 Conventional Phase Masks .....	2
1.2 Photo-Thermo-Refractive Glass .....	4
1.3 General Recording Procedure .....	7
1.4 Summary .....	8
CHAPTER 2: PROPERTIES OF VOLUME PHASE MASKS .....	9
2.1 Periodic Phase Masks .....	10
2.2 Non-Periodic Phase Masks .....	14
2.2.1 Effects on Beam Profile .....	16
2.2.2 Effects on Mode Conversion.....	24
2.3 Summary .....	32
CHAPTER 3: PROBABILISTIC PHASE MASKS .....	33
3.1 Recording with Amplitude Masks .....	34
3.1.1 Ideal Amplitude Masks .....	38
3.1.2 Probabilistic Amplitude Mask .....	40
3.1.3 Profile Optimization.....	44

3.2 Spiral Phase Mask.....	46
3.3 Fresnel Lens .....	52
3.4 Summary .....	59
CHAPTER 4: ABERRATIONS AND CORRECTING METHODS.....	61
4.1 Bragg Gratings Recorded in a Two-Beam Interference System.....	62
4.2 Description of Aberrations.....	66
4.3 The Effect of Aberrations on Thick Reflecting Gratings .....	71
4.4 Aberration Correcting Elements .....	82
4.5 Summary .....	87
CHAPTER 5: HOLOGRAPHIC PHASE MASKS .....	88
5.1 Recording Complex Phase Structures in Photosensitive Media .....	88
5.2 Coupled Wave Equations for Phase Shifted Transmitting Bragg Gratings.....	91
5.3 Diffraction with Binary Phase Encoding .....	96
5.4 Multiplexed Mode-Converting Masks.....	106
5.5 Summary .....	108
CHAPTER 6: SUMMARY AND CONCLUSIONS .....	110
APPENDIX: MATLAB CODE FOR COMPUTER SIMULATIONS .....	113
REFERENCES .....	134



## LIST OF FIGURES

Figure 1.1: Refractive index change vs. exposure dosage at 325 nm for values of $\epsilon$ corresponding to common glass melts and baking temperatures. Here $n_s$ is assumed to be 1000 ppm. ...	7
Figure 2.1: Two flat-top beams interfering with a half angle of interference $\theta$ to produce a sinusoidal grating in the bulk of a photosensitive medium.....	12
Figure 2.2: Illustration of collimated beam passing through a phase mask and being focused by a lens to achieve the far field beam profile. This illustration represents the coordinate system used throughout Chapters 2 and 3 for observing the intensity profile of a beam after passing through a phase mask. ....	16
Figure 2.3: Simulated beam profile of a Gaussian beam acquiring a binary step index phase profile in (a) the near field immediately after the sample and (b) in the far field. ....	17
Figure 2.4: Average absolute difference immediately after the sample between a binary VPM and an ideal binary phase mask for beams of diameters between 0.5 and 3 mm. ....	18
Figure 2.5: (a) Fresnel pattern immediately after the sample for large phase changes and (b) how they form and progress as the total phase accumulation increases. ....	19
Figure 2.6: Simulated far field intensity profile of beams after passing through a thin film mask with a $4\pi$ phase shift and VPMs containing a $4\pi$ and $8\pi$ phase shift. In all cases the far field profile is a Gaussian distribution. ....	20
Figure 2.7: Near-field scan of a beam passing through a sample containing a $\pi$ phase discontinuity using a fiber. The beam profile in the presence of the phase discontinuity shows a fluctuation in the intensity which is not expected if the mask acts as a traditional thin film mask. ....	22
Figure 2.8: Absorption in PTR glass after exposure and thermal development. Bleaching the sample after development is critical for achieving low-absorption samples. ....	22
Figure 2.9: Far field intensity distribution of a beam with a $\pi$ phase shift located at the beam center. This profile is measured at the focal plane of a 500 mm lens along the $f_x$ axis shown in Fig. 2.2. Here the $x$ scale on the horizontal axis refers to the lateral distance from the optical axis.....	24
Figure 2.10: Binary phase distribution for (a) a four-sector and (b) eight-sector mode converting phase mask. ....	25
Figure 2.11: Simulated far field intensity profile of a beam passing through (a) a four-sector and (b) an eight-sector mode converting phase mask.....	28
Figure 2.12: Simulated coupling efficiency of a beam after passing through a four-sector and eight-sector mask into the $TEM_{11}$ mode and $LG_{04}$ mode for different mode radii. The correct mode radius for determining the overlap of the field distribution with the $TEM_{11}$ and $LG_{04}$ mode is 0.577 and 0.445 times the radius of the initial Gaussian beam, respectively. ....	29
Figure 2.13: Experimental far field intensity distribution of a beam passing through a four-sector (a) and eight-sector (b) mode-converting VPM.....	30
Figure 2.14: Overlap integral of a Gaussian beam after passing through a VPM with higher order modes of different radii. Solid lines represent the ideal overlap integral and dotted lines represent the integral with the experimental data shown in Fig. 2.13. ....	31
Figure 3.1: Recording system for producing grayscale phase masks from an amplitude mask. ..	34

Figure 3.2: Simulated phase profile recorded into a 1.5 mm PTR sample for (a) a parabolic and (b) a sawtooth amplitude mask profile using the contact copy method.....	40
Figure 3.3: A probabilistic mask creates a quasi-grayscale intensity distribution via diffraction from micro-apertures. The transparency of a given aperture is based on the probability that the local desired phase at a given point is greater than a random number.....	42
Figure 3.4: Simulated phase distributions produced by probabilistic masks which replicate the amplitude transmittance function and the intensity transmittance function of a grayscale amplitude mask. ....	43
Figure 3.5: Phase profiles recorded by probabilistic masks with pixel sizes of {(a), (e)} 1 $\mu\text{m}$ , {(b), (f)} 2 $\mu\text{m}$ , {(c), (g)} 5 $\mu\text{m}$ , and {(d), (h)} 10 $\mu\text{m}$ .....	45
Figure 3.6: (a) Ideal phase distribution for an $m = 1$ spiral phase mask and (b) the resulting far field distribution of a collimated 3 mm beam after acquiring the phase distribution and being focused by a 100 mm lens.....	47
Figure 3.7: (a) Simulated spiral phase mask formed in PTR glass by the contact method and (b) the vortex profile 6 m after the phase mask. Due to computational limitations the profile in the far field could not be obtained with high resolution, but experimental evidence indicates that the profile does not significantly alter if focused by a lens. ....	49
Figure 3.8: (a) Simulated phase profile induced by a probabilistic amplitude mask in the contact copy configuration and (b) the resulting beam profile 6 m after the mask.....	50
Figure 3.9: (a) Annular far field beam profile of a 1 mm beam passing through a probabilistic spiral phase mask, and (b) the fork dislocation produced by the mask in an interferometer. Because the interferometer is a double-pass interferometer the topological charge is doubled, producing three times in the fork. ....	51
Figure 3.10: Diagram of a plano-convex lens in the configuration used to calculate the phase profile of a Fresnel lens.....	53
Figure 3.11: (a) Simulated phase profile of an ideal, $f = 100$ mm Fresnel lens and a lens recorded with a grayscale amplitude mask and (b) the energy distribution in the focal plane of the lens. ....	54
Figure 3.12: (a) Simulated phase profile of an ideal, $f = 100$ mm Fresnel lens and the profile produced by a probabilistic amplitude mask and (b) the resulting energy distribution in the focal plane of the lens. ....	56
Figure 3.13: (a) Energy distribution in the focal plane of a 200 mm focal length probabilistic Fresnel lens, showing a nearly Gaussian central spot. (b) When the intensity is increased the low energy diffraction rings become visible.....	58
Figure 4.1: Interference profile created by (a) the diffracted orders of a phase mask and (b) the interference of two beams in a holographic system.....	62
Figure 4.2: Schematic of a one-dimensional volume Bragg grating. Note that all angles shown are angles in the medium. ....	64
Figure 4.3: (a) Angular spectra of transmitting volume Bragg gratings of various strengths and (b) wavelength spectra of reflecting Bragg gratings.....	66
Figure 4.4: Aberrated fringe pattern recorded in (a) a thin sample (b) a thick sample. As the beams propagate in thick media different parts of the beams interfere, resulting in different fringe patterns at different depths. ....	71
Figure 4.5: Geometry of an RBG. Two recording beams with a half angle of interference $\theta$ inside the medium create a fringe pattern in the medium which acts a reflecting grating	

	for a probe beam incident along the orthogonal plane. In the presence of aberrations $\theta$ is not a constant but has local variations based on the wavefronts of the beams. When propagating the writing beams a rotated coordinate system is used to simplify the propagation equations. ....	72
Figure 4.6:	Reflection spectra in the presence of one wave of a given aberration for Grating A {(a), (b)}, and Grating B {(c), (d)}. The reflection spectra for a beam incident on the center of the grating {(a), (c)} is different than when the beam is incident at a point halfway between the center and the edge of the grating {(b), (d)}.....	80
Figure 4.7:	Reflection spectrum for a 3 mm beam centered on Grating B in the presence of one wave of coma $x$ if the local tilt of the grating is ignored and only the local change in period is considered. ....	81
Figure 4.8:	The spherical aberration in a system is corrected using a PTR aberration-correcting element without altering the other aberrations in the system. ....	84
Figure 4.9:	Aberration correction for varying amounts of spherical, coma $x$ , and coma $y$ along with linear fits. Astigmatism is not altered by the ACE. Here the aberration correction is given as the Zernike coefficient in waves rather than the Seidel values because the Seidel aberrations, which lack uniqueness, cannot distinguish the components of a given aberration along each axis.....	86
Figure 5.1:	A phase element in one arm of the two-beam interference system creates an object beam which, when interfered with the reference beam, produces a complex hologram. .	89
Figure 5.2:	Diffraction in the presence of a discontinuity in the grating phase. Different parts of the transmitted and diffracted beams may see the phase discontinuity as the beams propagate throughout the grating. ....	93
Figure 5.3:	Orientation of the holographic phase masks used throughout this chapter. The incident, transmitted, and diffracted beams all lie within the $x$ - $z$ plane.....	96
Figure 5.4:	(a) Phase distribution of the diffracted beam in the presence of a binary shift in the grating phase along the $x$ -axis and (b) the intensity distributions of the transmitted and diffracted beams.....	97
Figure 5.5:	(a) Phase distribution of the diffracted beam in the presence of a binary shift in the grating phase along the $y$ -axis and (b) the intensity distributions of the transmitted and diffracted beams.....	98
Figure 5.6:	Mach-Zenhder configuration for recording large-period gratings with binary phase encoding.....	100
Figure 5.7:	Image of overlapped recording beams on luminescent paper with a four-sector mode converting mask in one arm of the system. Note the cross pattern in the middle of the beams; this is due to diffraction from the transition regions of the phase mask in the object beam. Because the intensities of the recording beams are reduced along the cross only a very weak grating can form. ....	101
Figure 5.8:	Diffracted beam after passing through a holographic phase mask encoded with a four-sector mode converter. This image was taken when the diffracted beam had propagated 7 cm after the mask, and the horizontal line is clearly narrower than the vertical line. Though it was not possible to take an image of the beam closer to the mask, a visual inspection of the beam on a screen brought to within 0.5 cm of the mask showed that the horizontal line is invisible at this distance while the vertical line was the same size as that shown in the above image. ....	103

Figure 5.9: Far field profile of the diffracted beam from a four-sector holographic phase mask at (a) 632.8 nm, (b) 975 nm, and (c) 1064 nm. The sizes shown here are not to scale. ....	104
Figure 5.10: Overlap integral of the diffracted beam with the $TEM_{11}$ mode at 975 nm and 1064 nm. There is not a perfect overlap with the ideal binary phase mask, indicating that the holographic phase profile is not a perfect binary profile. However, the conversion efficiency profiles at 975 nm and 1064 nm are nearly identical, indicating that the phase profile recorded can be extracted at any wavelength which can satisfy the Bragg condition. ....	104
Figure 5.11: (a) Far field profile of a beam converted from a higher order mode to a Gaussian profile. (b) Horizontal and (c) vertical cross-sections of the beam indicate that the main spot has a near-diffraction-limited Gaussian profile.....	106
Figure 5.12: Far field profile of the beam diffracted from a multiplexed holographic phase mask when satisfying the Bragg condition for (a) a homogenous grating, (b) a two-sector mode converter, and (c) a four-sector mode converter. ....	108

## LIST OF TABLES

Table 2.1: The Hermite and Laguerre polynomials [61,62]. .....	26
Table 3.1: Focusing efficiency vs. focal length for simulated Fresnel lenses produced by the contact copy method using grayscale amplitude masks. ....	55
Table 3.2: Focusing efficiency of probabilistic Fresnel lenses for various focal lengths. ....	59
Table 4.1: List of aberrations described by the power series terms of the wavefront and the relationship between the power series coefficients and Seidel coefficients [88]. ....	67
Table 4.2: List of Zernike polynomials using Noll notation. It should be noted that these polynomials give the peak-to-valley wavefront aberration (maximum deviation to minimum deviation); for RMS aberrations each polynomial will be multiplied by a unique constant [89]. ....	69
Table 4.3: Conversion from Zernike description of aberrations to Seidel description [88]. Here $C_j$ is the coefficient in waves of the $j$ th Zernike polynomial in Noll notation. ....	70

## CHAPTER 1: INTRODUCTION

In this thesis a method for recording phase masks in the bulk of a photosensitive glass is demonstrated. The term “phase mask” is used to define any optical element excluding traditional lenses in which a spatially dependent phase profile is induced. Phase masks have been used for decades for a variety of applications, including improving the depth of field [1-3], manufacture of electronics [4], encryption [5-8], and coronagraphy [9-11]. While a phase mask may have an arbitrary phase profile in order to meet the needs of the system, there are several general categories of phase masks, including gratings [12-18], beam shapers [19-23], and mode converters [24,25]. Also, while traditional lenses are not considered phase masks, focusing elements such as Fresnel lenses may be considered phase masks as their total phase variation does not exceed  $2\pi$  and they typically contain multiple zones with a rapid phase variation at the boundary regions.

In this chapter the properties and limitations of conventional phase mask substrates are discussed and photo-thermo-refractive (PTR) glass, the substrate used in this thesis to surmount the conventional limitations, is described. Chapter 2 focuses on the properties that an ideal volume phase mask (VPM) recorded into the bulk of PTR glass has, describing the similarities and differences of VPMs to traditional phase masks. Chapter 3 discusses the means by which VPMs containing arbitrary profiles can be recorded into a sample and the limitations of current recording techniques. Chapter 4 discusses aberrations in a holographic system and demonstrates VPMs which can correct them, and Chapter 5 discusses holographic phase masks, where multiple phase masks can be encoded into a single element.

## 1.1 Conventional Phase Masks

Conventional phase masks are generally produced by either sculpting the surface of a material or by recording it in the bulk via direct exposure (including holographic exposure). While several substrates are used in the literature, for the sake of brevity only three common substrates will be discussed here: photoresists, dichromated gelatin, and photorefractive crystals. All of these substrates are used to produce a permanent (or in the case of the photorefractive crystals, semi-permanent) phase profile. While elements such as spatial light modulators can be used to create arbitrary phase distributions these elements are not generally considered phase masks and so are not included here.

Photoresists are photosensitive polymer structures such as poly(methyl methacrylate) (PMMA). When exposed to UV radiation, the solubility of photoresist to a chemical developer will change, either becoming soluble in the exposed regions (positive resist) or becoming insoluble in the exposed regions (negative resist). As the local phase is equal to  $\varphi = 2\pi nt / \lambda$ , to produce the desired local phase change either the initial thickness is controlled or the exposing dosage is modified so that only a portion of the resist changes solubility in the exposed region [26]. Despite its photosensitivity however, photoresist does not undergo refractive index change, which inherently limits its use to surface profiles where local phase accumulation is based on the optical path length of the resist. In addition, the absorption coefficient of PMMA in the visible and near-IR region is between 0.06 and 0.08  $\text{cm}^{-1}$  (defined here as the base 10 absorption coefficient:  $I = I_0 10^{-\alpha d}$ ) [27]. With this level of absorption, even a 1  $\mu\text{m}$  thick sample can be heated to above the melting point of PMMA in a multi-kilowatt system, depending on the beam power and diameter [28-32]. While air cooling may be applied to the sample, the high air

pressure necessary to reduce the temperature below the point where the surface profile is not degraded by heat is likely to ablate the surface to the point where the profile is destroyed. Thus PMMA and similar photoresists cannot be used in high power systems.

Another thin-film-type substrate is dichromated gelatin (DCG) (natural gelatin doped with  $(\text{NH}_4)_2\text{Cr}_2\text{O}_7$  or  $\text{K}_2\text{Cr}_2\text{O}_7$ ), which, like photoresist, becomes insoluble in water after exposure to UV or blue light. However, unlike photoresist DCG undergoes refractive index modulation as well. It is a popular material for the production of holographic optical elements because of its capacity for high refractive index modulation (up to 80,000 ppm), a resolution capacity greater than 5000 lines/mm and its ability to be redeveloped to produce the desired amount of refractive index modulation [33]. In addition the thickness of the DCG layer can be controlled and with the addition of appropriate dyes DCG can be made photosensitive at red wavelengths. However, this potentially wide region of photosensitivity results in a higher absorption coefficient at many wavelengths, and as the melting point of gelatin is  $\sim 30^\circ\text{C}$  depending on the grade [34], it cannot be used in kilowatt-level systems.

If it is desirable to have a phase profile recorded in the bulk of a material, without any changes to the surface profile, a commonly used substrate in a photorefractive crystal. Photorefractive crystals utilize the electro-optic effect to create a refractive index change. While several photorefractive crystals are described in the literature, only lithium niobate ( $\text{LiNbO}_3$ ), which is the most commonly used crystal, will be covered here. During the irradiation of  $\text{LiNbO}_3\text{:Fe}$  crystals (as with other dopants in  $\text{LiNbO}_3$ ), electrons are excited into the conduction band from  $\text{Fe}^{2+}$  ions trapped within the valence band. At low intensities the number of electrons excited is directly proportional to the light intensity and concentration of  $\text{Fe}^{2+}$  ions [35]. From the conduction band electrons rapidly recombine with defects present in the crystal at an



intermediate level between the valence and conduction bands. For typical  $\text{LiNbO}_3$  crystals the number of defects is significantly greater than the number of deep  $\text{Fe}^{3+}$  recombination centers. As a result, electrons will diffuse between defect sites until recombining with deep centers [36].

$\text{LiNbO}_3$  masks have lesser utility than DCG masks in that refractive index modulation can only occur when there is a net diffusion of electrons into  $\text{Fe}^{3+}$  traps. Therefore it is impossible to modify the refractive index over an area significantly larger than the diffusion length, as many of the electrons will merely refill the newly ionized  $\text{Fe}^{2+}$  centers. Also, unlike DCG masks, the space charge distribution is not permanent, as any incident light that can re-excite electrons can erase or modify the initial distribution [37]. This prevents lithium niobate from being used in high power systems since the refractive index profile will be rapidly erased.

## 1.2 Photo-Thermo-Refractive Glass

As seen with photoresist and DCG absorption in the substrate may result in the phase profile being destroyed and so for phase masks to be used in high power systems it is necessary to have low absorption in the substrate to avoid overheating. Also, since surface masks may have problems with dust and handling errors, recording into the bulk of a medium is desirable. When recording in the bulk of a material the ideal substrate will have a high laser damage threshold, a high melting point, and will allow a phase profile of arbitrary shape and size to be recorded within it. The substrate used in this thesis, which has the necessary properties, is photo-thermo-refractive (PTR) glass.

PTR glass is a sodium-potassium-zinc-aluminum-fluorine-bromine-silicate glass doped with cerium, antimony, tin, and silver [38], with a region of transparency from 350 nm to 2700 nm [39] and a damage threshold of  $40 \text{ J/cm}^2$ . Due to this wide transparency window, PTR glass

is used to produce volume Bragg gratings for the visible and infrared regions, which have found applications in pulse stretching and compression and beam steering, and their high laser damage threshold is ideal for high power spectral beam combining [17]. In the near IR region PTR glass has an absorption coefficient of  $\sim 10^{-4} \text{ cm}^{-1}$ , and air cooling can be applied to the sample without degrading the recorded profile or seriously affecting the beam [40].

Refractive index modulation is achieved via a multi-step process: it is first exposed to UV radiation from a He-Cd laser, ionizing  $\text{Ce}^{3+}$  to  $\text{Ce}^{4+}$ . The ionized electrons are trapped in intrinsic defects of the glass matrix or are bound to dopants and impurities, including  $\text{Ag}^+$  ions, which are reduced to atomic silver. Thermal development of the glass at a temperature of approximately  $485^\circ\text{C}$  causes the atomic silver to conglomerate into clusters which serve as nucleation centers for sodium fluoride (NaF) nanocrystals. After the nucleation centers are formed the glass is cooled to below  $200^\circ\text{C}$  and then heated to temperatures between  $500^\circ\text{C}$  and  $520^\circ\text{C}$ , during which the NaF nanocrystals will form. After development the nanocrystals are typically about 20 nm in diameter with an average spacing of approximately 110 nm [38].

After NaF crystallization is complete the exposed portion of the glass can be broken into three nanoscopic regions: the NaF crystals, the surrounding region which has been depleted of sodium and fluorine, and the chemically unaltered PTR glass. The size of the three regions is dependent on the total refractive index change, with the depleted region being anywhere from a few tens of nanometers to the full distance between the NaF crystals. In considering stresses between the three regions, note that immediately after development but before cooling the glass is above the glass transition temperature  $T_g \sim 460^\circ\text{C}$  so the glass acts as a viscous liquid. Therefore any stresses between the three regions will relax quickly. However, the coefficient of thermal expansion (CTE) for NaF is  $\sim 3.6 \times 10^5 \text{ K}^{-1}$  while the CTE for virgin PTR glass is  $\sim$

$1 \times 10^5 \text{ K}^{-1}$ , nearly a factor of four smaller. Therefore, as the glass is cooled radial and tangential stresses, which are constant over the volume of the NaF crystals and decay as  $r^{-3}$  for the depleted and unaltered PTR glass, will build between the regions. Due to the large difference in the CTE for the NaF and the virgin glass, the largest contribution to the stress is at the NaF/depleted glass interface, with stresses of 750-950 MPa being measured by XRD spectroscopy, which is close to the point at which microstresses will fracture the glass [38]. These stresses induce an absolute refractive index modulation of up to 1000 ppm. These stresses are only present when the glass is cooled to room temperature and will relax if the glass is reheated above  $T_g$ ; as described in [38] if a PTR sample is heated to 500°C after development then no refractive index change is measured. However, after the sample has cooled then the stresses reappear and refractive index modulation is present once more. It should be noted that these stresses slightly decrease the density of the material so the induced refractive index change is negative.

The total refractive index change that will be induced in the glass is a function of the dosage irradiating the sample, the temperature at which it is developed, the time for which it is developed, and how it is cooled [38,41,42]. For a given fixed temperature if the glass is allowed to cool slowly ( $\sim 0.1 \text{ K/min}$ ) after the final thermal treatment (where the NaF crystals are developed) then the refractive index change can be modeled empirically [41] using a hyperbolic formula:

$$\Delta n = \frac{n_s D}{\varepsilon + D} . \quad ( 1.1 )$$

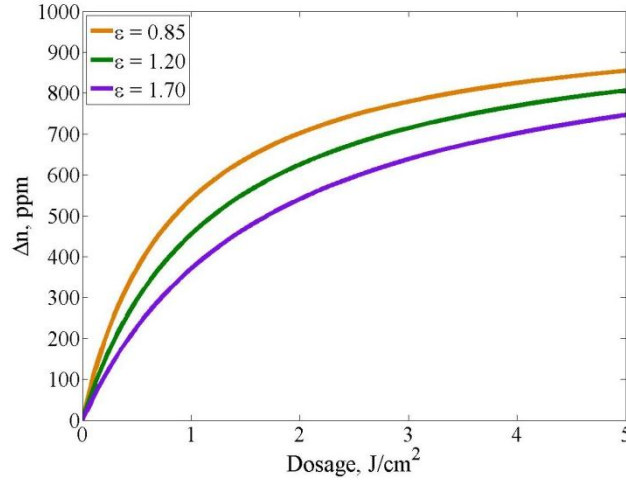


Figure 1.1: Refractive index change vs. exposure dosage at 325 nm for values of  $\epsilon$  corresponding to common glass melts and baking temperatures. Here  $n_s$  is assumed to be 1000 ppm.

Here  $\Delta n$  is the refractive index change,  $n_s$  is the maximum refractive index change induced by saturating the sample with infinite dosage,  $D$  is the dosage, and  $\epsilon$  is the rate of change corresponding to a dosage necessary to achieve  $n_s/2$ , which depends on the glass properties and the temperature of development when forming the nanocrystals. Fig. 1.1 shows the refractive index change curves for some common glass melts when exposed to a beam at 325 nm, the emission wavelength of a He-Cd laser. Nonlinear effects become significant for peak dosages larger than approximately  $0.75 \text{ J/cm}^2$  and must therefore be taken into account when recording elements with a large dosage. Note that using a smaller dosage and a longer bake time at a given temperature can improve the linearity of the refractive index profile but not eliminate it entirely.

### 1.3 General Recording Procedure

Having chosen the recording medium for this work it is necessary to determine the methods by which one may record volume phase masks (VPMs) in PTR glass. In general there are three techniques which may be employed: direct writing, indirect illumination through an amplitude mask and imaging system, and direct illumination through an amplitude mask using

the contact copy technique. While each technique has its strengths and weaknesses, the method of choice in this thesis is direct illumination of the sample using the contact copy method. In this system an amplitude mask is placed directly on top of the sample, with some index matching fluid between them to eliminate any reflections. The mask and sample are then illuminated by the recording beam, which may either completely illuminate the mask or illuminate it piecemeal via a raster scan. This method can have difficulties when illuminated by a monochromatic, coherent source, as it is still possible to have an interference pattern between the transmitted and diffracted portions of the beam after passing through the amplitude mask (unless the aperture dimensions in the amplitude mask are subwavelength). However, if the source is broadband any interference profile will be partially or completely washed out, depending on the bandwidth and degree of coherence of the source. The main limitation of this technique is diffraction from sharp edges in the amplitude mask. This generally prevents very sharp phase transitions, which, as will be seen in later chapters, can reduce performance in certain applications.

#### 1.4 Summary

Conventional substrates for recording phase masks cannot be used in high power systems. Furthermore, thin-film-type substrates, which are used to create surface phase masks, can be easily damaged via handling and can have their phase profiles significantly affected by dust. To avoid these problems, phase masks in this thesis are recorded in the bulk of PTR glass, which due to its low absorption and high damage threshold makes it a suitable substrate for high power applications. To record the phase profiles into the glass, the contact copy method with an amplitude mask and broadband illumination is used where the desired phase profile is converted into an amplitude profile for recording.

## CHAPTER 2: PROPERTIES OF VOLUME PHASE MASKS

*Note: This chapter contains material which was or will be published in the following works:*

*M. SeGall, V. Rotar, J. Lumeau, S. Mokhov, B. Zeldovich, and L. B. Glebov, "Binary volume phase masks in photo-thermo-refractive glass," Optics Letters 37, 1190-1192 (2012).*

*M. SeGall, I. Divliansky, D. Ott, J. Lumeau, S. Mokhov, B. Zeldovich, and L. B. Glebov, "Beam shaping by volume phase structures in photo-thermo-refractive glass," Optics+Photonics 8843-6 (2013) (conference proceedings to be published)*

*M. SeGall, I. Divliansky, and L. B. Glebov, "Gradual phase accumulation in thick media," (to be published)*

As described in the previous chapter, phase masks constitute a class of elements which have a variety of different applications, depending on their composition and phase profile. While in general phase masks may be transmissive or reflective, in this thesis only phase masks which are transmissive will be considered, as this is generally the case for all masks except for gratings which are placed in a closed system. In industrial applications such masks are typically intended to be permanent, and are therefore recorded in photoresist or DCG, which is no more than a few tens of microns thick. Volume phase masks however will generally be recorded in a sample which can be several millimeters thick. As this is two orders of magnitude thicker than traditional masks it is possible for a thick mask containing the same phase profile as a thin mask to demonstrate different effects both in the near field and in the far field. In this chapter the properties of volume phase masks will be discussed and the applications in which they may be used will be described.

## 2.1 Periodic Phase Masks

Periodic phase masks (i.e., gratings) are a well-known example where phase accumulation in the bulk of a large medium may have different effects than the same phase accumulation over a few microns at the surface. This problem has been well-studied in the literature, and there are two broad regions for which several analytical theories have been developed [43-47]. The first region is the Raman-Nath diffraction regime, which is typically associated with “thin” gratings. Raman-Nath diffraction is characterized by an incident beam being diffracted into multiple diffraction orders, with each of the orders diffracting symmetrically about the 0<sup>th</sup> order (where the 0<sup>th</sup> order is the order where the beam is transmitted at the same angle as the incident angle, and therefore is not diffracted). This regime is effectively polarization insensitive and can be described using scalar diffraction theory, where the vectorial nature of the electric field is ignored. To be in the Raman-Nath regime the incident beam must generally satisfy the paraxial approximation, as at large angles polarization effects become prevalent, precluding the use of scalar diffraction theory, and the symmetry of the system is broken by some diffraction orders becoming evanescent [47].

Gratings which exhibit Raman-Nath behavior, which will henceforth be referred to as thin gratings, are typically produced by creating a surface profile in a dielectric material with refractive index  $n$  and immersing it in a medium with refractive index  $n_0$ . The diffracted orders are diffracted from the grating in a ray fan with each order propagating at an angle given by the grating equation [43]:

$$\Lambda n_0 (\sin \theta_i + \sin \theta_m) = m\lambda. \quad (2.1)$$

Here  $\Lambda$  is the grating period,  $\theta_i$  and  $\theta_m$  are the angles of the incident and  $m$ th diffracted order, and  $\lambda$  is the free-space wavelength. As can be seen from Eq. 2.1 the diffracted ray fan is symmetric, and for a constant period and incident angle, the only effect of changing the wavelength is to alter the angles of the diffracted rays.

The diffraction efficiency of a thin grating depends upon its phase profile; for a sinusoidal grating each of the orders will have a diffraction efficiency (in the Raman-Nath regime) of

$$\eta_m = J_m^2\left(\frac{\varphi_p}{2}\right), \quad (2.2)$$

where  $J_m$  is the  $m$ th order Bessel function of the first kind and  $\varphi_p$  is the peak-to-peak (maximum of the sinusoidal pattern to the minimum of the sinusoidal pattern) phase variation of the grating [43]. Note that as the efficiencies are determined by the Bessel functions it is impossible to achieve higher efficiencies than the global maximum of the Bessel functions. For diffraction into the first order this limits the maximum efficiency to 33.8%. This limit, however, is based on the assumption that the grating is used at small incident angles. It is possible to achieve higher efficiencies if the incident angles are very large (close to  $90^\circ$ ), with up to 100% efficiency theoretical possible due to all other orders becoming evanescent [47]. However, as stated previously in this configuration the grating is not exhibiting true Raman-Nath diffraction due to polarization effects becoming prevalent, preventing the use of scalar diffraction theory to model the system. While Harvey et al. have developed a nonparaxial scalar diffraction theory for TE polarization which can model the grating system [47], they have not been able to do so for TM polarization and so in general the grating must be modeled using some form of vectorial theory to calculate the fields.



Volume gratings by contrast are typically created by holographic exposure of an interference pattern into the bulk of a photosensitive medium. A transmitting grating is formed when two flat-top beams which are both incident on the same face of the sample interfere in the medium, creating a sinusoidal fringe pattern with a period controlled by the angle of interference between the beams, as shown in Fig. 2.1. Due to the large interaction length between an incident beam and the recorded fringe pattern the dephasing between diffraction orders becomes larger, reducing the amount of power transferred between the orders. If the dephasing is large enough only a single diffraction order aside from the 0<sup>th</sup> order will be present. This is the second overall regime in which a grating may operate, referred to as Bragg diffraction. Diffraction into an order other than the 0<sup>th</sup> order only occurs when a probe beam is incident at or near a specific angle known as the Bragg angle, which may or may not be an angle small enough to apply the small angle approximation, requiring a vectorial diffraction theory to model the system [44-46]. The Bragg angle is given by [44]:

$$2n_0\Lambda \sin \theta_B = m\lambda . \quad ( 2.3 )$$

At the Bragg angle the diffracted beam diffracts at angle which is equal in magnitude and opposite in sign from the incident angle (in the grating medium; Snell's law must be applied at the boundaries).

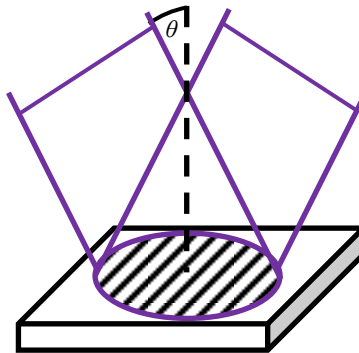


Figure 2.1: Two flat-top beams interfering with a half angle of interference  $\theta$  to produce a sinusoidal grating in the bulk of a photosensitive medium.

Here it is assumed that the grating has fringes which are not tilted, which occurs when the angle between the first writing beam (the left beam in Fig. 2.1) and the normal to the grating surface is identical to the angle between the second writing beam (the right beam in Fig. 2.1) and the normal to the grating surface, though a more complete description is given in Chapter 4.

In addition to the different number of diffracted orders present as compared to thin gratings, volume gratings have a significantly different criterion for diffraction efficiency. The peak diffraction efficiency of a grating is achieved when the Bragg condition is fulfilled (i.e. when the incident beam is at the Bragg angle), and for a grating without tilted fringes this diffraction efficiency is given by [44]:

$$\eta = \sin^2 \left( \frac{\pi \Delta n d}{\lambda \cos \theta_B} \right). \quad (2.4)$$

Here  $\Delta n$  is the refractive index modulation and  $d$  is the grating thickness. Note that by proper choice of  $\Delta n$  and  $d$  it is possible to achieve 100% diffraction efficiency, when the argument of the sine function is  $\pi/2$ . Also, as the efficiency is a sinusoidal function of  $\Delta n$  and  $d$  there are multiple thicknesses which will have the same diffraction efficiency for a given  $\Delta n$ . However, increasing the thickness such that the argument is larger than  $\pi/2$  results in a decrease of angular selectivity [44], which is generally undesirable in practice.

The boundary between the Bragg regime and the Raman-Nath regime is a question of interest because it does not depend solely on the physical thickness of a grating. As described in Refs. [45,48-52], two parameters are necessary to quantify the position of the boundaries. The parameters are  $Q'$  and  $\gamma$ , defined as

$$Q' = \frac{2\pi\lambda d}{n_0 \Lambda^2 \cos \theta_B} \quad (2.5)$$

$$\gamma = \frac{\pi \Delta n d \rho}{\lambda \cos \theta_B}. \quad (2.6)$$

Here  $\rho$  is a polarization term, which is equal to 1 for TE polarization and  $\cos 2\theta_B$  for TM polarization.

If  $Q'\gamma \gg 1$  (usually a value larger than 20 is sufficient) then the grating will be in the Bragg regime. Note that this ratio has no dependence on the thickness of the grating, but depends only on the modulation of refractive index, the grating period, and the wavelength of the incident beam. If  $Q'\gamma \ll 1$  the grating will be in the Raman-Nath regime, and Moharam and Young have shown that a looser criterion of  $Q'\gamma \leq 1$  satisfies the Raman-Nath criterion to within one percent based on the power in the diffracted orders as compared to the power predicted by Eq. 2.2 [48]. Note that this product is essentially a ratio of the thickness to the grating period, so even a grating with small physical thickness may not satisfy the criterion depending on the period. In this case there is poor coupling to any order which does not satisfy the Bragg condition and thus the order will be suppressed. If  $Q'\gamma > 1$  and  $Q'\gamma \simeq 1$  then the grating does not satisfy the conditions for either the Bragg regime or the Raman-Nath regime. In this case the number of diffraction orders, their angles of diffraction, and relative diffraction efficiencies cannot be determined unless a rigorous coupled-wave theory is applied.

## 2.2 Non-Periodic Phase Masks

Non-periodic phase masks, including non-periodic binary masks [9-11,24,53-55], polynomial masks [2], etc., are used for applications such as mode conversion and beam shaping. In this case there is little to no energy diffracted into higher orders and the goal of the phase mask is to provide a specific amount of local phase accumulation in order to shape the wavefront

to a desired profile in a given plane, usually the focal plane of a lens. When manufacturing such a phase mask the traditional assumption is that the mask effectively provides all of the necessary local phase accumulation in a single plane, what is henceforth referred to as the ideal phase mask assumption (IPMA). While this assumption is reasonable in the case where the phase mask is very thin (on the order of a few tens of microns), the gradual accumulation of phase over relatively large distances where the beam has the opportunity to propagate suggests that the IPMA may not apply, as diffraction effects may become significant in a similar manner to volume gratings. To determine the actual beam profile the beam propagation method (BPM) [56] will be used here.

In the BPM the following outline is used for determining the field at a given distance:

1. Take the Fourier transform of the initial electric field.
2. Multiply it by  $\exp[-i(f_x^2 + f_y^2)\Delta z / 2k_0]$ , where  $f_x$  and  $f_y$  are the spatial frequencies,  $\Delta z$  is the propagation distance, and  $k_0$  is the wavenumber. This term provides the linear propagation in the Fourier domain.
3. Take the inverse Fourier transform of the new field.
4. Multiply it by  $\exp[ik_0 n(x, y)\Delta z]$ . This provides the local phase accumulation over the distance  $\Delta z$ . When propagating in a homogenous medium the refractive index is just a constant and so this step may be neglected if the final step is in a homogenous medium (such as propagating in air after passing through an inhomogeneous medium). Note that the refractive index is assumed to be constant in  $z$  over the range of the step size. If the refractive index changes with  $z$  it will be necessary to choose step sizes small enough that it can be assumed to be constant during each step.

5. Set the resulting field as the initial field and repeat steps 1 – 4 until reaching the desired propagation distance.

### 2.2.1 Effects on Beam Profile

As a beam propagates through a VPM it is likely that any significant departure from the IPMA will be due to diffraction effects from sharp boundaries in the local refractive index. To examine this, consider a phase mask which has a step function in its refractive index profile. In particular, consider two samples which are illuminated by a 3 mm (where the beam diameter is defined as the full width at  $1/e^2$  of the intensity profile) collimated Gaussian beam at 632.8 nm, as illustrated in Fig. 2.2. The first sample is 2 mm thick and has a refractive index profile of  $n = 1.5$  for  $x < 0$  and 1.4998418 for  $x \geq 0$ . The second sample is 50  $\mu\text{m}$  thick, and has a refractive index profile of  $n = 1.5$  for  $x < 0$  and 1.493672 for  $x \geq 0$ . This decrease in refractive index provides a phase shift of  $\pi$  after propagating through the thickness of the respective samples. Using the BPM with a step size of 1  $\mu\text{m}$ , a lateral resolution of 100 nm in the spatial domain, and a lateral resolution of  $0.01 \text{ mm}^{-1}$  in the Fourier domain, the phase element is simulated in Matlab and the resulting intensity distribution is then compared to the intensity distribution of a beam which acquires a  $\pi$  phase shift assuming the IPMA.

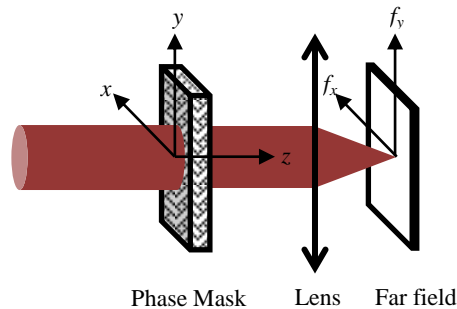


Figure 2.2: Illustration of collimated beam passing through a phase mask and being focused by a lens to achieve the far field beam profile. This illustration represents the coordinate system used throughout Chapters 2 and 3 for observing the intensity profile of a beam after passing through a phase mask.

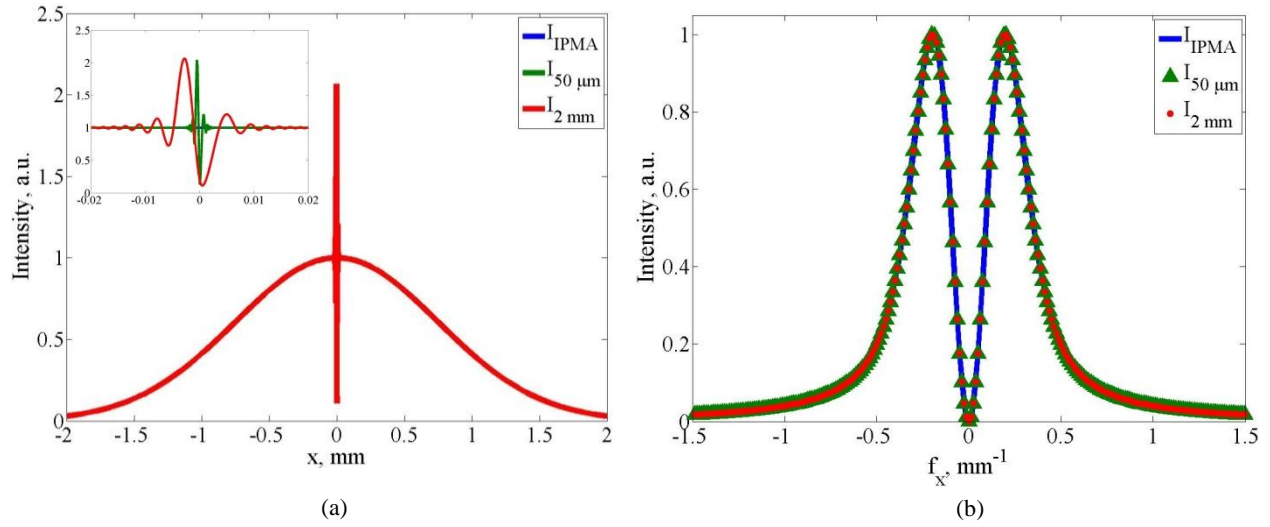


Figure 2.3: Simulated beam profile of a Gaussian beam acquiring a binary step index phase profile in (a) the near field immediately after the sample and (b) in the far field.

As shown in Fig. 2.3a, the beam which acquires its phase change under the IPMA has no change in its intensity profile (as expected) immediately after the sample because the beam has not yet undergone any propagation. The beams which gradually acquire their phase change however have a different profile, with a fluctuation in the profile that is expected due to interference between the diffracted wavefront and transmitted wavefront at the boundary between regions with different refractive indices. These different profiles indicate that because the beam has the opportunity to propagate during its phase accumulation the IPMA cannot be applied, at least in the near field. The sample that is 50  $\mu\text{m}$  thick however shows a profile which is considerably closer to the profile predicted by the IPMA; this is obviously because the sample is closer to fulfilling the assumptions of the IPMA. Though the fluctuation in the intensity profile is still present in the 50  $\mu\text{m}$  sample it occurs over a much narrower region, with the lateral distance between the point of highest intensity and lowest intensity being equal to about one wavelength; this indicates that for traditional thin film masks in which the thickness necessary to achieve a  $\pi$  phase shift is on the order of a few microns there will be no observable deviation

from the input beam profile. If the beams are propagated to the far field, corresponding mathematically to a Fourier transform of the field, then as shown in Fig. 2.3b there is a negligible difference between the intensity profiles under the different assumptions. Thus the IPMA can be applied if the beam is being considered in the far field. Since the difference between a beam undergoing gradual phase change and a beam acting under the IPMA will begin to converge to zero as both beams propagate towards the far field the largest difference between the two cases is therefore in the very near field, immediately after the sample.

To determine the effects of varying sample thickness and beam size on the intensity distribution, the average absolute difference (AAD) between a beam undergoing gradual phase change (GPC) and a beam acting under the IPMA is taken here for beams of diameter in the range of 0.5–3 mm and samples of thickness between 2  $\mu\text{m}$  and 5 mm. Here the average absolute difference is defined as

$$\overline{|I_x - I_y|} = \frac{1}{n} \sum_{i=1}^n |I_{x_i} - I_{y_i}| \quad (2.7)$$

for  $n$  points within an  $e^{-2}$  diameter.

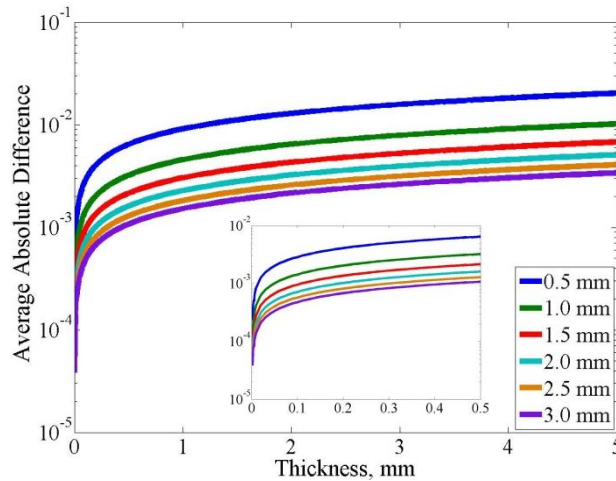


Figure 2.4: Average absolute difference immediately after the sample between a binary VPM and an ideal binary phase mask for beams of diameters between 0.5 and 3 mm.

$I_x$  and  $I_y$  represent the normalized intensity profiles of the different beams. (In this formulation, the peak intensity of the normalized beam subject to the IPMA is unity, and each beam contains an equal amount of energy). In all cases the refractive index difference between regions is chosen so that after propagating the full thickness the beam has acquired a  $\pi$  phase change at 632.8 nm. As shown in Fig. 2.4, in all cases in the near field as the sample thickness increases so does the average absolute difference, and masks which are only a few microns thick are practically indistinguishable from masks subject to the IPMA. However, there is an order of magnitude difference in the value of the AAD for a 100  $\mu\text{m}$  sample compared to a 2  $\mu\text{m}$  sample for all beam diameters; in order to reasonably apply the IPMA in the near field sample thicknesses should be no more than a few tens of microns. Note also that larger beams have more power located far from the phase discontinuity so their average absolute difference is consequently smaller. In the far field the AAD is zero to within the rounding errors of the software for all diameters and sample thicknesses.

A further difference between beams undergoing GPC and beams acting under the IPMA can be seen if the relative phase difference is increased to  $2\pi$  or greater.

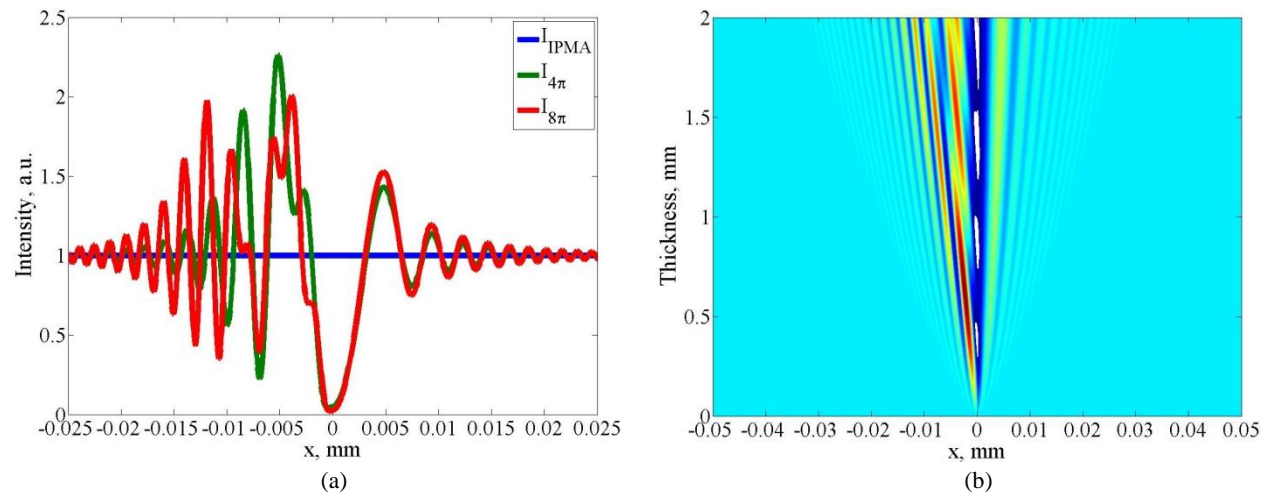


Figure 2.5: (a) Fresnel pattern immediately after the sample for large phase changes and (b) how they form and progress as the total phase accumulation increases.



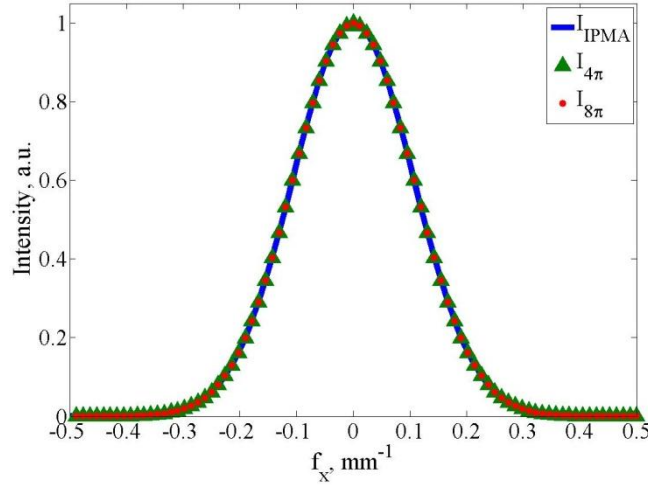


Figure 2.6: Simulated far field intensity profile of beams after passing through a thin film mask with a  $4\pi$  phase shift and VPMs containing a  $4\pi$  and  $8\pi$  phase shift. In all cases the far field profile is a Gaussian distribution.

Returning to the 2 mm sample illuminated by a 3 mm beam, consider now a refractive index profile such that a  $4\pi$  shift is induced. As highlighted in Fig. 2.5a the relatively low intensity side fringes seen in Fig. 2.3a become larger, predominately on the left-hand side where the phase change occurs, though the central null is still present. These side fringes continue to increase in visibility as the total phase change increases, and new fringes will form, as shown in Fig. 2.5b. These fringes shift position linearly as new fringes form with the width and spacing of the fringes differing depending on whether or not they form on the side where the refractive index is changed. However, as seen in Fig. 2.6, in the far field the beam maintains the Gaussian profile that is expected whenever the phase change is a multiple of  $2\pi$ . While difficult to see in Fig. 2.6, there is a slight decrease in intensity of the beams that pass through a VPM as compared to the beam passing through the thin film mask because a small fraction of the energy is diffracted from the boundary between different refractive indices to high spatial frequencies.

To experimentally verify these simulations a VPM containing a  $\pi$  phase shift was recorded by using an amplitude master mask which was opaque over half of the surface. The illumination source was a collimated 1.1 mm He-Cd beam (Kimmon) at 325 nm and the overall

profile was recorded by using a raster scan with each pass partially overlapping the previous pass to create a uniform dosage of  $0.9 \text{ J/cm}^2$ . In order to ensure that reflections from the back surface of the glass would not create an interference pattern within the sample, the back surface and sides were coated in an absorbing solution. This solution was a mixture of First Contact™ polymer solution (Photonic Cleaning Technologies) and standard black ink used in inkjet printers. The ink was added to the polymer solution until the mixture became opaque when dried. The mixture was then painted onto the back surface and sides of the sample, with multiple layers added if there was any light leakage visible by eye. Because the polymer solution has a refractive index close the refractive index of the glass the mixture acted as an absorbing index-matching film. In the same sample, but separate from the mask, a single stripe was recorded with the same dosage as the maximum dosage in the mask.

The sample was then developed following the procedure described in Chapter 1 and a refractive index change of 208 ppm measured in a custom liquid-cell shearing interferometer [57] based on the refractive index change of the stripe. Note that this stripe is necessary, as the shearing interferometer (as well as most interferometers) has difficulty in determining the phase shift at a sharp transition boundary. This is because diffraction from the boundary typically makes it difficult to determine how many fringes the pattern has shifted by in the exposed region, and it is not uncommon for the analysis software to overestimate or underestimate the number of fringes. Therefore the stripe is necessary, as it has a Gaussian intensity distribution with no sharp edges.

To achieve a  $\pi$  phase shift at 632.8 nm the sample was then polished to a thickness of 1.52 mm with a surface flatness of  $\lambda/4$ , measured by a commercial Zygo interferometer. The sample was then bleached [58] to reduce the total absorption in the glass.

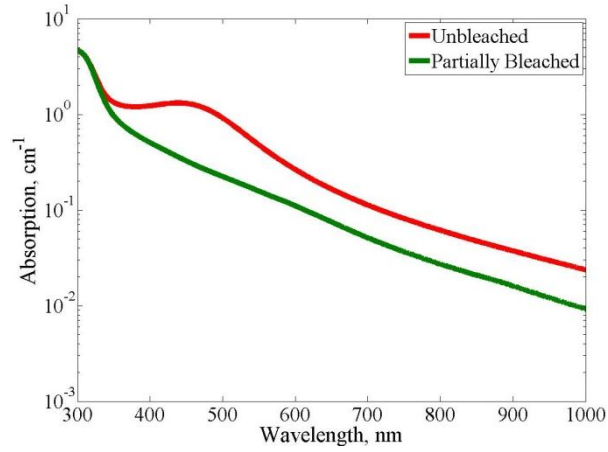


Figure 2.8: Absorption in PTR glass after exposure and thermal development. Bleaching the sample after development is critical for achieving low-absorption samples.

This bleaching removes color centers formed in the glass after exposure and development, shown in Fig. 2.7, and while not generally necessary for phase masks used in low power applications, it is critical for high power applications.

To experimentally determine whether there is any difference between the near field profile of the VPM as compared to a traditional mask a near-field scan was performed by illuminating the sample with a collimated 3 mm He-Ne laser at 632.8 nm and placing a 62.5  $\mu\text{m}$  graded-index fiber (Corning Infinicor 300) directly behind the sample.

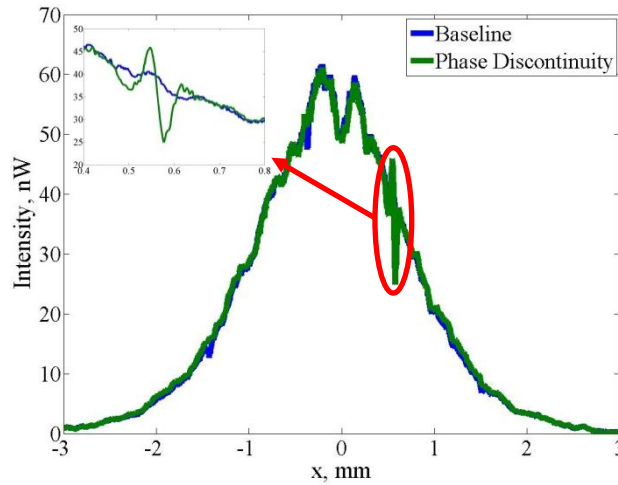


Figure 2.7: Near-field scan of a beam passing through a sample containing a  $\pi$  phase discontinuity using a fiber. The beam profile in the presence of the phase discontinuity shows a fluctuation in the intensity which is not expected if the mask acts as a traditional thin film mask.

The fiber tip was then scanned over the illuminated region at a speed of 5  $\mu\text{m/s}$ . The distance between the fiber tip and the sample was approximately 50  $\mu\text{m}$ , and the output from the fiber directly illuminated a Laserstar detector (Ophir) which sampled at a rate of 3 Hz. As shown in Fig. 2.8, the sample was first illuminated in a region where there was no phase discontinuity in order to determine the beam profile; the VPM acted as a window in this case. A scan was then taken to establish the intensity profile of the incident beam, providing the baseline against which the second scan was compared. Because the beam quality at the center of the beam was poor, when the beam was placed to illuminate the phase discontinuity, the boundary between regions was deliberately offset from the center of the beam, making it easier to establish whether there was any change in the intensity profile. After scanning the beam with the phase discontinuity in place, a clear fluctuation in intensity is observed that is not expected to be seen with the resolution of the fiber if the VPM behaved in the same manner as a thin phase mask. Note that there are some small variations in intensity in the baseline profile which more or less match the positions of the variations seen with the VPM. These fluctuations are consistent with the fluctuations of the illuminating laser intensity and therefore their alignment with the fluctuations seen with the VPM is coincidental.

Though the VPM produces a different intensity profile in the near field, in the far field the intensity distribution shows the same two-lobed structure expected when a traditional phase mask is used, as seen by the cross-section shown in Fig. 2.9 where the beam is focused by a 500 mm lens. Note that in this figure the position of the beam has been shifted so that the phase discontinuity is no longer offset from the beam center.

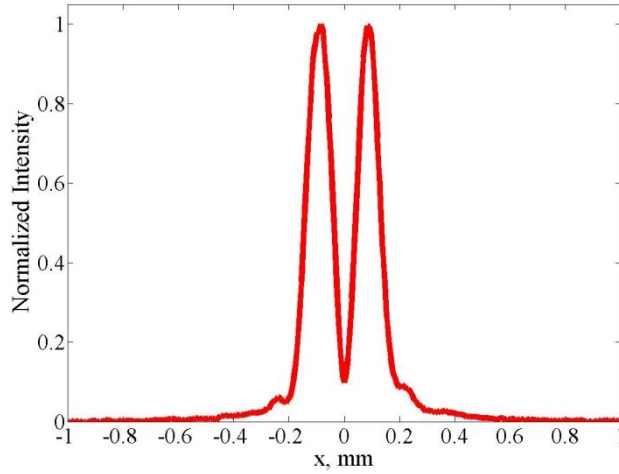


Figure 2.9: Far field intensity distribution of a beam with a  $\pi$  phase shift located at the beam center. This profile is measured at the focal plane of a 500 mm lens along the  $f_x$  axis shown in Fig. 2.2. Here the  $x$  scale on the horizontal axis refers to the lateral distance from the optical axis.

The null region in the center of the profile does not reach zero intensity because of the small spot size and finite resolution of the camera; for smaller incident beam sizes where the far field spot size is larger the null space between lobes can be seen reaching the noise floor.

### 2.2.2 Effects on Mode Conversion

While a simple one-dimensional step function in the refractive index profile indicates that in the far field a VPM has the same intensity distribution as a thin phase mask, in practical applications the phase mask will have some two-dimensional profile which may contain several sharp boundaries. In this case one must consider the possibility that diffraction from the multiple boundaries may result in an interference pattern which degrades the intensity distribution in the desired image plane. Such an interference pattern may not result in a significantly altered intensity profile by eye, but in applications such as mode conversion the conversion efficiency may suffer if, for instance, a desired null point is not perfectly achieved.

To investigate the effects on conversion efficiency, consider a set of two-dimensional binary masks which will be used to convert a Gaussian beam into higher order Hermite-Gaussian

and Laguerre-Gaussian modes. The first mask will consist of four sectors and the second one will consist of eight, with the phase between adjacent sectors shifted by  $\pi$ , as shown in Fig. 2.10. The four-sector mask will partially convert a Gaussian beam to a  $\text{TEM}_{11}$  mode and the eight-sector mask will partially convert the beam to the  $\text{LG}_{04}$  mode [59]. To determine the degree of conversion, note that the Hermite-Gaussian modes (and Laguerre-Gaussian modes) are mutually orthogonal; two normalized modes  $E_{n_1 m_1}$  and  $E_{n_2 m_2}$  are related by

$$\left| \iint E_{n_1 m_1}^* E_{n_2 m_2} da \right|^2 = \delta_{n_1 n_2} \delta_{m_1 m_2}. \quad (2.8)$$

Here  $a$  is area,  $(*)$  denotes complex conjugation and  $\delta$  is the Kronecker delta. The fields for each mode are given by [60]:

$$E_{nm}^{HG}(x, y, z) = E_0 \frac{w_0}{w(z)} H_n \left( \frac{\sqrt{2}x}{w(z)} \right) H_m \left( \frac{\sqrt{2}y}{w(z)} \right) e^{\frac{-(x^2+y^2)}{w^2(z)}} e^{-i \left( kz - (1+n+m) \arctan \left( \frac{z}{z_0} \right) + k \frac{x^2+y^2}{2R(z)} \right)} \quad (2.9)$$

$$E_{nm}^{LG}(r, \varphi, z) = E_0 \frac{w_0}{w(z)} \left( \frac{\sqrt{2}r}{w(z)} \right)^{|m|} L_n^{|m|} \left( \frac{2r^2}{w^2(z)} \right) e^{\frac{-r^2}{w^2(z)}} e^{im\varphi} e^{-i \left( kz - (1+2n+|m|) \arctan \left( \frac{z}{z_0} \right) + k \frac{r^2}{2R(z)} \right)} \quad (2.10)$$

Here  $w$  is the radius of the beam (defined as the half width at  $1/e^2$  of the beam intensity),  $H_n$  is the Hermite polynomial of the physicist's form of order  $n$ ,  $k$  is the wavenumber,  $z_0$  is the Rayleigh length, and  $R$  is the radius of curvature of the wavefront.

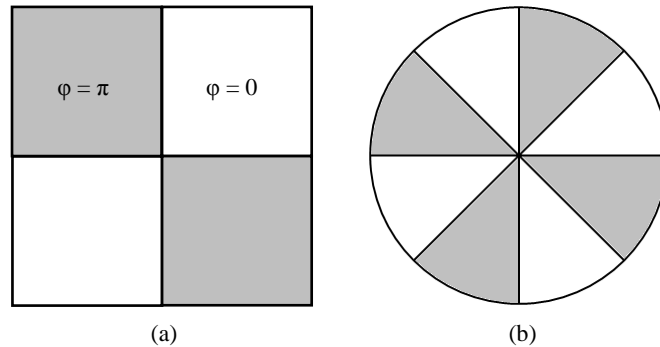


Figure 2.10: Binary phase distribution for (a) a four-sector and (b) eight-sector mode converting phase mask.

Table 2.1: The Hermite and Laguerre polynomials [61,62].

$n$	$H_n(x)$	$L_n^m(r)$
0	1	1
1	$2x$	$1+m-x$
2	$4x^2-2$	$1/2(2+3m+m^2-(4+2m)x+x^2)$
$n$	$(-1)^n e^{x^2} \frac{d^n}{dx^n} e^{-x^2}$	$\frac{x^{-m} e^x}{n!} \frac{d^n}{dx^n} (e^{-x} x^{n+m})$

$L_n^m$  is the associated Laguerre polynomial of order  $n$ . The first few Hermite and Laguerre polynomials are listed in Table 2.1. Note that the lowest order polynomial in both cases is one, so the lowest order mode is a standard Gaussian beam.

Since a Gaussian beam transmitted through a multi-sector VPM acquires local phase change it will thus not have the same field distribution as the lowest order mode for either the Hermite-Gaussian modes or the Laguerre-Gaussian modes and conservation of energy will therefore dictate that some energy will be coupled into higher order modes. Mathematically this is equivalent to stating that the transmitted beam is a linear combination of each mode in the basis set (where the Hermite polynomials represent a basis set in Cartesian coordinates and the Laguerre polynomials represent a basis in polar coordinates). The fraction of energy coupled into a given higher order mode is given by

$$\eta = \frac{\left| \iint E_{nm}^* E_{00} T da \right|^2}{\iint |E_{00} T|^2 da \cdot \iint |E_{nm}|^2 da}, \quad (2.11)$$

where  $T$  is the transmittance function of the sector masks and the denominator serves as a normalization factor. Eq. 2.11 determines the overlap of the field distribution with a given mode, with 100% overlap corresponding to 100% of the energy being coupled into that mode. If

the coupling into a desired mode is less than 100% then the remaining energy can be considered as losses in mode purity.

When comparing beams however it should be noted that higher order modes have, obviously, a different distribution of energy compared to a Gaussian beam. Therefore for a higher order mode with the same radius as a Gaussian beam, the size of the bucket which contains the same amount of energy will generally be different. Thus the coupling of a Gaussian beam of radius  $w$  into a higher order mode will depend on the size of the higher order mode, which will be denoted here with a “radius” of  $u$ . This radius corresponds to the radius of the Gaussian kernel which is being multiplied by the Hermite or Laguerre polynomials in Eqs. 2.9 and 2.10. Therefore the fraction of energy coupled into a mode becomes

$$\eta(u, w) = \frac{\left| \iint E_{nm}^*(u) E_{00}(w) T da \right|^2}{\iint |E_{00}(w) T|^2 da \cdot \iint |E_{nm}(u)|^2 da} . \quad (2.12)$$

To determine whether a given mode radius is the correct one to use in Eq. 2.12, consider a Gaussian beam with a radius  $w$  of 2 mm and a transmittance function  $T = 1$ . Because the Gaussian beam is a pure mode if it were modeled as a superposition of the various Laguerre-Gaussian modes Eq. 2.12 would give a “coupling efficiency” of 100% if it were matched to the lowest order Laguerre-Gaussian mode with a radius  $u$  of 2 mm with 0% of the energy coupled into the other modes. However, it is possible to model this Gaussian beam as a superposition of Laguerre-Gaussian modes for which the radius  $u$  is 1 mm. In this case the Eq. 2.12 states that 64% of the energy is coupled into the lowest order Laguerre-Gaussian mode and the remaining energy is distributed among the higher order modes. The lowered coupling efficiency is caused by the mismatch between the energy distribution of the original Gaussian beam and the lowest order mode that is being fit to that Gaussian beam, even though both of these modes are



Gaussian distributions. By adjusting the radius  $u$  of the modes that are used to fit a given field distribution the overlap integral (Eq. 2.12) will change, and typically for some radius one mode in the basis set will have a much larger overlap with the field distribution than the other modes. When the overlap integral with this mode is maximized by proper choice of  $u$  then the correct radius has been determined which should be used to model the field distribution. Thus in the previous example with the Gaussian beam, by adjusting  $u$  to maximize Eq. 2.12 for the lowest order Laguerre-Gaussian mode, one would find that  $u$  should equal  $w$ , exactly as expected since the Gaussian beam is a pure mode. If however the dominant mode were unknown and the radius  $u$  was chosen to maximize for instance the  $LG_{20}$  mode instead of the  $LG_{00}$  mode, the coupling efficiency into the  $LG_{20}$  mode would be 13.4% at this value for  $u$ . If however the field distribution was modeled using the full superposition of the Laguerre-Gaussian modes with this value for  $u$  one would find that the coupling efficiency into the  $LG_{00}$  mode would be 79.1%, which is larger than the  $LG_{20}$  mode, indicating that the wrong mode was chosen to optimize  $u$ .

This variation in conversion efficiency achieved by improperly choosing the mode radius can be used as a tool to determine the quality of a given phase mask.

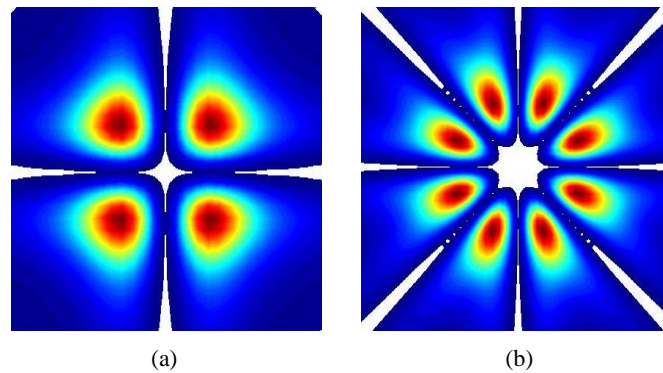


Figure 2.11: Simulated far field intensity profile of a beam passing through (a) a four-sector and (b) an eight-sector mode converting phase mask.

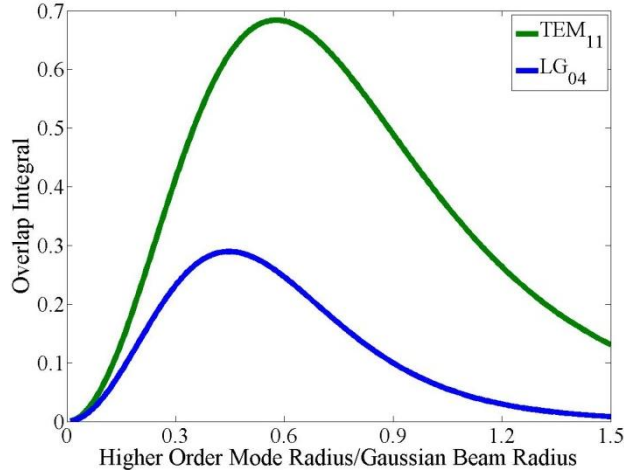


Figure 2.12: Simulated coupling efficiency of a beam after passing through a four-sector and eight-sector mask into the TEM<sub>11</sub> mode and LG<sub>04</sub> mode for different mode radii. The correct mode radius for determining the overlap of the field distribution with the TEM<sub>11</sub> and LG<sub>04</sub> mode is 0.577 and 0.445 times the radius of the initial Gaussian beam, respectively.

This is done by first simulating the conversion efficiency for a perfect phase mask with a given transmittance function. For the four-sector mask and eight-sector mask the transmittance function is

$$T_4(x, y) = \text{sign}(x)\text{sign}(y)\exp(i\varphi_{avg}) \quad (2.13)$$

$$T_8(x, y) = \text{sign}(x)\text{sign}(y)\text{sign}(x+y)\text{sign}(x-y)\exp(i\varphi_{avg}), \quad (2.14)$$

where the average phase incursion  $\varphi_{avg}$  may be set to zero without loss of generality. In the far field the ideal intensity profile of a Gaussian beam passing through these masks is shown in Fig. 2.11. The overlap of the field distribution after passing through the masks with the higher order modes is shown in Fig. 2.12. The four-sector mask has a maximum overlap of 68.4% with the TEM<sub>11</sub> mode when  $u/w = 0.577$  and the eight-sector mask has a maximum overlap of 29% with the LG<sub>04</sub> mode when  $u/w = 0.445$ . These radii are the correct radii to use when modeling the field distribution with the full superposition of Hermite-Gaussian or Laguerre-Gaussian modes. However, the quality of an actual phase mask can be determined by fitting the Hermite-Gaussian modes and Laguerre-Gaussian modes of different radii to the experimental field distribution and

comparing the overlap integral curve to the curve for the ideal phase mask. If there is a deviation in the experimental curve from the ideal curve, whether the overlap is larger or smaller, then the actual phase mask is coupling more energy into undesired modes than expected, indicating that the actual phase mask does not produce the desired phase profile.

To verify this model VPMs were produced with the appropriate phase profiles, which were tested and polished to the proper thickness using the techniques described previously. Note that though there is a finite transition region between the sectors during the recording, the width of this zone has a negligible effect. After achieving a  $\pi$  phase shift between adjacent sectors the masks were then illuminated with a collimated He-Ne laser at 632.8 nm with a diameter of 6.6 mm and the far field intensity distribution was examined by focusing the transmitted beam through a lens. As shown in Fig. 2.13, excellent visual agreement with the theoretical intensity distribution is observed. In order to quantitatively relate the theoretical field distribution and experimental intensity distribution it is necessary to convert the theoretical field distribution to an intensity distribution.

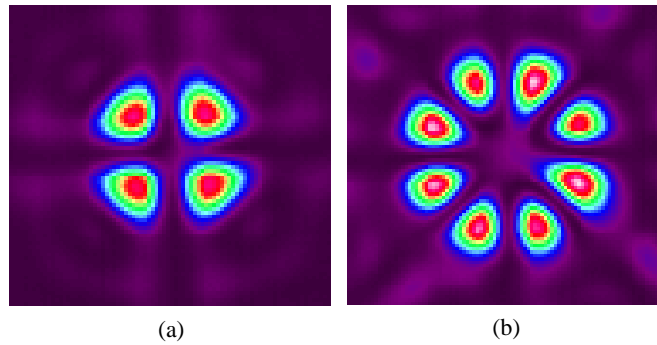


Figure 2.13: Experimental far field intensity distribution of a beam passing through a four-sector (a) and eight-sector (b) mode-converting VPM.

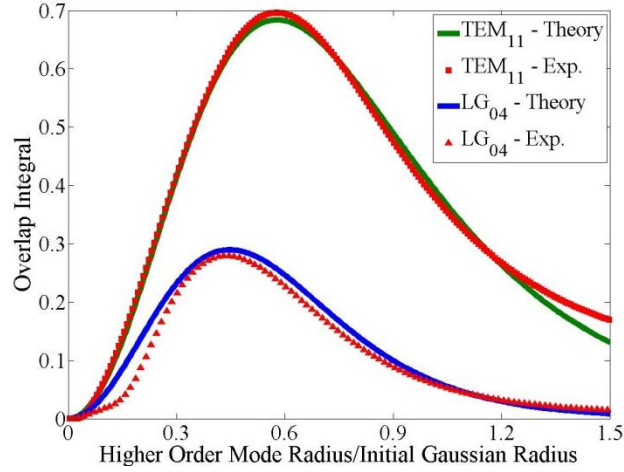


Figure 2.14: Overlap integral of a Gaussian beam after passing through a VPM with higher order modes of different radii. Solid lines represent the ideal overlap integral and dotted lines represent the integral with the experimental data shown in Fig. 2.13.

Modifying Eq. 2.12 to account for this gives an overlap integral of the form

$$\eta(u, w) = \frac{\left| \iint |E_{nm}^*(w)| \cdot |E_{00}(u)T| da \right|^2}{\iint |E_{00}(u)T|^2 da \cdot \iint |E_{nm}(u)|^2 da}, \quad (2.15)$$

where the modulus of the field is the square root of the intensity. Fig. 2.14 shows the theoretical and experimental overlap integrals for the relevant modes with different radii, with good overall agreement between theory and experiment. Note that the overlap integral with the  $TEM_{11}$  mode is larger than the ideal case, especially as the radius  $u$  is increased; this indicates that there is more energy being coupled into this mode than would be expected for an ideal four-sector binary phase mask. Thus the experimental mask is not quite ideal, with the deviation being caused primarily by the finite transition region between adjacent sectors. The eight-sector mask shows a similar behavior when coupling into the  $LG_{04}$  mode. However, the location of the correct radius (the peak overlap) matches the theoretical predictions, and at the correct radius there is very good agreement between the experimental and theoretical coupling efficiency. Therefore VPMs can

successfully convert between different Hermite-Gaussian and Laguerre-Gaussian modes with the same efficiency as an ideal phase mask under the IPMA.

### 2.3 Summary

Volume phase masks recorded in thick media will exhibit different properties than thin phase masks if the phase mask contains high spatial frequencies or if the intended use of the mask is in the near field. However, for low spatial frequency elements, particularly in the far field, there is no difference in the beam profile created by a VPM as opposed to a traditional phase mask. This applies not only to intensity profiles but directly to field, as the mode conversion exhibited by a VPM is the same as that of an ideal phase mask. Therefore VPMs may be used in the same applications as traditional phase masks, and with their higher robustness they may be used in systems requiring higher powers or temperatures than can safely be handled by traditional masks.

## CHAPTER 3: PROBABILISTIC PHASE MASKS

*Note: This chapter contains material which was published in the following works:*

*S. Mokhov, M. SeGall, D. Ott, V. Rotar, J. Lumeau, B. Zeldovich, and L. Glebov, "Direct recording of phase plates in holographic material with using of probabilistic amplitude masks," Digital Holography and Three-Dimensional Imaging JMA11 (2010).*

*M. SeGall, I. Divliansky, D. Ott, J. Lumeau, S. Mokhov, B. Zeldovich, and L. B. Glebov, "Beam shaping by volume phase structures in photo-thermo-refractive glass," Optics+Photonics 8843-6 (2013) (conference proceedings to be published)*

As seen in the previous chapter it is possible to make fairly simple masks which, despite having any possible geometric shape, still induce a constant phase shift between the exposed and unexposed regions. However, in order to be a useful technology a phase mask with an arbitrary phase profile should be able to be produced, including phase gradients, sharp transitions, and any other desired features. To create such an arbitrary spatial dependence in the phase for a mask recorded in PTR glass it is necessary to alter the local intensity of the UV light that is incident during the recording of the phase element. As described in Chapter 1 there are a number of techniques which may accomplish this goal; here the contact copy technique with a broadband incoherent source and an appropriate amplitude mask will be used. Conventional amplitude masks however are inherently binary, being either opaque or transparent. Furthermore, diffraction from sharp transition regions in the mask during recording will result in a partially washed out illumination profile. This partially washed out profile however is the key to producing a grayscale phase mask. Here a new type of amplitude mask, which will henceforth be referred to as a probabilistic amplitude mask, which is specifically designed to utilize the diffraction effects during recording, will be used.

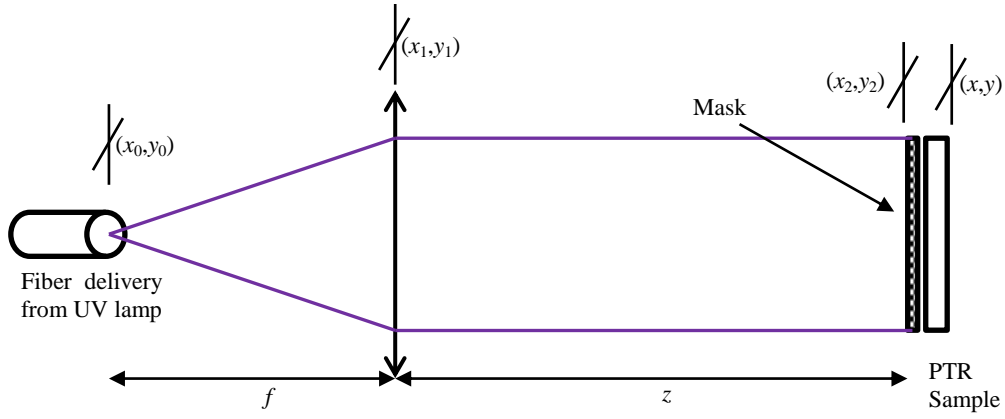


Figure 3.1: Recording system for producing grayscale phase masks from an amplitude mask.

### 3.1 Recording with Amplitude Masks

Before considering the profile of an amplitude mask used to create a phase mask it is necessary to determine what phase profile will be recorded into the PTR substrate when an arbitrary amplitude mask is used. The PTR sample was illuminated by a UV mercury lamp (Dymax Bluewave 200) in the recording system shown in Fig. 3.1. The lamp delivered incoherent broadband UV radiation from 300 nm to 400 nm, which covers the photosensitive region of the PTR glass [39,63], and emitted it via a 5 mm diameter wide-aperture fiber. The broadband, incoherent source was deliberately chosen to eliminate interference effects from any diffracting pixels in the mask. The emitted beam was then collimated and illuminated the amplitude mask and PTR sample. To avoid reflections in the system index-matching fluid was placed between the amplitude mask and the PTR sample, and the metal surface of the mask is the surface which was in contact with the sample.

As no element in this system is polarization sensitive it may be modeled using scalar diffraction theory [43]. The illumination from the fiber can therefore be considered as coming

from a collection of point sources over the fiber area, which will be taken to be in the  $(x_0, y_0)$  plane. The emitted wave from a single point source in this plane will take the form of [43]

$$U(x_1, y_1) = \frac{e^{ik_0 f}}{i\lambda f} \exp\left(i \frac{\pi}{\lambda f} [(x_1 - x_0)^2 + (y_1 - y_0)^2]\right) \quad (3.1)$$

in the plane of the lens. Here  $f$  is the focal length of the lens,  $\lambda$  is the free-space wavelength, and  $k_0$  is the free-space wavenumber. After passing through the lens the scalar field is multiplied by the amplitude transmittance function of the lens, given by

$$t_{lens} = \text{circ}\left(\frac{2\sqrt{x_1^2 + y_1^2}}{D}\right) \exp\left[\frac{-i\pi}{\lambda f} (x_1^2 + y_1^2)\right], \quad (3.2)$$

where *circ* is the circle function defined in [43] and  $D$  is the lens diameter. After propagating a distance  $z$  after the lens the field is given by

$$U(x_2, y_2) = \frac{e^{ik_0 z}}{i\lambda z} \iint t_{lens} U_1(x_1, y_1) \exp\left(i \frac{\pi}{\lambda z} [(x_2 - x_1)^2 + (y_2 - y_1)^2]\right) dx_1 dy_1. \quad (3.3)$$

In general Eq. 3.3 must be solved numerically. However, if the diameter of the lens is larger than the emitted light cone so that all of the energy is collected then the lens may be treated as infinite, in which case Eq. 3.3 has the analytical solution of

$$U(x_2, y_2) = \frac{e^{ik_0(f+z)}}{i\lambda f} \exp\left[\frac{i\pi}{\lambda f} \left(1 - \frac{z}{f}\right) (x_0^2 + y_0^2)\right] \exp\left[-i \frac{2\pi}{\lambda f} (x_2 x_0 + y_2 y_0)\right]. \quad (3.4)$$

Note that this is just a tilted plane wave, which is expected when a point source is located at the focal plane of a lens. Experimental observations indicate that a finite lens which collimates the majority of the light cone will create a nearly uniform intensity distribution at the center of the beam and a more complicated profile towards the edges. However, only the center of the beam



was used during the recording of a phase mask so the beam may effectively be treated as a plane wave after being collimated by the lens.

The angle at which the plane wave propagates can be determined from the spatial frequencies:

$$\sin \theta_{x,y} = k_{x,y} \lambda . \quad (3.5)$$

Here  $k_{x,y}$  is the spatial frequency along the relevant axis. The angle of propagation along the x-axis is therefore  $\theta_x = \arcsin(x_0 / f)$ , and the angle of propagation along the y-axis has the same form. Note that the criterion  $\sqrt{x_0^2 + y_0^2} \ll f$  must be satisfied for the assumption of a plane wave to be valid. If this criterion is not satisfied the lens will image the point to a plane according to the lens equation, resulting in a non-uniform intensity distribution depending on the propagation distance  $z$ .

Having propagated the recording beam to the amplitude mask via Eq. 3.4, the actual design of the mask must be taken into account. The amplitude mask is not an infinitely thin set of apertures but rather a layer of metal bonded to a glass or fused silica substrate. As the metal surface is the surface in contact with the PTR sample the recording beam must first pass through the glass substrate before encountering the amplitude mask. Using Snell's law and Eq. 3.5, the refraction at the air/substrate interface reduces the spatial frequencies by a factor of  $n$ :

$$f_{x,y,air} \lambda = \sin \theta_{air} = n \sin \theta_m = n f_{x,y,m} \lambda . \quad (3.6)$$

Here  $n$ ,  $f_{x,y,m}$  and  $\theta_m$  are the refractive index, spatial frequency, and propagation angle in the substrate, respectively. Rewriting Eq. 3.4 to account for refraction gives the field as

$$U(x_2, y_2) = \frac{e^{ik_0(f+z)}}{i\lambda f} \exp \left[ \frac{i\pi}{\lambda f} \left( 1 - \frac{z}{f} \right) (x_0^2 + y_0^2) \right] \exp \left[ -i \frac{2\pi}{n\lambda f} (x_2 x_0 + y_2 y_0) \right] . \quad (3.7)$$

Since  $U$  is a plane wave, when propagating the beam through the thickness of the substrate the only effect on the field is to accumulate a phase factor:

$$U(x_3, y_3) = \frac{e^{ik_0(f+z+nd)}}{i\lambda f} \exp\left[\frac{i\pi}{\lambda f}\left(1 - \frac{z}{f} - \frac{d}{nf}\right)(x_0^2 + y_0^2)\right] \exp\left[-i\frac{2\pi}{n\lambda f}(x_3x_0 + y_3y_0)\right]. \quad (3.8)$$

Here the propagation distance is  $d = d_s (\cos \theta_{x,m} \cos \theta_{y,m})^{-1}$ , where  $d_s$  is the physical thickness of the substrate. After passing through the amplitude mask the field is multiplied by the amplitude transmittance function of the mask  $t_{mask}$  and then propagates into the PTR sample. At a depth  $z_{PTR}$  into the sample the field is therefore

$$U(x, y, z_{PTR}) = \tilde{C} \iint t_{mask}(x_3, y_3) e^{\frac{i\pi}{n\lambda z_{PTR}}(x_3^2 + y_3^2)} e^{\frac{-i2\pi}{n\lambda}\left[\left(\frac{x}{z_{PTR}} + \frac{x_0}{f}\right)x_3 + \left(\frac{y}{z_{PTR}} + \frac{y_0}{f}\right)y_3\right]}, \quad (3.9)$$

which can be written as a Fourier transform:

$$U(x, y, z_{PTR}) = \tilde{C} \mathcal{F} \left\{ t_{mask}(x_3, y_3) \exp\left(\frac{i\pi}{n\lambda z_{PTR}}(x_3^2 + y_3^2)\right) \right\} \bigg|_{f_x = \frac{x_0}{n\lambda f} + \frac{x}{n\lambda z_{PTR}}, f_y = \frac{y_0}{n\lambda f} + \frac{y}{n\lambda z_{PTR}}} \quad (3.10)$$

The complex amplitude term in Eqs. 3.9 and 3.10 is

$$\tilde{C} = \frac{-e^{ik_0(f+z+nd+nz_{PTR})}}{\lambda^2 n f z_{PTR}} \exp\left(\frac{i\pi}{\lambda n z_{PTR}}(x^2 + y^2)\right) \exp\left[\frac{i\pi}{\lambda f}\left(1 - \frac{z}{f} - \frac{d}{nf}\right)(x_0^2 + y_0^2)\right]. \quad (3.11)$$

The intensity profile produced by this source point at a given plane in the PTR sample is the squared modulus of Eq. 3.10. Because the lamp is an incoherent source the total intensity distribution at a given plane in the PTR sample is the integral of the intensity distributions produced by each source point in the  $(x_0, y_0)$  plane, multiplied by their relative intensities and absorption in the PTR sample:

$$I(x, y, z_{PTR}) = \iiint |U(x, y, z_{PTR})|^2 I(x_0, y_0, \lambda) 10^{-\alpha(\lambda)z_{PTR}} dx_0 dy_0 d\lambda. \quad (3.12)$$

In order to determine the change in refractive index induced in the glass, a final step is needed. As shown in Chapter 1 the refractive index change in the glass is nonlinear with respect to illuminating dosage. Combining Eqs. 3.12 and 1.1 give the spatially dependent refractive index profile:

$$\Delta n(x, y, z_{PTR}) = \frac{n_s I(x, y, z_{PTR}) t_{\text{exp}}}{\varepsilon + I(x, y, z_{PTR}) t_{\text{exp}}} . \quad (3.13)$$

Here  $t_{\text{exp}}$  is the exposure time. This refractive index profile is dependent on the material properties of the glass and the baking parameters used so for modeling purposes it is necessary to empirically determine  $n_s$  and  $\varepsilon$ . The phase profile that is induced in the glass is then

$$\varphi(x, y) = \frac{2\pi \int_0^{d_{PTR}} \Delta n(x, y, z_{PTR}) dz_{PTR}}{\lambda} , \quad (3.14)$$

where  $d_{PTR}$  is the physical thickness of the PTR sample.

### 3.1.1 Ideal Amplitude Masks

To produce a smoothly varying phase profile in PTR glass using the contact copy method a grayscale amplitude mask is required. As amplitude masks have a transmittance function between zero (opaque) and one (transparent), the phase profile which is to be recorded in the glass must be normalized in order to be contained within this range:

$$\varphi_{\text{norm}} = \frac{\varphi - \varphi_{\min}}{\varphi_{\max} - \varphi_{\min}} . \quad (3.15)$$

Eq. 3.15 will always normalize the desired phase profile such that the maximum phase to be recorded is set to one and the minimum phase is set to zero; strictly speaking this is not necessary if the total phase range is less than 1 radian, in which case the normalized phase should merely

be nonnegative. However, as will be discussed later, this formulation is necessary for probabilistic phase masks, so Eq. 3.15 will be used in all cases.

Consider now an ideal grayscale amplitude mask which can have an arbitrary transmittance profile with perfect resolution. If the refractive profile induced in the glass is a linear function of the exposing dosage, which is nearly the case for samples considered here, the amplitude mask should have an intensity transmittance profile of  $I_{mask} = 1 - \phi_{norm}$ , since PTR glass decreases its refractive index upon exposure and development. Using the system shown in Fig. 3.1, if the PTR sample were a very thin sample (only a few microns thick) then this ideal amplitude mask would perfectly create the desired phase profile in the glass. However, because the samples are typically several millimeters thick, diffraction effects from the amplitude mask must be taken into account. To investigate the effects of diffraction, consider two phase profiles: a parabolic profile which contains no sharp edges, and a sawtooth profile, which contains sharp edges and a large phase jump at these edges. Using Eqs. 3.10-3.15, where  $t_{mask} = \sqrt{I_{mask}}$ , the phase profiles were calculated in Matlab for a 1.5 mm sample over the wavelength range of 300-330 nm, assuming a linear response of the glass to dosage and taking into account the spectral response of the lamp and the wavelength-dependent absorption.

As shown in Fig. 3.2, the parabolic profile can be almost perfectly replicated. However, the sawtooth profile suffers from poor representation at the transition regions; the transition regions are over 10  $\mu\text{m}$  wide, the phase profile contains oscillations near the boundaries, and the minimum and maximum phase changes are larger than their ideal values. Thus for a volume phase mask to provide an accurate phase profile it is necessary to minimize the number of sharp phase transitions.

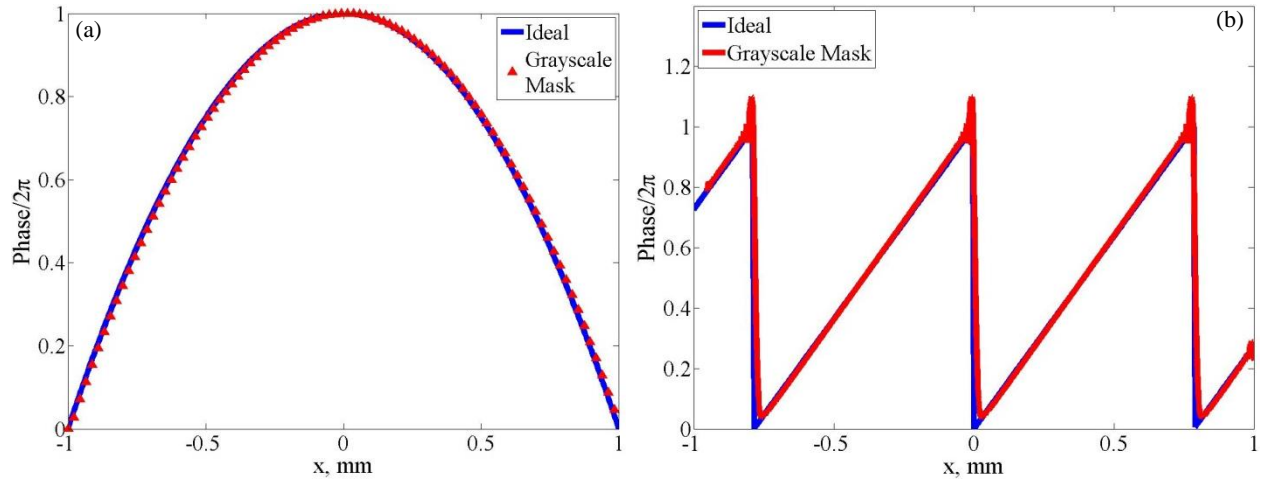


Figure 3.2: Simulated phase profile recorded into a 1.5 mm PTR sample for (a) a parabolic and (b) a sawtooth amplitude mask profile using the contact copy method.

If this is done then an ideal grayscale amplitude mask can generate the desired phase distribution in PTR glass with very good accuracy, allowing the volume phase mask to possess the same beam-shaping properties as a traditional phase mask.

### 3.1.2 Probabilistic Amplitude Mask

Since simulations of grayscale amplitude masks indicate that they can produce good quality representations of the desired phase distribution the question becomes how to produce such masks practically. Grayscale amplitude masks are produced commercially using photolithography in specialized materials such as high-energy-beam-sensitive (HEBS) glass [64-71]. During production, depending on the process and the substrate used to create the amplitude mask either a set of discrete gray levels will be produced [67,68] or a continuous gray-level profile will be implemented [69-71]. In either case a high level of precision is needed, in addition to a specialized substrate. This makes grayscale amplitude masks very expensive, with a 25 x 25 mm mask costing at least 15 times as much as a traditional chrome-on-quartz mask of the same size. As this costliness makes grayscale amplitude masks impractical for most research applications a

cheaper method is desirable, even if the phase profile is somewhat degraded. If resolution is not critical then the amplitude mask can be printed onto a UV-transparent film using a high-end laser printer, with the gray levels being limited to the gray levels of the printer. However, most printers cannot achieve a resolution of more than 1200 dpi, limiting the feature size to approximately 20  $\mu\text{m}$  at best. In order to achieve higher resolution (and therefore more closely match the desired phase profile), the new type of amplitude mask, the probabilistic mask, using chrome-on-quartz substrates was used here.

Probabilistic masks were designed by considering the local phase change compared to the maximum phase change. A quasi-random distribution of opaque and transparent pixels were then generated in that region so that the number of transmitting pixels equals the local phase, e.g., if the local phase shift should be  $\pi$  and the maximum phase shift across the entire mask is  $2\pi$  then half of the pixels in the local region are transparent. In order to produce a quasi-grayscale mask each pixel should be small enough for diffraction effects to become significant so that the area immediately surrounding a transparent pixel will receive approximately the same dosage as the transmitting pixel area. Since the number of transmitting pixels is based on the desired local phase change this results in the entire region being exposed with approximately the same dosage, which is higher or lower depending on the desired local phase.

Fabrication of a probabilistic mask was performed in a similar manner to a grayscale amplitude mask; the desired phase profile was first normalized via Eq. 3.15, the square root of this normalized phase profile was taken, and the profile was then pixelated. An array of random numbers between 0 and 1 was then generated with each random number corresponding to one pixel.

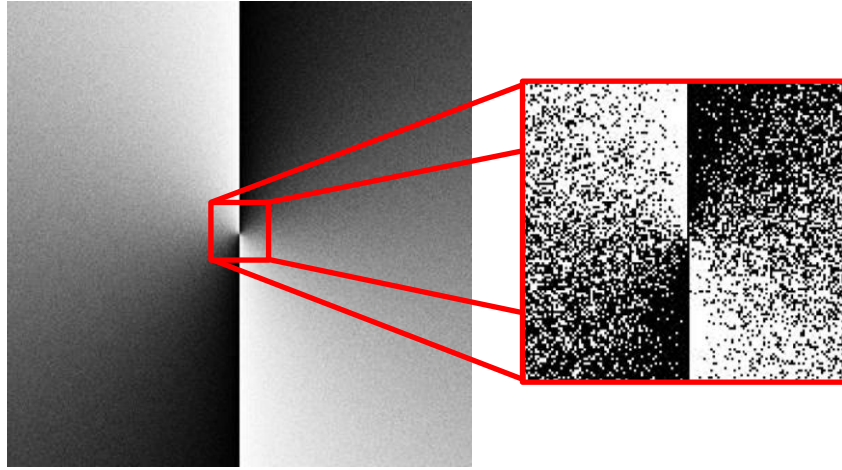


Figure 3.3: A probabilistic mask creates a quasi-grayscale intensity distribution via diffraction from micro-apertures. The transparency of a given aperture is based on the probability that the local desired phase at a given point is greater than a random number.

If the normalized phase at a given pixel in the phase distribution was greater than its matching random number then the corresponding pixel in the amplitude mask was chosen so that the PTR sample will have a higher refractive index in this region. Since PTR decreases its refractive index upon exposure and development the pixel in the amplitude mask was made opaque.

As an example of this procedure, suppose that the desired normalized phase at pixel number 34 in the normalized phase array is 0.75 and the desired phase at pixel number 35 is 0.78. Further, suppose that the matching random numbers in the random number array are 0.1 and 0.79, respectively. Because  $0.75 > 0.1$  and  $0.78 < 0.79$ , the value of the amplitude mask at pixel 34 in the amplitude mask array would be set to 0 (opaque) and at pixel 35 it would be set to 1 (transparent). The entire amplitude mask array then consists of quasi-randomly distributed opaque and transparent pixels, as shown in Fig. 3.3, which alter the local exposing beam intensity to create a quasi-continuous phase distribution in the PTR glass. Since the transparency of a given pixel in the amplitude mask array equals the probability that a random number is greater than the desired normalized phase at its corresponding pixel, these masks are denoted

probabilistic masks. Note that these values in the amplitude mask correspond to the values of the mask once it is produced, and care must be taken when designing the amplitude mask to ensure this outcome. If for instance the mask-writing system (whether an e-beam system or some other system) writes on a value of 0 (i.e. makes that pixel transparent) then the designed mask array should have each value reversed so that the final mask is as desired. Since each system is different it is necessary to determine how the amplitude mask will be written and adjust the amplitude mask array accordingly.

A notable difference between the probabilistic mask and the grayscale amplitude mask is that for the probabilistic mask it is necessary to take the square root of the normalized phase profile, whereas for a grayscale amplitude mask this is not done. This difference is caused by the difference in representation of the phase profile; if the photosensitivity of the recording material is linear with respect to intensity then the grayscale amplitude mask should match the desired phase pattern. Probabilistic masks however are always either opaque or transparent; it is impossible for them to match the phase profile.

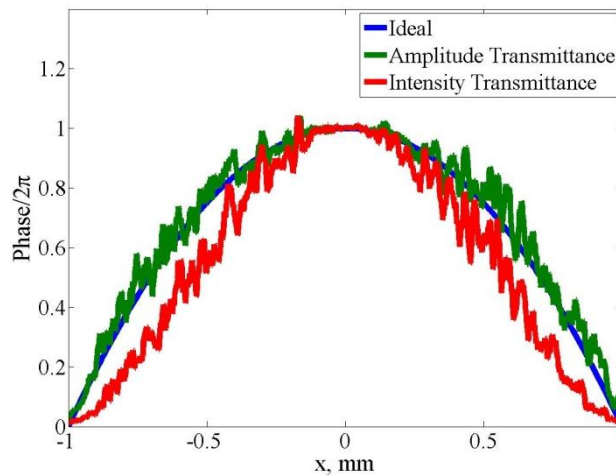


Figure 3.4: Simulated phase distributions produced by probabilistic masks which replicate the amplitude transmittance function and the intensity transmittance function of a grayscale amplitude mask.



In order to produce the pseudo-grayscale levels in the sample it is necessary to utilize diffraction to illuminate the regions surrounding the transparent pixels, which is governed by the electric field rather than the intensity. Therefore the probabilistic mask should replicate the amplitude transmittance function of a grayscale amplitude mask rather than the intensity transmittance function. As shown in Fig. 3.4, if this is not done then the recorded phase profile will not match the desired phase profile.

### *3.1.3 Profile Optimization*

When fabricating probabilistic masks it is important to create a mask which will provide a profile that is as close to the desired phase profile as possible. For simple binary masks one need only design the appropriate grid shape with the size of the pixels being relatively unimportant. For more general profiles however, this will not suffice. All amplitude masks used in this thesis were manufactured using a Leica EBPG5000+ e-beam, which can create features less than 100 nm across via direct writing. However, the amplitude mask itself is a fused silica substrate with a layer of chrome and photoresist bonded to it. After the e-beam illuminated the photoresist it was then chemically developed, during which the exposed photoresist and chrome were removed. The combination of minimum dosage needed for full resist development and parasitic undercutting at the edge of the exposed regions added a minimum of 200 nm to the width of an exposed pixel, which effectively limited the size of the pixels to one micron or larger in order to have opaque and transparent pixels with approximately the same size.

To determine the effects of pixel size consider again the parabolic and sawtooth profiles that were previously simulated assuming a linear response of the PTR glass with pixel sizes ranging from 1  $\mu\text{m}$  to 10  $\mu\text{m}$ .

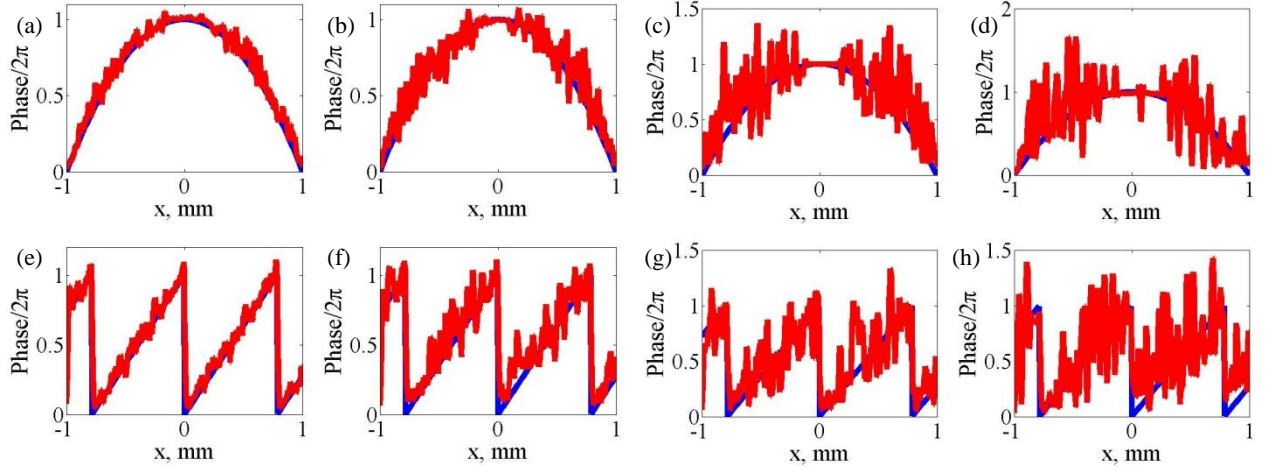


Figure 3.5: Phase profiles recorded by probabilistic masks with pixel sizes of {(a), (e)} 1  $\mu\text{m}$ , {(b), (f)} 2  $\mu\text{m}$ , {(c), (g)} 5  $\mu\text{m}$ , and {(d), (h)} 10  $\mu\text{m}$ .

As shown in Fig. 3.5, in all cases there are fluctuations from the desired phase profile caused by non-uniform illumination, as the light passing through the apertures does not uniformly redistribute energy when diffracting. Pixel sizes of 10  $\mu\text{m}$  or larger give a poor overall representation of the phase profile for both the parabola and the sawtooth pattern, while pixel sizes on the order of 2-5  $\mu\text{m}$  work reasonably well in that the general profile is followed. However, for both profiles the best representation is achieved with 1  $\mu\text{m}$  pixels, though the sawtooth profile suffer from the same problems as the grayscale amplitude mask. This is unsurprising, as smaller pixels diffract more, improving the uniformity of the gray levels and thus more closely matching the profile of a grayscale amplitude mask. Also, with smaller pixels more are necessary to cover the entire phase profile, and as the transparency of the pixels is based on probability, more pixels increases the likelihood of the ratio of transparent to opaque pixels matching the desired local phase.

As pixel sizes of 1  $\mu\text{m}$  provide the best representation of the desired phase distribution this is the pixel size that was used for all elements demonstrated henceforth. However, the small fluctuations in the phase profile caused by the quasi-uniform illumination suggest that though

probabilistic masks provide a cheap alternative to grayscale amplitude masks they may also reduce the quality of the phase masks, especially wherever there is a phase discontinuity. To investigate this, consider a spiral phase mask, which contains only a single phase discontinuity as the phase changes from 0 to a multiple of  $2\pi$  and a Fresnel lens, which never has a phase change exceeding  $2\pi$  and contains a large number of discontinuities.

### 3.2 Spiral Phase Mask

Spiral phase masks are used to produce optical vortices, which are used in applications including optical tweezers [72], quantum cryptography [73], and beam converters [25]. A vortex exists in a beam if there is a phase singularity in the center of the beam and the beam carries orbital angular momentum. In such a case the beam intensity will be zero at the location of the singularity, and its equiphase surface is not planar but rather spirals about the optical axis. This results in an annular beam distribution which in the far field can be approximated using the Laguerre-Gaussian modes (Eq. 2.10). Of importance is the topological charge  $m$ ; a photon with topological charge  $m$  will have an orbital angular momentum of  $m\hbar$ . Note that the topological charge does not have to be an integer, but non-integer topological charges are unstable [74,75]. If the vortex beam interferes with a reference beam the fringe pattern will have a fork discontinuity at the location of the phase discontinuity, with the number of tines in the fork equaling the topological charge of the vortex plus one [76].

In order to produce an optical vortex of topological charge  $|m|$ , a spiral phase mask induces an azimuthal phase variation from 0 to  $2m\pi$ , with the sign of  $m$  determined by the helicity of the phase variation. Conventional transmitting spiral phase masks can in principle convert a Gaussian beam into the appropriate vortex beam with 100% efficiency, but they are

either produced with a liquid crystal spatial light modulator [72], limiting their use to low powers, or create the phase variation through local changes in the geometrical thickness of the phase mask [77,78]. Creating a smooth annular profile is difficult using thin films, as the standard methods of producing a thin film mask will result in a staircase profile, whereas creating a smooth profile in the surface of a glass substrate requires high precision etching.

To create a spiral phase mask in PTR glass, it was assumed that the glass has a nearly linear response to the exposure dosage, so the phase profile which will be encoded into the amplitude master has a phase profile of  $\varphi(r, \theta) = m\theta$ . For simplicity only the  $m = 1$  case will be considered here. From Eq. 3.15 the intensity distribution of the mask is then  $I_{mask}(r, \theta) = \theta / (2\pi)$ . Note that the profile  $I_{mask}(r, \theta) = 1 - \theta / (2\pi)$  produces the same spiral pattern but with opposite helicity. As the phase mask recorded in the PTR sample is a transmitting phase mask it can be used with a beam incident from either side, with the helicity observed by the beam on one side being the reverse of the helicity observed by a beam incident from the other side.

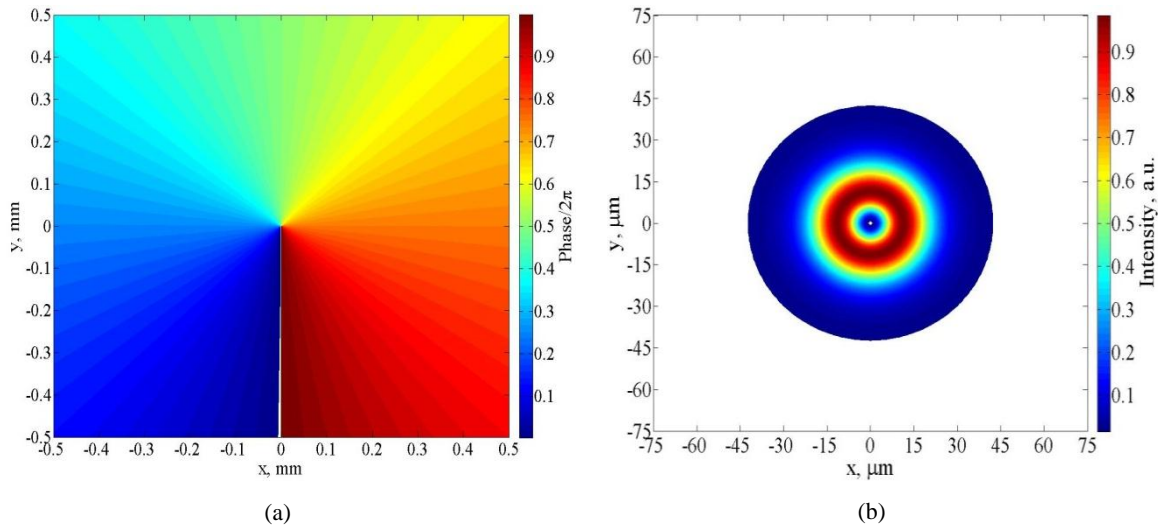


Figure 3.6: (a) Ideal phase distribution for an  $m = 1$  spiral phase mask and (b) the resulting far field distribution of a collimated 3 mm beam after acquiring the phase distribution and being focused by a 100 mm lens.

Therefore both helicities are encoded using either of the intensity profiles, and a separate phase mask with opposite helicity is not required. In either case, the ideal phase profile encoded will linearly vary with azimuthal angle, shown in Fig. 3.6a, and will produce an annular beam in the far field with 94% of the total energy contained in the annulus, as shown in Fig. 3.6b. As the edge of the annulus is arbitrary, here it is defined such that if the energy along a given circumference is at least 3% of the maximum energy along any circumference (to provide a good signal to noise ratio during experiments) then it is a measurable part of the ring. After finding the outermost points along each axis which satisfies this condition the total energy in the ring is calculated via a square which contains these outermost points to approximate a traditional detector.

During exposure the peak intensity was  $134 \text{ mW/cm}^2$  with an exposure time of 25 seconds; the PTR samples were baked at  $510^\circ\text{C}$  for 60 min. Based on the measured values of refractive index change for samples of different glass melts, the average empirical constants from Eq. 3.13 are  $n_s = 880 \text{ ppm}$  and  $\varepsilon = 3.76$ . While each glass sample will in practice have slightly different values for  $\varepsilon$  and potentially large differences in  $n_s$ , it was assumed for the purposes of modeling that these differences are negligible and the above constants were used throughout when calculating the refractive index distribution throughout a PTR sample. It should be noted that these empirical constants clearly show that the refractive index change is not linear over the range of zero intensity to peak intensity. Therefore to properly match the phase profile the constants for each sample should be taken into account and the profile of the amplitude mask back-calculated so that the desired phase profile is produced.

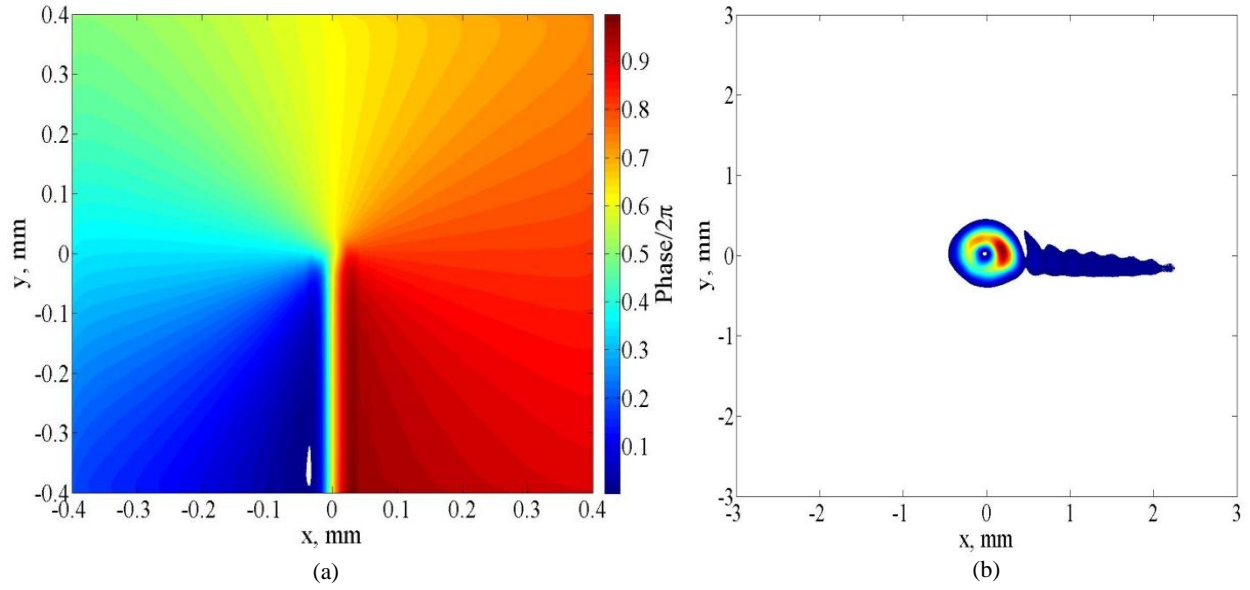


Figure 3.7: (a) Simulated spiral phase mask formed in PTR glass by the contact method and (b) the vortex profile 6 m after the phase mask. Due to computational limitations the profile in the far field could not be obtained with high resolution, but experimental evidence indicates that the profile does not significantly alter if focused by a lens.

However, because each glass melt is different, requiring a new amplitude mask to be produced each time, and because the deviation from linearity is expected to have only a small effect, it will be assumed throughout this thesis that the linear intensity profile is sufficiently accurate.

A simulation of the spiral phase mask generated by a grayscale amplitude mask, taking into account the nonlinearity of the refractive index change, is shown in Fig. 3.7. The azimuthal profile is maintained, though it is no longer a linear phase change due to the nonlinearity of the refractive index change. This nonlinearity will distort the beam profile, but as there is still a phase discontinuity at the center of the phase mask an optical vortex is still formed. The larger effect is caused by the transition region between 0 and  $2\pi$  phase shift; rather than an abrupt transition there is a finite width of a few tens of microns, resulting in a diffraction tail seen in Fig. 3.7b.

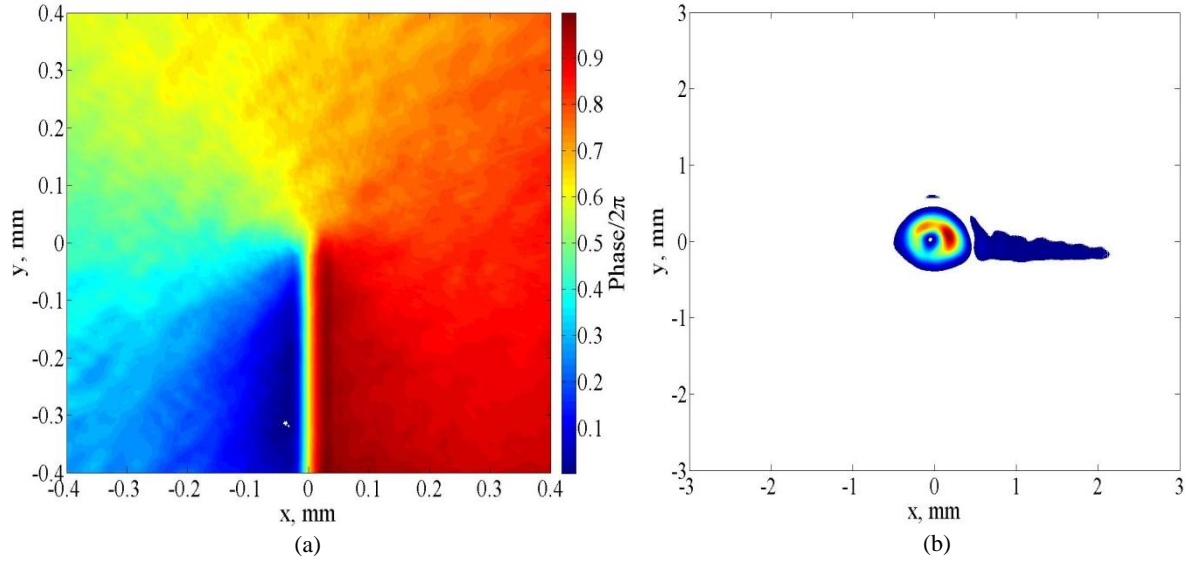


Figure 3.8: (a) Simulated phase profile induced by a probabilistic amplitude mask in the contact copy configuration and (b) the resulting beam profile 6 m after the mask.

This diffraction tail degrades the profile of the beam but contains relatively little energy; simulations of beams of different radii incident upon this phase mask indicate that approximately 92.5% of the energy is still contained within the annulus. Therefore though the overall profile is distorted an optical vortex containing nearly the amount of energy in the annulus as a perfect phase mask is still in principle possible.

Since a good quality vortex can ideally be produced with a grayscale amplitude mask, the probabilistic spiral phase mask was then simulated using the same recording procedure as the before, with collimated beams of different radii passing through the mask in order to determine the fraction of energy in the central ring. As shown in Fig. 3.8a, the probabilistic mask produces a phase pattern similar to the grayscale amplitude mask though it is not as smooth, with the splotches in the profile being caused by quasi-grayscale illumination. The transition region at the boundary between 0 and  $2\pi$  phase change is however almost identical to the grayscale amplitude mask; this is because at the boundary there is almost no difference between the two

amplitude mask profiles. As shown in Fig. 3.8b this phase mask produces a vortex profile similar to the profile in Fig. 3.7b, with a distorted annulus and a diffraction tail.

The fraction of energy in the ring is  $91 \pm 2\%$ , with the uncertainty being caused by numerical uncertainties and the probabilistic nature of the mask; a different probabilistic mask will produce a slightly different profile. Note that this ratio depends on the beam diameter; if the beam is sufficiently small a large fraction of energy will be diffracted by the transition region. Only beams with a diameter on the order of 1 mm or larger will have over 90% of the energy in the ring since only a small fraction of the beam is incident on the transition region.

To experimentally verify these simulations a probabilistic amplitude mask was placed in contact with a PTR sample in the recording configuration shown in Fig. 3.1 and a 100 mm plano-convex lens with a diameter of 50.4 mm was used as the collimating lens for the lamp. The mask and sample were placed approximately 300 mm behind the lens. After exposure and thermal development the sample had a refractive index change of 364 ppm and it was subsequently polished to 1.75 mm in order to achieve a  $2\pi$  phase shift at 633 nm.

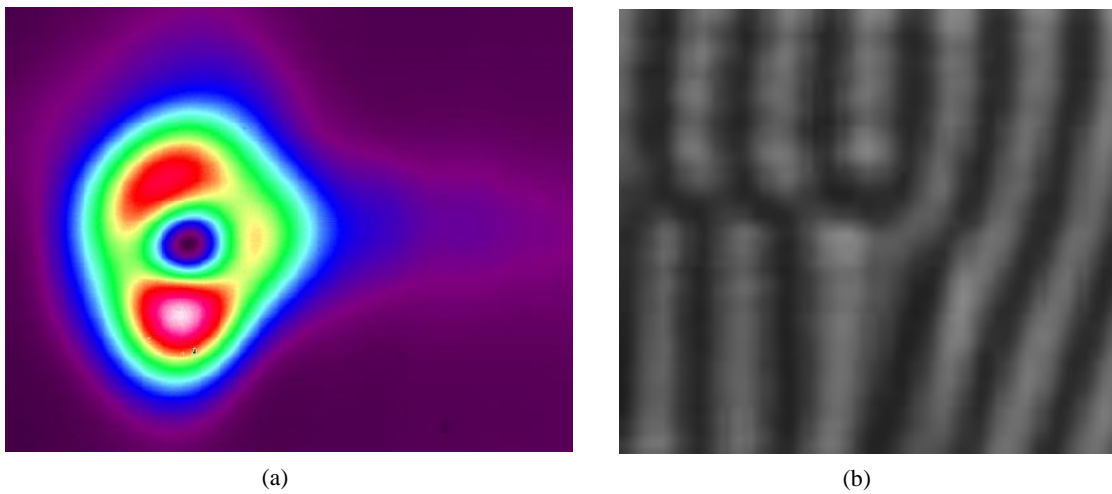


Figure 3.9: (a) Annular far field beam profile of a 1 mm beam passing through a probabilistic spiral phase mask, and (b) the fork dislocation produced by the mask in an interferometer. Because the interferometer is a double-pass interferometer the topological charge is doubled, producing three times in the fork.



As shown in Fig. 3.9a, after a 1 mm beam passed through the mask it achieved a nearly annular beam profile in the far field, along with a low energy diffraction tail. The fraction of the energy in the annulus is  $82 \pm 1\%$ , which was determined by comparing the power in the entire beam immediately after the sample to the far field power in the annulus. To measure the power in the annulus in the far field an iris diaphragm was used to block the diffraction tail. The measured fraction of energy in the annulus is fairly consistent with the simulations after accounting for fabrication errors in the probabilistic mask, indicating that annular profile can be produced with reasonable fidelity. To verify that the beam was truly a vortex beam the phase mask was placed in a double-pass interferometer (Zygo), and as shown in Fig. 3.9b the phase mask produces a fork dislocation in the interferogram. Because the interferometer is a double-pass interferometer the topological charge of the mask is doubled, and so the three lines shown in Fig. 3.9b are expected rather than the two-line pattern that would be observed in a single-pass interferometer. Therefore, probabilistic masks can produce optical vortices with approximately the same fidelity as a grayscale amplitude mask while being considerably cheaper and easier to fabricate.

### 3.3 Fresnel Lens

While VPMs can be used to create spiral phase masks with a reasonable conversion efficiency these masks only contain a single sharp phase transition and are otherwise smooth. In general however a phase mask may contain multiple phase discontinuities as well as a large phase gradient over small regions, with the Fresnel lens being a prime example.

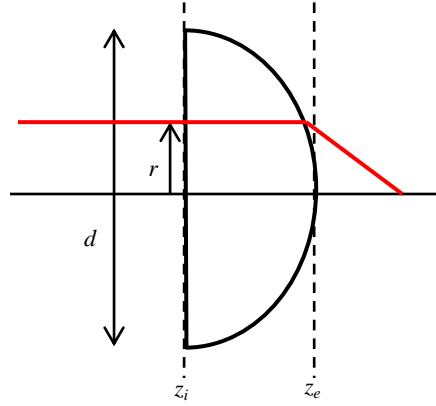


Figure 3.10: Diagram of a plano-convex lens in the configuration used to calculate the phase profile of a Fresnel lens.

As seen with the spiral phase mask even a single phase discontinuity cannot be perfectly represented, so due to the large number of phase discontinuities if Fresnel lenses it is unlikely that a VPM can be used to create a Fresnel lens of arbitrary size and focal length and still focus the majority of the energy to the focal point. To investigate the limitations of VPMS when trying to produce such elements, several plano-convex lenses are considered here.

To simulate a Fresnel lens first consider a collimated beam incident on a standard plano-convex lens of diameter  $d$ , with the first surface being flat and the second surface having a radius of curvature  $R$  as shown in Fig. 3.10 (this orientation was chosen as it is a common orientation for commercially available Fresnel lenses). Using geometrical optics the total optical path length that a ray a distance  $r$  from the center of the lens will incur from the incident plane  $z_i$  to the exit plane  $z_e$  is

$$OPL = n \left( \sqrt{R^2 - r^2} - \sqrt{R^2 - \frac{d^2}{4}} \right) + \frac{R - \sqrt{R^2 - r^2}}{\cos(\theta_e - \theta_m)}. \quad (3.16)$$

Here  $\theta_m = \arcsin(r/R)$  is the angle the normal of the back surface at a distance  $r$  makes relative to the optical axis and  $\theta_e = \arcsin(n \sin(r/R))$  is the angle of the ray refracted from the back

surface at a distance  $r$ , based on Snell's law. This optical path length is converted to phase by  $\varphi = 2\pi OPL / \lambda$  (modulo  $2\pi$ ); 632.8 nm is the wavelength of choice in all simulations shown here.

Using Eq. 3.16 lenses with focal lengths from 50 mm to 500 mm were simulated assuming that the original lens had a 25 mm diameter. However, this resulted in a large Fresnel lens, which was computationally intensive to model, and zones at larger radii, which were very small, were difficult to adequately sample. Since it is expected that there will be limitations on the focusing efficiency of a Fresnel lens regardless of numerical precision at large radii, only the central 2 mm diameter was considered, which is then illuminated with a collimated 1 mm beam. Due to computational limitations these calculations were restricted to a one-dimensional Fresnel lens and beam, but due to cylindrical symmetry these results apply for a two-dimensional lens as well.

As shown in Fig. 3.11a it is difficult for a grayscale amplitude mask to properly represent the multiple zones and sharp borders.

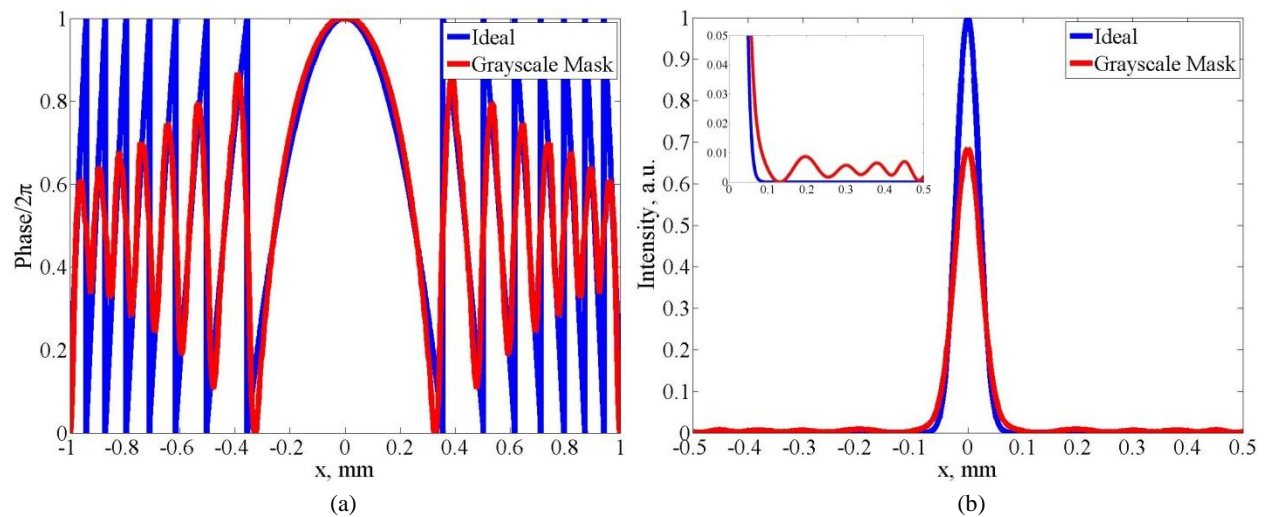


Figure 3.11: (a) Simulated phase profile of an ideal,  $f = 100$  mm Fresnel lens and a lens recorded with a grayscale amplitude mask and (b) the energy distribution in the focal plane of the lens.

Table 3.1: Focusing efficiency vs. focal length for simulated Fresnel lenses produced by the contact copy method using grayscale amplitude masks.

$f$ , mm	$\eta_{focus}$
50	66.0
100	83.0
200	93.3
300	96.3
500	98.8

In all cases the borders have a finite width rather than a sharp transition, and the smaller the Fresnel zone the worse the recorded profile is compared to the ideal profile. In addition, the nonlinearity of the refractive index change makes it impossible to match the ideal phase even in the central zone, though the more linear the refractive index change the better the matching will become.

Because the phase profile only partially matches the ideal profile the energy distribution in the focal plane changes as well, as shown in Fig. 3.11b. There is a reduction in the energy in the central lobe, which is also broadened. Also, there are several low energy rings surrounding the central lobe caused by diffraction from the transition regions. While the shape and energy distribution of these rings are dependent on the focal length of the lens they are nonetheless present for all lenses, including the 500 mm lens which contains only two zones.

The focusing efficiencies of the simulated lenses are listed in Table 3.1, where the focusing efficiency is defined as the fraction of energy in the central lobe (which is 1 by definition for an ideal Fresnel lens). Note that for the 300 mm lens and the 500 mm lens over 98% of the energy is contained within the central region before the first diffraction ring. However, in both cases the central spot has large wings. To eliminate the effect of the wings a Gaussian profile was fitted to the central region and the energy contained within the lobe bounded by the Gaussian fit was used to calculate the focusing efficiency.

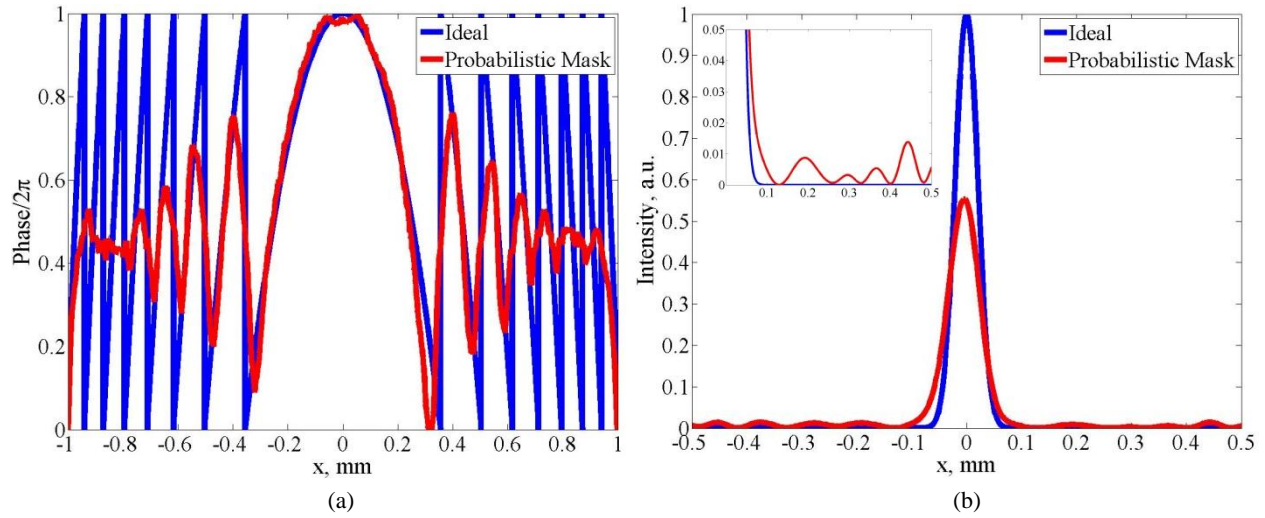


Figure 3.12: (a) Simulated phase profile of an ideal,  $f = 100$  mm Fresnel lens and the profile produced by a probabilistic amplitude mask and (b) the resulting energy distribution in the focal plane of the lens.

As can be seen from the table, in order to have a focusing efficiency larger than 90% the Fresnel lens must have a focal length of at least 200 mm for 1 mm incident beams, and for larger beams the focal length must be even larger to minimize the number of zones.

Even though it is clear that VPMs cannot produce Fresnel lenses with high fidelity, it is not clear how much the phase profile will be affected when a probabilistic phase mask is used. Therefore, as a probabilistic Fresnel mask was simulated in the contact copy configuration for a variety of focal lengths using the same recording parameters as the probabilistic spiral phase mask. As shown in Fig. 3.12a, the probabilistic Fresnel lens, while producing a similar overall phase profile as the grayscale mask, has several differences. The most notable of these differences is the asymmetry in the profile; this is caused by the probabilistic nature of the mask, and the finite number of pixels used to represent each region. Since the set of random numbers used to represent the left side of the Fresnel lens for instance is likely to be different than the set used to represent the right side, symmetry cannot be perfectly maintained. Also, in addition to the increased roughness of the profile the probabilistic mask cannot represent the smaller zones

very well. This is to be expected as the pixilation of the phase profile inherently limits the sampling of the smaller zones, making them more difficult to represent. In order to properly sample smaller zones the pixel size would have to be reduced to subwavelength dimensions, effectively making the mask a grayscale amplitude mask.

The energy distribution in the focal plane of the lens is also noticeably different than in the ideal case, as seen in Fig. 3.12b. The central lobe is shifted away from the optical axis and the side lobes are also asymmetrical; this is due to the asymmetry in the phase profile. The central lobe is wider than the lobe produced by a grayscale mask and also contains less energy. Part of the energy that was originally in the central lobe is distributed among the side lobes, as the transition regions between the zones are larger. Part of the incident energy however is simply not focused at all because of the poor representation of the smaller zones. As a result the focusing efficiency of the probabilistic Fresnel lenses is lower than the efficiency of a grayscale lens. How much the focusing efficiency will decrease will depend on the probabilistic mask in question, since different probabilistic masks will have different profiles. To design an optimal Fresnel lens probabilistic mask, multiple masks should be simulated until the focusing efficiency is within an acceptable tolerance from the grayscale mask focusing efficiency. Note however that for short focal length Fresnel lenses no probabilistic mask can have a focusing efficiency within at least 1% of a grayscale mask. This is because for short focal length lenses the incident beam will be transmitted through several Fresnel zones, and as shown in Fig. 3.12a only the first two or three zones can be reasonably produced. Therefore when selecting a focusing efficiency tolerance this should be taken into account.

To verify these simulations 100, 200, and 500 mm focal length probabilistic Fresnel lenses were produced using the same techniques as for the probabilistic spiral phase mask.

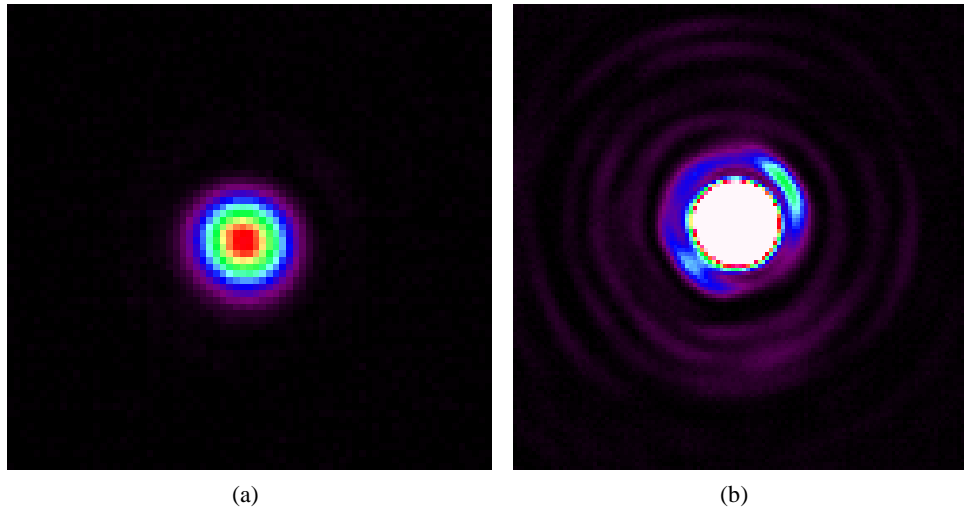


Figure 3.13: (a) Energy distribution in the focal plane of a 200 mm focal length probabilistic Fresnel lens, showing a nearly Gaussian central spot. (b) When the intensity is increased the low energy diffraction rings become visible.

Using a 1 mm beam centered on the lenses a central spot surrounded by low energy rings was observed, as shown in Fig. 3.13. The central spot is close to Gaussian, with some energy contained in low energy wings. This energy is fairly small however so the Fresnel lenses do not significantly distort the central spot. The focusing efficiency of each lens was determined by blocking the side rings with a diaphragm and then reducing the incident power so that any rings that were not blocked would have an intensity low enough to put them in the noise floor. The power in the main spot was then measured and compared to the power in the beam immediately after passing through the sample.

The focusing efficiencies, listed in Table 3.2, are in excellent agreement with the simulations. As with the grayscale amplitude mask, in order to achieve greater than 90% focusing efficiency it is necessary to have a focal length of at least 200 mm for a 1 mm incident beam and longer focal lengths for larger beams in order to minimize the number of zones in the lens.

Table 3.2: Focusing efficiency of probabilistic Fresnel lenses for various focal lengths.

$f$ , mm	$\eta_{theoretical}$ (%)	$\eta_{experimental} \pm 1\%$
50	57.2	-
100	77.9	76.2
200	91.3	92.5
300	96.3	-
500	98.0	94.7

The difference between the focusing efficiency of a VPM recorded by a probabilistic mask and the efficiency recorded by a grayscale mask is quite large for the 50 mm and 100 mm lens, but within a couple of percent for the lenses with focal lengths of 200 mm or larger. As the focusing efficiency is only 90% or more for these longer focal lengths it can be concluded that for any Fresnel lens that would be useful there is no appreciable difference between the VPMs produced by probabilistic masks and VPMs produced by grayscale masks. Therefore, even though a Fresnel lens-type phase profile may not be generated with high fidelity in a VPM, it may still be produced using a probabilistic amplitude mask with a quality comparable to the ideal grayscale amplitude mask.

### 3.4 Summary

Probabilistic amplitude masks may be used to produce volume phase masks with similar phase profiles as ideal amplitude masks. Due to diffraction during the recording of a volume phase mask these masks cannot generate phase profiles with sharp edges but if there is only a single transition region, as is the case for a spiral phase mask, then only about 3% of the energy will be lost due to a poor representation of the boundary. If the number of transition regions increase however then more energy will be lost, as seen in the case of a Fresnel lens in which over 40% of the energy can be lost for lenses containing a large number of zones. Therefore



probabilistic VPMs should be used to produce phase structures having very few sharp transitions. If this is done then the probabilistic mask will produce a good representation of the desired phase profile and it can then be used with comparable efficiency as a traditional phase mask.

## CHAPTER 4: ABERRATIONS AND CORRECTING METHODS

*Note: This chapter contains material which will be published in the following works:*

*M. SeGall, D. Ott, I. Divliansky, and L. B. Glebov, "The effect of aberrations in a holographic system on reflecting volume Bragg gratings," (submitted to Applied Optics Aug. 2013)*

*M. SeGall, I. Divliansky, D. Ott, J. Lumeau, S. Mokhov, B. Zeldovich, and L. B. Glebov, "Beam shaping by volume phase structures in photo-thermo-refractive glass," Optics+Photonics 8843-6 (2013) (conference proceedings to be published)*

Aberrations in optical systems result in poor imaging [79,80], distorted interference patterns [81-83], and an increase in the divergence of Gaussian beams [84,85]. Monochromatic aberrations are caused by the deviation of the wavefront from the ideal case, which is generally either a plane wave or an ideal Gaussian profile. As the distortions are present in the wavefront rather than in the amplitude of a beam they may be treated as local phase variations, or in other words, as a phase mask containing the aberration information which is added to the ideal profile. The key to eliminating these aberrations from the system is therefore to add a phase mask which contains the opposite amount of aberration so that the total phase variation from a given reference wavefront is zero. Here the monochromatic aberrations of an arbitrary optical system are described and how their presence in a two-beam holographic system results in locally altered fringe patterns. These distorted fringe patterns prevent a probe beam from fully satisfying the Bragg condition everywhere, resulting in a degraded spectral response of reflecting Bragg gratings. Finally, volume phase masks which can selectively adjust these aberrations are shown.

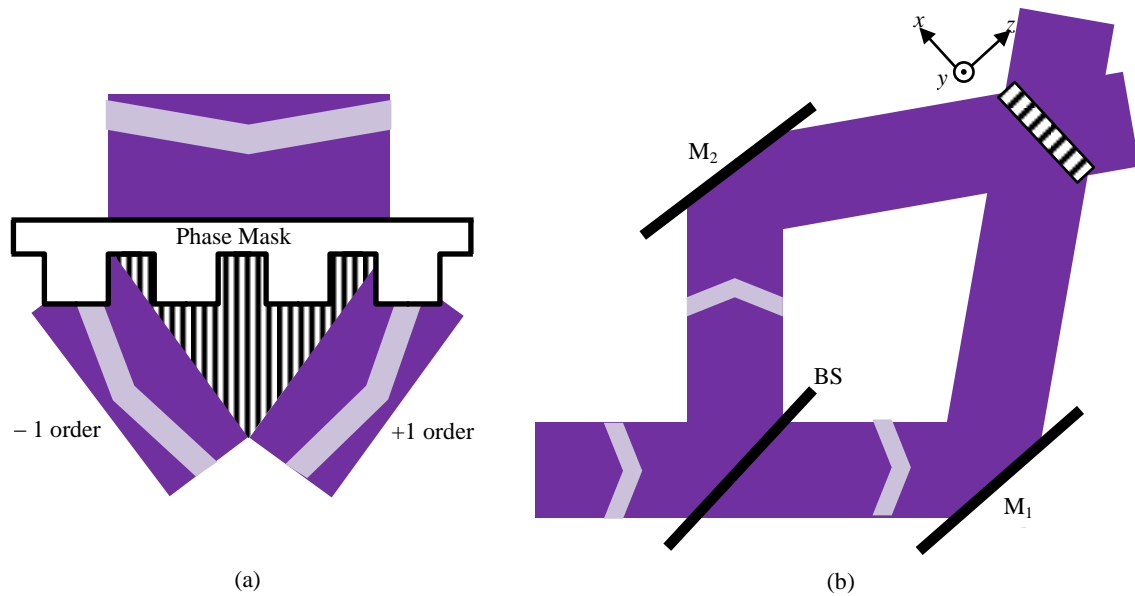


Figure 4.1: Interference profile created by (a) the diffracted orders of a phase mask and (b) the interference of two beams in a holographic system.

#### 4.1 Bragg Gratings Recorded in a Two-Beam Interference System

Volume Bragg gratings are generally recorded in one of two ways: the first way, shown in Fig. 4.1a, is to place a periodic phase mask (usually produced lithographically) in the path of the illuminating beam and let the diffracted orders interfere to produce a refractive index pattern. This technique is commonly used to produce fiber Bragg gratings and is very robust, as the interference pattern produced by the diffracted orders is easily recreated regardless of the number of gratings that need to be recorded. Furthermore, by proper design of the phase mask it is possible to have highly complex interference patterns, allowing for complex grating structures to be written. However, once a phase mask is produced it can only create a single grating profile; in short it is not very versatile because for every new grating profile that is desired a new phase mask must be produced to create that profile.

Holographic recording by two beam interference, however, is much more versatile. As shown in Fig. 4.1b, the period and tilt of the gratings can be controlled by rotating the mirrors

and the recording sample, allowing almost any grating period and tilt to be recorded in the sample provided there is enough room to allow the beams to propagate to the plane of interference. More complex grating structures may also be created by placing elements in one or both of the recording arms to alter the wavefront of the recording beam. For now however only the case where an ideal uniform grating is desired will be considered. The interference of two ideal flat-top beams with wavevectors  $\vec{k}_1$  and  $\vec{k}_2$  is described by the well-known equation [86]

$$I(x, y, z) = I_1(x, y, z) + I_2(x, y, z) + 2\sqrt{I_1 I_2} \cos\left(\left(\vec{k}_1(x, y, z) - \vec{k}_2(x, y, z)\right) \cdot \vec{r}\right), \quad (4.1)$$

where  $I$  is the intensity and  $k$  is the wavenumber in the medium. In a lossless, dielectric, photorefractive medium this will induce a refractive index profile of

$$n(x, y, z) = n_0 + \delta n \cos(\vec{K} \cdot \vec{r} + \varphi), \quad (4.2)$$

Where  $n_0$  is the background index,  $\delta n$  is the refractive index modulation,  $\vec{K} = \vec{k}_1 - \vec{k}_2$  is the grating wavevector, and  $\varphi$  is a phase term which in the ideal case is a constant which shifts the positions of the fringes.

As mentioned in Chapter 2, energy and momentum conservation requires that Bragg gratings have little to no diffraction except at the Bragg condition, which for a general one-dimensional grating is [44]

$$\cos(\phi - \theta_p) = \frac{K}{2k}. \quad (4.3)$$

Here  $\phi$  is the grating tilt, given by  $\tan \phi = K_x / K_z$  and  $\theta_p$  is the incident angle of the probe beam in the grating medium, as shown in Fig. 4.2.

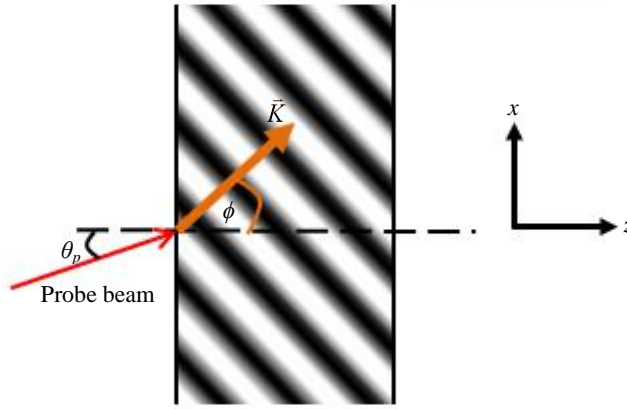


Figure 4.2: Schematic of a one-dimensional volume Bragg grating. Note that all angles shown are angles in the medium.

At or near the Bragg angle there only two waves present in the grating as the probe beam propagates (the transmitted or 0<sup>th</sup> order wave, and the diffracted wave), with the total electric field satisfying the scalar Helmholtz equation

$$\nabla^2 E + k_0^2 n^2 E = 0. \quad (4.4)$$

The general solution to this equation is [44]

$$E = A(x, y, z)e^{-i\vec{k}_p \cdot \vec{r}} + B(x, y, z)e^{-i\vec{\sigma} \cdot \vec{r}}, \quad (4.5)$$

where  $A$  is the amplitude of the transmitted wave,  $B$  is the amplitude of the diffracted wave,  $k_p$  is the wavenumber of the probe beam and  $\vec{\sigma} = \vec{k}_p - \vec{K}$ . In the ideal case the amplitudes of each wave are only a function  $z$  as energy is coupled from the transmitted wave into the diffracted wave. Inserting Eqs. 4.5 and 4.2 into Eq. 4.4 gives the coupled-wave equations which describe the transfer of energy from the transmitted wave to the diffracted wave:

$$\begin{aligned} \frac{\partial^2 A}{\partial z^2} - 2ik_{p,z} \frac{\partial A}{\partial z} &= -2\kappa k_p e^{-i\varphi} B \\ \frac{\partial^2 B}{\partial z^2} - 2i\sigma_z \frac{\partial B}{\partial z} + (k_p^2 - \sigma^2) B &= -2\kappa k_p e^{i\varphi} A \end{aligned} \quad (4.6)$$

Here  $\kappa = \pi \delta n / \lambda_0$  is the coupling coefficient for TE polarization.

Kogelnik and others [44,87] have solved these equations for both transmitting and reflecting Bragg gratings (TBGs and RBGs), and have found that TBGs have wide spectral selectivity but narrow angular selectivity while RBGs have wide angular selectivity and narrow spectral selectivity. The diffraction efficiencies of these gratings are given by (for TE polarization):

$$\eta_{TBG} = \frac{\sin^2 \left( \sqrt{S_0^2 - \Delta_B^2} \right)}{1 + \Delta_B^2 / S_0^2}, \quad (4.7)$$

$$\eta_{RBG} = \frac{\sinh^2 \left( \sqrt{S_0^2 - \Delta_B^2} \right)}{\cosh^2 \left( \sqrt{S_0^2 - \Delta_B^2} \right) - \Delta_B^2 / S_0^2}$$

where

$$S_0 = \frac{\pi \delta n t}{\lambda_B \sqrt{\cos \theta_p (\cos \theta_p - K \cos \phi / k_p)}} \quad (4.8)$$

is the strength of the grating and

$$\Delta_B = \frac{K d \sin(\phi - \theta_B)}{2 (\cos \theta_p - K \cos \phi / k_p)} \Delta \theta_p - \frac{K^2 d}{8 \pi n_0 (\cos \theta_p - K \cos \phi / k_p)} \Delta \lambda \quad (4.9)$$

is the detuning from the Bragg condition.

As shown in Fig. 4.3a, if a TBG's strength increases past  $\pi/2$  then the diffraction efficiency at the Bragg condition is reduced, while the side lobes increase. If the strength is an odd multiple of  $\pi/2$  then the peak efficiency is 100% but the peaks of the side lobes will increase for multiples larger than 1. RBGs by contrast never decrease their diffraction efficiency as their strength increases; rather, their spectral width increases, as shown in Fig. 4.3b.

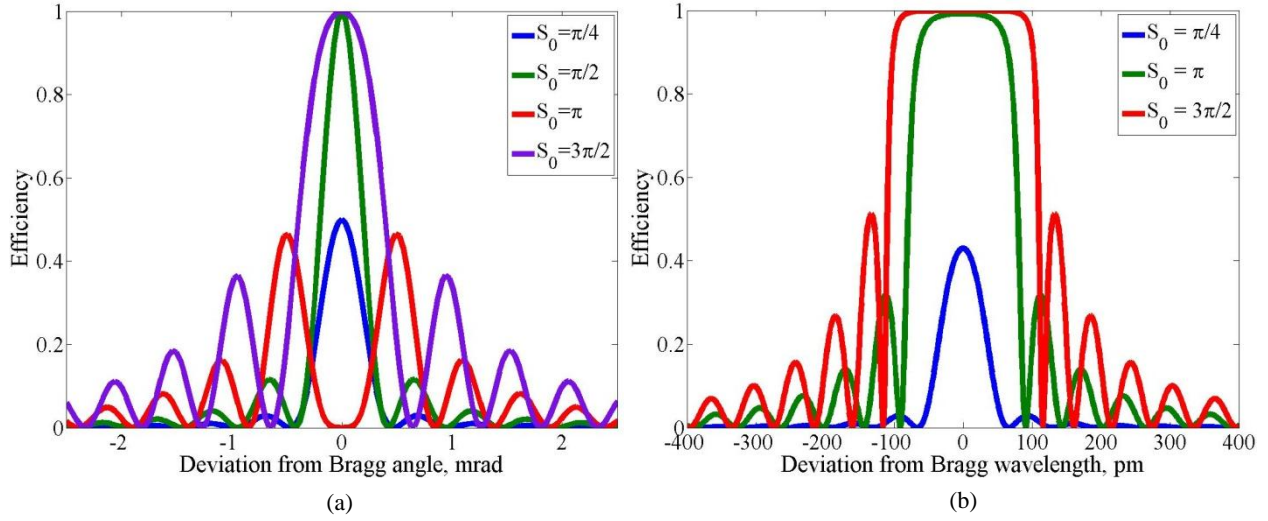


Figure 4.3: (a) Angular spectra of transmitting volume Bragg gratings of various strengths and (b) wavelength spectra of reflecting Bragg gratings.

For both TBGs and RBGs however, there are clear distinctions between the main peak and the side lobes, with the diffraction efficiency equaling zero at some point between them. This is indicative of the ideal case, when there are no variations to the grating strength or period. As will be seen however, if aberrations are present the boundary between the main lobe and the side lobes begins to disappear.

#### 4.2 Description of Aberrations

Monochromatic aberrations are described by considering the profile of the wavefront over a given aperture, which is usually circular. Originally these aberrations were characterized based on the deviation of rays from the exit pupil to the image plane compared to that of an ideal, symmetrical optical system. Because the magnitude of a given aberration cannot depend on a rotation of the coordinate axes in a symmetric optical system any wavefront description must be dependent on variables which are invariant under rotation, which limits the total wavefront description to a function of three variables:  $x$ ,  $y$ , and  $x_i$ , where  $x$  and  $y$  are the coordinates in the

object plane and  $x_i$  is a lateral coordinate in the image plane. Typically the  $x$  and  $y$  coordinates are converted to a radius  $\rho$  and angle  $\psi$ , with  $x = \rho \cos \psi$ , and  $y = \rho \sin \psi$ . Generally  $\rho$  and  $x_i$  are normalized to one at the edge of the exit pupil and maximum image position. The wavefront is then expanded in a power series [79,88]:

$$\begin{aligned}
W(\rho, \psi, x_i) &= \sum_{j,m,n} W_{jmn} x_i^{2j+m} \rho^{2n+m} \cos^m \psi \\
&= W_{200} x_i^2 + W_{111} x_i \rho \cos \psi + W_{020} \rho^2 + W_{020} \rho^4 + W_{131} x_i \rho^3 \cos \psi + \dots \\
&\quad + W_{222} x_i^2 \rho^2 \cos^2 \psi + W_{220} x_i^2 \rho^2 + W_{311} x_i^3 \rho \cos \psi + \dots
\end{aligned} \tag{4.10}$$

Here  $W_{jmn}$  is the coefficient of the corresponding aberration. This wavefront expansion gives a complete description of the wavefront at the image plane and Table 4.1 lists the aberrations and corresponding wavefront expansion terms.

It should be noted that the first three terms, while technically aberrations, are not usually considered so; piston alters the position of the wavefront along the propagation axis but does not alter the shape in any way, tilt merely changes the direction of propagation, and defocus, while altering the wavefront in one plane, can be corrected by moving the image plane along the propagation axis to the point where the wavefront is restored to its ideal shape.

Table 4.1: List of aberrations described by the power series terms of the wavefront and the relationship between the power series coefficients and Seidel coefficients [88].

Aberration	Wavefront Coefficient	Seidel Coefficient	Wavefront Form
Piston	$W_{200}$		$x_i^2$
Tilt	$W_{111}$		$x_i \rho \cos \psi$
Defocus	$W_{020}$		$\rho^2$
Spherical	$W_{040}$	$S_I = 8W_{040}$	$\rho^4$
Coma	$W_{131}$	$S_{II} = 2W_{131}$	$x_i \rho^3 \cos \psi$
Astigmatism	$W_{222}$	$S_{III} = 2W_{222}$	$x_i^2 \rho^2 \cos^2 \psi$
Field Curvature	$W_{220}$	$S_{III} + S_{IV} = 4W_{220}$	$x_i^2 \rho^2$
Distortion	$W_{311}$	$S_V = 2W_{311}$	$x_i^3 \rho \cos \psi$



Expansion terms other than the first three are the first true aberrations in that the wavefront profile is distorted and cannot be corrected by altering the image plane location or orientation. The first five of these higher order terms are known as the Seidel aberrations, which are the most common aberrations described [79,88]. The Seidel aberrations are used in a geometrical optics approach to wavefront propagation and as such they are principally concerned with finding the deviation of a light ray from the ideal optical path in a given system. These aberrations are primarily used in describing lenses and other refracting dielectric elements, and it is assumed that any higher order terms in the wavefront expansion are negligible. To calculate the Seidel aberrations in a ray-tracing scheme, first propagate a ray through the system and keep track of the deviation in angle and ray height (lateral distance from the optical axis) at each refracting surface, noting that the ray height should be normalized to the aperture of interest. The summation over all refracting surfaces, taking into account curvatures of refracting surfaces and distances of propagation for all rays in the system and comparing it to each term in the power series expansion gives the Seidel sum for each term. The Seidel sum can be written as a constant factor times the deviation of each ray from a ray propagating from an ideal reference sphere. This constant factor is the Seidel coefficient for the system.

The wavefront may also be described in a given plane by Zernike polynomials for a circular aperture or Legendre polynomials for a square aperture. For brevity, only Zernike polynomials will be covered here though identical principles are applied for Legendre polynomials. Zernike polynomials are a set of polynomials over the unit disk of the form [89,90]

$$\begin{aligned} Z_n^m &= R(\rho) \cos(m\psi) \\ Z_n^{-m} &= R(\rho) \sin(m\psi) \end{aligned} \quad (4.11)$$

where the first equation describes even functions and the second describes odd functions. The radial function  $R$  is given by

$$R_n^m(\rho) = \begin{cases} \sum_{\ell=0}^{(n-m)/2} \frac{(-1)^\ell (n-\ell)!}{\ell!((n+m)/2+\ell)!((n-m)/2+\ell)!} \rho^{n-2\ell} & n-m \text{ even} \\ 0 & n-m \text{ odd} \end{cases}. \quad (4.12)$$

The first few Zernike polynomials are listed in Table 4.2 using Noll notation [89]. The usefulness of the Zernike polynomials comes for their orthogonality on the unit disk; the integral over the unit disk of the product of two different polynomials is always zero. Because of this orthogonality it is possible to fit a wavefront to the set of polynomials and acquire a unique set of coefficients which correspond to each aberration. Furthermore, each aberration term can be investigated and modified without altering the other terms. This formulation is useful in systems which may not be rotationally symmetric, and is also useful in providing the aberrations relative to a fixed axis.

Table 4.2: List of Zernike polynomials using Noll notation. It should be noted that these polynomials give the peak-to-valley wavefront aberration (maximum deviation to minimum deviation); for RMS aberrations each polynomial will be multiplied by a unique constant [89].

Zernike Polynomial	Aberration	Cartesian Form of $Z_j$
1	Piston	1
2	Tilt $x$	$x$
3	Tilt $y$	$y$
4	Defocus	$2(x^2 + y^2) - 1$
5	$0^\circ$ Astigmatism	$(x^2 - y^2)$
6	$45^\circ$ Astigmatism	$2xy$
7	Coma $x$	$3x^3 + 3xy^2 - 2x$
8	Coma $y$	$3x^2y + 3y^3 - 2y$
9	$0^\circ$ Trefoil	$x^3 - 3xy^2$
10	$30^\circ$ Trefoil	$3x^2y - y^3$
11	Spherical	$6(x^4 + y^4 - x^2 - y^2) + 12x^2y^2 + 1$

Table 4.3: Conversion from Zernike description of aberrations to Seidel description [88]. Here  $C_j$  is the coefficient in waves of the  $j$ th Zernike polynomial in Noll notation.

Wavefront Coefficient	Aberration	Conversion Formula
$W_{111}$	Tilt	$\sqrt{(C_2 - 2C_7)^2 + (C_3 - 2C_8)^2}$
$W_{020}$	Defocus	$2C_4 - 6C_{11} \pm 2\sqrt{C_5^2 + C_6^2}$ Sign is chosen to minimize the absolute value of the magnitude
$W_{222}$	Astigmatism	$\mp 2\sqrt{C_5^2 + C_6^2}$
$W_{131}$	Coma	$3\sqrt{C_7^2 + C_8^2}$
$W_{040}$	Spherical	$6C_{11}$

Therefore rotating the system will change the values of, for instance, coma  $x$  and coma  $y$  but will not the total amount of coma, which is the square root of the product of coma  $x$  and coma  $y$ . This is the formulation used to determine the effects of aberrations on the diffraction of volume Bragg gratings.

If necessary it is possible to extract the Seidel aberrations from the Zernike terms, though this is valid if and only if the wavefront can be reasonably well described using just the Seidel aberrations; for more complicated aberration profiles it is better to remain with the Zernike terms. The peak-to-valley coefficients (the coefficients corresponding to the polynomials used in Table 4.2), shown in Table 4.3, can be easily calculated, though as discussed in [88] the peak-to-valley coefficients alone do not provide information as to the area over which an aberrated wavefront is measured. In this respect the root-mean-square (RMS) aberration description is preferable as it gives the variance of the wavefront over the entire aperture of interest. If converting to Seidel aberrations it is generally better to calculate the RMS wavefront error.

### 4.3 The Effect of Aberrations on Thick Reflecting Gratings

Reflecting Bragg gratings (RBGs) are used as elements in a variety of applications including spectral beam combining [17,91,92], mode selection in lasers [93,94], and spectral filtering [94-97]. For applications requiring narrow spectral selectivity [98], or large apertures [99], these gratings must have a uniform period throughout the length of the recording medium, which may be on the order of several millimeters. However, when recording gratings using two-beam interference it is possible during the beam resizing and shaping for aberrations to be introduced into the beam. Previous works in the literature have considered the effects of aberrations in a single recording plane where the beams perfectly overlap [81]. Such an approach is valid for thin media (on the order of tens of microns), but for thick recording media (on the order of several millimeters) there will be a significant shift in the positions of the beams relative to each other as they traverse the recording medium, as seen in Fig. 4.4.

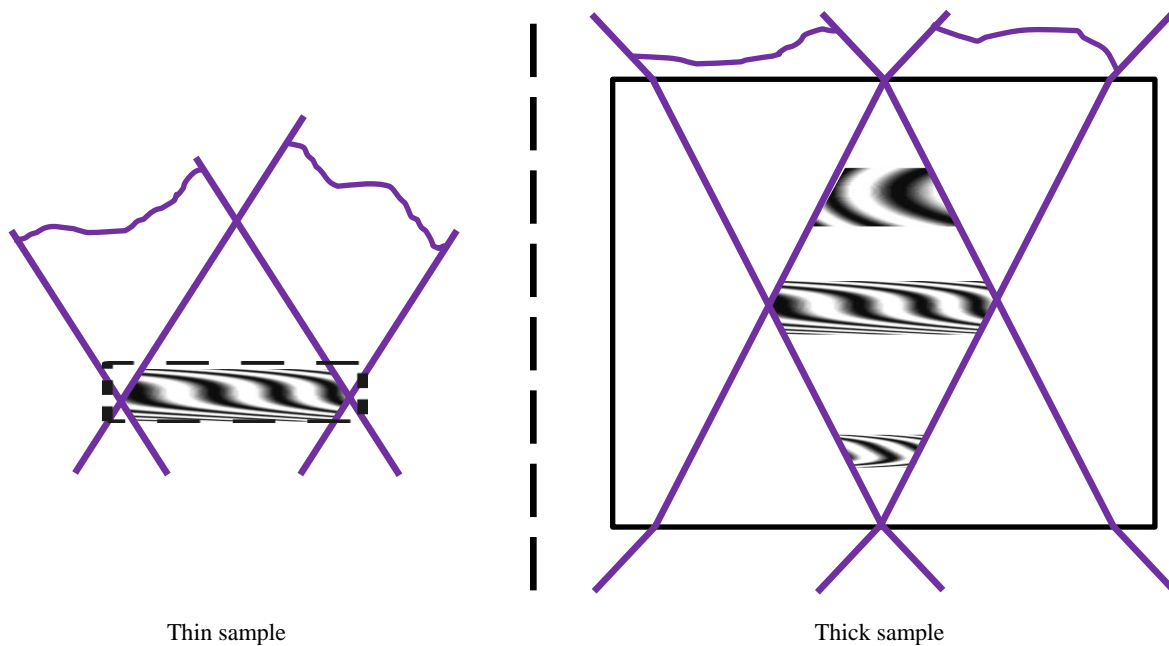


Figure 4.4: Aberrated fringe pattern recorded in (a) a thin sample (b) a thick sample. As the beams propagate in thick media different parts of the beams interfere, resulting in different fringe patterns at different depths.

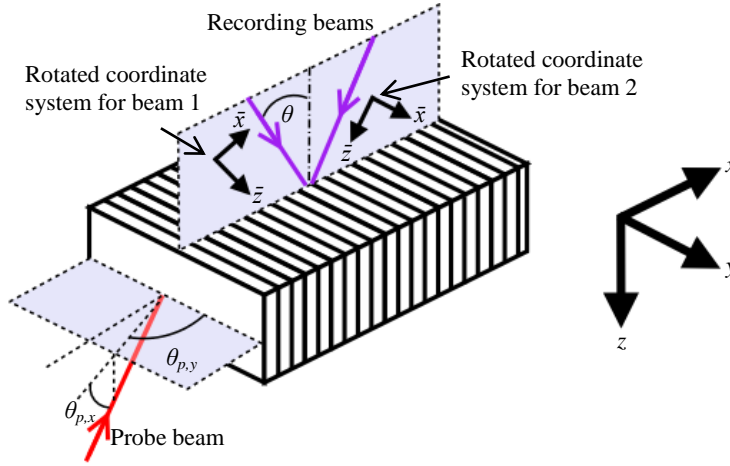


Figure 4.5: Geometry of an RGB. Two recording beams with a half angle of interference  $\theta$  inside the medium create a fringe pattern in the medium which acts as a reflecting grating for a probe beam incident along the orthogonal plane. In the presence of aberrations  $\theta$  is not a constant but has local variations based on the wavefronts of the beams. When propagating the writing beams a rotated coordinate system is used to simplify the propagation equations.

Therefore, the fringe pattern produced will not be constant throughout the grating if one or both beams have a non-uniform wavefront, but rather will have some spatial dependence.

To determine the spatial dependence of the fringe pattern, consider two interfering beams which contain aberrations, as shown in Fig. 4.5. Note that all angles shown are the angles inside the grating medium. As conventional mirrors and beamsplitters have very good surface quality it can be assumed that such an aberrated beam is produced only by the process of enlarging and shaping a beam for use in a holographic setup, which occurs prior to the beamsplitter in Fig. 4.1b. This aberrated beam then passes through the beamsplitter and is reflected towards the sample, with the interference of the beams given by Eq. 4.1. However, since there are aberrations in the beams the local wavevector  $\vec{k}$  is not constant throughout the grating as in the ideal case and must therefore be determined from the local wavefront (where it is assumed that the wavefront contains no phase discontinuities).

To calculate the wavefront at a given position within the grating, consider first a single beam in the coordinate system  $(\bar{x}, \bar{y}, \bar{z})$ , where the beam propagates along the  $\bar{z}$ -axis. It shall be

assumed that for each beam the wavefront is known at the  $\bar{z} = 0$  plane and can be described using Zernike polynomials, which as discussed previously guarantees that the wavefront is characterized by a unique, orthogonal expansion. Since the Zernike polynomials are normalized to the beam radius  $r$ , the normalized dimensions will be written as  $(\bar{x}', \bar{y}', \bar{z}') = (\bar{x}, \bar{y}, \bar{z}) / r$ . The electric field at the  $\bar{z} = 0$  plane is then

$$E(\bar{x}, \bar{y}, 0) = E_0(\bar{x}, \bar{y}, 0) \exp \left( ik \sum_j Z_j(\bar{x}', \bar{y}') \right), \quad (4.13)$$

where  $Z_j$  is the  $j$ th Zernike polynomial. The beam must then be propagated throughout the depth of the sample, which will be calculated here using the beam propagation method described in Chapter 2:

$$E(\bar{x}, \bar{y}, \bar{z}) = \mathcal{F}^{-1} \left\{ \mathcal{F} \{ E(\bar{x}, \bar{y}, 0) \} e^{\frac{-(f_x^2 + f_y^2)\bar{z}}{2k}} \right\} e^{ik\bar{z}}. \quad (4.14)$$

The local phase incursion  $\varphi$  in a given  $\bar{z}$ -plane is related to the wavefront by  $\varphi = k(\bar{z} + W)$ , so the local wavefront of a beam is given by

$$W(\bar{x}, \bar{y}, \bar{z}) = \frac{1}{k} \arctan \left( \frac{\text{Im}[E(\bar{x}, \bar{y}, \bar{z})]}{\text{Re}[E(\bar{x}, \bar{y}, \bar{z})]} \right) - \bar{z}. \quad (4.15)$$

The local wavevector is then given by the gradient of the wavefront:

$$\bar{k}(\bar{x}, \bar{y}, \bar{z}) = \frac{k}{\sqrt{1 + \left( \frac{\partial W}{\partial \bar{x}} \right)^2 + \left( \frac{\partial W}{\partial \bar{y}} \right)^2}} \begin{pmatrix} -\frac{\partial W}{\partial \bar{x}} \\ -\frac{\partial W}{\partial \bar{y}} \\ 1 \end{pmatrix}. \quad (4.16)$$

In order to calculate the wavevector in the  $(x, y, z)$  coordinate system shown in Fig. 4.5, where the normal of the grating as seen by the recording beams is along the  $z$ -axis, the wavevector must be rotated by the half angle of interference  $\theta$ . The rotated wavevector is given by the standard rotation matrix:

$$\bar{k}_g(\bar{x}, \bar{y}, \bar{z}) = \begin{pmatrix} \cos \theta & 0 & \sin \theta \\ 0 & 1 & 0 \\ -\sin \theta & 0 & \cos \theta \end{pmatrix} \bar{k}(\bar{x}, \bar{y}, \bar{z}). \quad (4.17)$$

Finally, the position of the local wavevector along the wavefront in the  $(x, y, z)$  coordinate system is given by converting the  $(\bar{x}, \bar{y}, \bar{z})$  coordinates to  $(x, y, z)$  coordinates, giving the local wavevector as  $\bar{k}_g(x \cos \theta - z \sin \theta, y, -x \sin \theta + z \cos \theta) = \bar{k}_g(\bar{x}, \bar{y}, \bar{z})$ . Note that a wavefront in the  $(\bar{x}, \bar{y}, \bar{z})$  coordinate system will not cross a given  $z$ -plane all at once. For perfect plane waves this is unimportant as the beam will maintain its profile as it propagates, so the wavevectors will be unchanged. For beams in the presence of strong aberrations (e.g. if a lens were placed in one of the recording arms and the defocus induced treated as an aberration) it is possible for the wavefront and the intensity distribution to change significantly as it propagates. In order to determine the wavevectors everywhere at a given  $z$ -plane the beams must be propagated forwards (and possibly backwards depending on the origin of the system) until every wavevector is calculated at every point in that plane. This is a computationally heavy task which is subject to accumulating numerical errors, as the beams must be propagated a given distance, the intersection of the wavefront with a  $z$ -plane determined, and then propagated again, etc.

If the beams however are close to ideal plane waves, which is the case for any reasonable amount of aberrations in a well-aligned system, then the wavefront will not change significantly as it propagates over a short distance. Calculations indicate, for instance, that a wavefront with

two waves of defocus aberration will not deviate from its original profile by more than 1 nm across a 25 mm beam after propagating 20 mm, which is thicker than any PTR sample considered here. If the wavefront does not alter its profile beyond a given tolerance throughout the depth of the sample then the wavefront at  $\bar{z} = 0$ , which is by definition described by Zernike polynomials, can be used everywhere, after propagating all parts of the wavefront onto the  $z = 0$  plane and then taking into account the lateral shift incurred as the beam propagates.

In order to propagate all parts of the wavefront to the  $z = 0$  plane note that the writing beam is effectively being treated as a plane wave with a half angle of interference  $\theta_{eff,x}$  and an inclination angle  $\theta_{eff,y}$ . Note that the inclination angle is the standard inclination angle for spherical coordinates, so an inclination angle of  $\pi/2$  corresponds to a wavevector in the  $x$ - $z$  plane. The effective angles can be determined by calculating the wavevector at the center of the beam where the only deviation from the ideal angles is caused by a tilted wavefront (which can be introduced by terms other than  $Z_2$  and  $Z_3$ , e.g. coma  $x$ ). The effective angles are therefore

$$\begin{aligned}\theta_{eff,x} &= \arctan \left( \frac{\bar{k}_{g,x}(0,0,0)}{\bar{k}_{g,z}(0,0,0)} \right) \\ \theta_{eff,y} &= \arccos \left( \frac{\bar{k}_{g,y}(0,0,0)}{k} \right)\end{aligned}\tag{4.18}$$

Here it is assumed that the wavefront center is located at  $(x,y,z) = (0,0,0)$  and  $(\bar{x}, \bar{y}, \bar{z}) = (0,0,0)$ .

The wavevector of the writing beam at the  $z = 0$  plane is then

$$\bar{k}_g(x, y, 0) = \bar{k}_g(\bar{x} / \cos \theta_{eff,x}, \bar{y} / \sin \theta_{eff,y}, 0)\tag{4.19}$$

and the wavevector at an arbitrary  $z$ -plane is

$$\bar{k}_g(x, y, z) = \bar{k}_g(x + z \tan \theta_{eff,x}, y + z \cot \theta_{eff,y}, 0).\tag{4.20}$$



The local grating vector is  $\vec{K}_{TBG}(x, y, z) = \vec{k}_{g,1}(x, y, z) - \vec{k}_{g,2}(x, y, z)$  for a probe beam incident on the same face as the recording beams (i.e. a transmitting grating). However, to use the grating as a reflecting grating the probe beam must be incident from a perpendicular plane as shown in Fig. 4.5, which requires an additional 90° rotation:

$$\vec{K}_{RBG} = \begin{pmatrix} 0 & 0 & -1 \\ 0 & 1 & 0 \\ 1 & 0 & 0 \end{pmatrix} \vec{K}_{TBG} \quad (4.21)$$

for a probe beam incident along the  $x$ -axis.

The reflection spectrum of uniform Bragg gratings may be calculated using Kogelnik's coupled-wave equations [44]. In coupled-wave theory the fields of the forward (transmitted) and backward (reflected) waves are written in matrix form as

$$\begin{pmatrix} E_+(0) \\ E_-(0) \end{pmatrix} = \mathbf{T} \begin{pmatrix} E_+(t) \\ E_-(t) \end{pmatrix}, \quad (4.22)$$

where  $E_+$  is the forward propagating wave and  $E_-$  is the backward propagating wave.  $\mathbf{T}$  is a transfer matrix with elements [100]

$$\begin{aligned} T_{11} &= [\cosh(\gamma t) + i\Delta k \sinh(\gamma t) / \gamma] \exp(ik_{Bragg}t) \\ T_{12} &= -\kappa t \sinh(\gamma t) \exp(-i(k_{Bragg}t + \varphi)) / (\gamma t) \\ T_{21} &= -\kappa t \sinh(\gamma t) \exp(i(k_{Bragg}t + \varphi)) / (\gamma t) \\ T_{22} &= [\cosh(\gamma t) - i\Delta k \sinh(\gamma t) / \gamma] \exp(-ik_{Bragg}t) \end{aligned} \quad (4.23)$$

Here  $\Delta k = k_p - k_{Bragg}$  is the difference between the propagation constant of the probe beam and the propagation constant for a wave satisfying the Bragg condition,  $\varphi$  is the grating phase factor,  $t$  is the grating thickness,  $\kappa = \pi \delta n / \lambda$  is the coupling coefficient between the forward and

backward-propagating waves (assuming TE polarization),  $\gamma^2 = \kappa^2 - (\Delta k)^2$ , and  $\delta n$  is the refractive index modulation [100].

To find  $k_{Bragg}$ , note that to satisfy the conservation of energy and momentum in the Bragg regime where only a single diffracted order can exist, the diffracted wavevector must be related to the incident wavevector by  $\vec{k}_d = \vec{k}_i - \vec{K}$ . In the general two-dimensional case the incident wavevector and grating wavevector have the form

$$\vec{k}_i = k_i \begin{pmatrix} \sin \theta_z \sin \theta_y \\ \cos \theta_y \\ \cos \theta_z \sin \theta_y \end{pmatrix}, \quad \vec{K} = K \begin{pmatrix} \sin \phi_z \sin \phi_y \\ \cos \phi_y \\ \cos \phi_z \sin \phi_y \end{pmatrix}, \quad (4.24)$$

where  $\theta_z$  and  $\phi_z$  are the angles of the incident beam and grating vectors, respectively, relative to the  $z$ -axis (where the  $z$ -axis is the axis of propagation of the probe beam, as in Fig. 4.2), and  $\theta_y$  and  $\phi_y$  are the angles of the incident beam and grating vectors, respectively, relative to the  $y$ -axis.

To satisfy the Bragg condition,  $|\vec{k}_d| = |\vec{k}_i|$ , which gives the Bragg condition as

$$K = 2k_{Bragg} \left( \sin \theta_y \sin \phi_y \cos(\phi_z - \theta_z) + \cos \theta_y \cos \phi_y \right). \quad (4.25)$$

This simplifies to Kogelnik's Bragg condition in the one-dimensional case. In the coordinate system shown in Fig. 4.5,  $\theta_z = \theta_{p,x}$ ,  $\phi_z = \arctan(K_{RBG,x} / K_{RBG,z})$  is the tilt angle along the same axis,  $\theta_y = \theta_{p,y}$ , and  $\phi_y = \arccos(K_{RBG,y} / |K_{RBG}|)$ .

As stated previously, Eqs. 4.22-4.25 assume a uniform grating. In the case of a distorted grating, the reflectance from each point can be treated as an infinitesimal grating which is uniform across the grating face (but not necessarily throughout the thickness), and the overall reflectance is the integration of the reflectance at every point:

$$R(\lambda) = \frac{\iint R(y, z, \lambda) I_p(y, z, \lambda) dy dz}{\iint I_p(y, z, \lambda) dy dz}. \quad (4.26)$$

Here  $R$  is the reflectance and  $I_p$  is the intensity of the probe beam. The reflectance at every point in turn can be calculated (assuming the slowly varying envelope approximation) by dividing the transfer matrix into  $N$  segments which are thin enough to be considered uniform throughout the thickness:

$$\mathbf{T} = \prod_{i=1}^N \mathbf{T}_i. \quad (4.27)$$

Here  $\mathbf{T}_i$  is a function of a local (constant)  $\kappa_i$ ,  $\Delta k_i$ ,  $t_i$ , and  $\varphi_i$ . In order to match the phases between the segments,  $\varphi_i$  must satisfy the relationship  $\varphi_i = \varphi_{i-1} + 2t_{i-1}\pi / \Lambda_{i-1}$  [100]. The local grating vector which should be used to calculate  $\mathbf{T}_i$  is  $\vec{K}(x, y + \Delta y, z + \Delta z)$ , where  $\Delta y = x \cot \theta_{p,y}$  and  $\Delta z = x \tan \theta_{p,x}$ . Also, the effective thickness of the grating will be  $t_{eff} = t / (\cos \theta_{p,x} \sin \theta_{p,y})$ .

The reflectance of each point is then given by [100]

$$R(y, z, \lambda) = \left| \frac{T_{21}}{T_{11}} \right|^2. \quad (4.28)$$

Inserting Eq. 4.28 into Eq. 4.26 provides to overall reflectance spectrum for a probe beam incident on the grating.

For a given set of aberrations the reflection spectrum that is measured will in general depend on the parameters of the probe beam (position, size, incident angles, etc.) as well as the thickness and strength of the grating. The combination of grating and probe beam parameters yields a plurality of spectral profiles showing some degree of deterioration. To demonstrate this, two gratings representing different types of applications for lasers emitting in the vicinity of

1064 nm are simulated here. The first one is a high-efficiency, relatively thin grating (Grating A), useful in applications such as spectral beam combining, and the second one is a thick grating with moderate diffraction efficiency (Grating B), which may be used in applications requiring narrow spectral widths. Grating A is designed such that it ideally has a 1064 nm resonant wavelength with  $\delta n = 200$  ppm, and  $t = 5.5$  mm. From Eqs. 4.20-4.26 this should give a diffraction efficiency of 99.4% and a spectral width of 178 pm for a probe beam at normal incidence. Grating B is designed for the same resonant wavelength, with  $\delta n = 20$  ppm, and  $t = 20$  mm, corresponding to a diffraction efficiency of 68.5% and a spectral width of 24 pm at normal incidence. In order to minimize the effects of possible grating chirp (a best-case scenario), Grating A was analyzed over the region  $-2.75 \leq x \leq 2.75$  mm and Grating B was analyzed over the region  $-10 \leq x \leq 10$  mm. Both gratings are 25 mm wide and 6 mm deep (along the  $z$ -axis in Fig. 4.4) with a recording wavelength of 325 nm. This recording wavelength is the emission wavelength of a He-Cd laser which is typically used to record gratings in PTR glass. These gratings are then illuminated with a collimated 3 mm beam at normal incidence at two positions: the center of the grating and halfway between the center and the right side ( $y = 6.25$  mm in Fig. 4.4). Note that the center of the grating is the most likely place for any symmetry in the system to minimize the effects of aberrations since this is where the writing beams will perfectly overlap, whereas in all other positions there is no perfect overlap. Therefore it is expected that any deviations in the reflection spectra caused by aberrations will be minimized at this point.

Figs. 4.6a and 4.6b show the effects of one wave of a given aberration on the reflection spectrum for Grating A and Figs. 4.6c and 4.6d show the effects for Grating B.

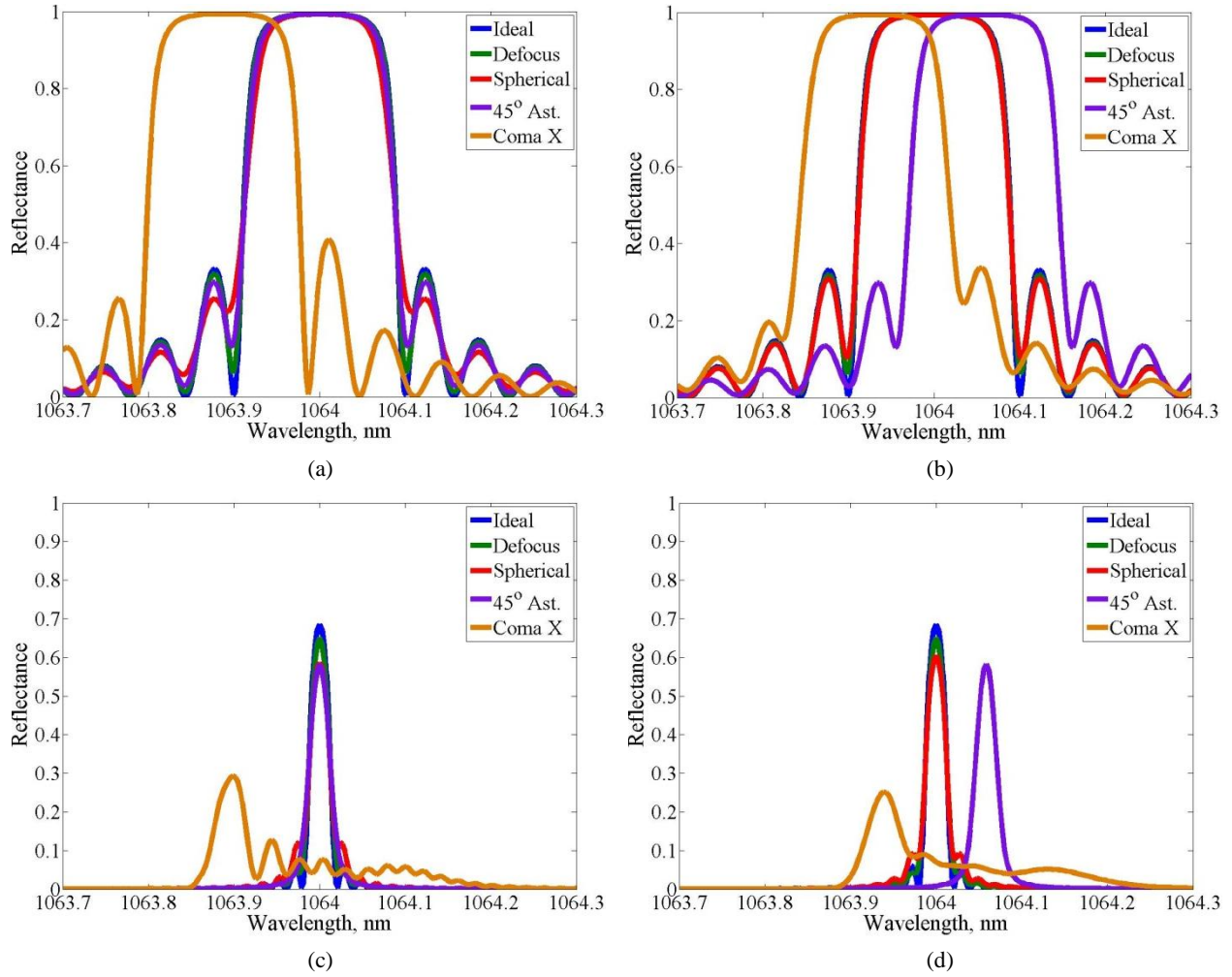


Figure 4.6: Reflection spectra in the presence of one wave of a given aberration for Grating A {(a), (b)}, and Grating B {(c), (d)}. The reflection spectra for a beam incident on the center of the grating {(a), (c)} is different than when the beam is incident at a point halfway between the center and the edge of the grating {(b), (d)}.

In both cases the side lobes are washed out and there is a shift in the central wavelength of up to 100 pm for some aberrations depending on the beam position. Grating A shows a small amount of broadening in the main peak but the peak diffraction efficiency is largely unchanged. This can be explained by the large spectral bandwidth of the initial grating. At each point along the face the reflection spectrum has a slightly different central wavelength, but since the initial bandwidth is wide these small shifts do not shift the peak outside of the main lobe or even shift them within the main lobe very much. This also applies for coma  $x$  and  $45^\circ$  astigmatism; even

though the central wavelengths have noticeably shifted for these aberrations this large shift is more or less consistent at each point along the face. Other effects however are not reduced by the large spectral acceptance; coma  $x$  for instance creates an asymmetry in the side lobes which is consistent with the asymmetrical profiles induced in chirped gratings [45]. Unlike typical chirped gratings however, where the chirp is so large that the spectral acceptance is broadened significantly, the amount of chirp induced by the single wave of coma  $x$  is insufficient to have any noticeable effect on the spectral width of the central lobe.

Grating B by contrast shows a much more dramatic change in the reflection spectra, especially for coma  $x$ . This is not surprising, as the grating is much thicker than Grating A, and it was also designed to be a weaker grating so there are no benefits that may be associated with possible overmodulation widening the spectrum as in the case of Grating A. In addition to the washed out side lobes there is a noticeable decrease in peak efficiency as well as spectral broadening. Coma  $x$  shows the most significant change, with a reduction in peak efficiency of over 40% and a spectral broadening to  $\sim 300$  pm.

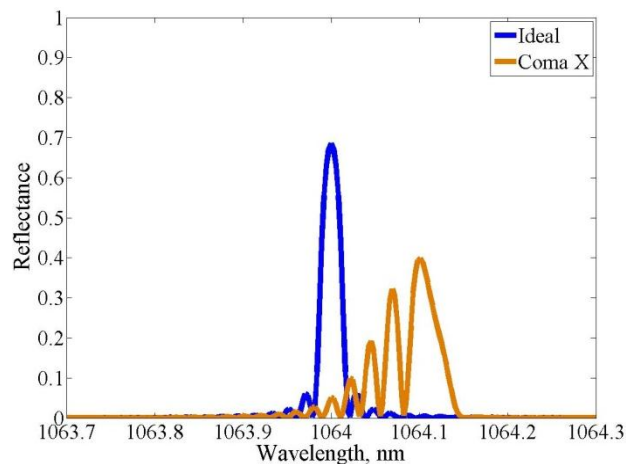


Figure 4.7: Reflection spectrum for a 3 mm beam centered on Grating B in the presence of one wave of coma  $x$  if the local tilt of the grating is ignored and only the local change in period is considered.

This is caused partially by the change in local grating tilt and partially by the change in local period, as seen in Fig. 4.7 where the tilt of the grating is ignored. A comparison of Fig. 4.7 to Fig. 4.6c shows that both effects have a significant contribution to the final spectrum neither can be ignored in favor of the other.

The degradation of the reflection spectra in the presence of even one wave of aberrations and their associated problems when used in wider applications requires that aberrations be dealt with during the recording of the grating. Unlike fibers or thin film gratings it will not be sufficient to find a plane where the aberrations are minimized as the large thickness of the recording medium will ensure that the beams produce a spatially dependent fringe profile in the recording medium. If these aberrations cannot be corrected by proper alignment of the holographic recording system then an aberration correcting element will be necessary to eliminate them.

#### 4.4 Aberration Correcting Elements

Aberration correcting elements (ACEs) may be used to eliminate specific aberrations from an optical system. If the aberrations in the system are fixed and known, it is possible to manufacture a passive phase mask which corrects them [101,102]. If the aberrations fluctuate however, it will be necessary to have active monitoring of the aberrations as well as a real-time corrector, such as a spatial light modulator or deformable mirror [103-108]. ACEs, both passive and active, generally rely on characterizing the aberrations using Zernike polynomials as described previously, and then create an element which has the same magnitude of aberration but opposite sign.

In industrial applications the ACE is generally produced with liquid crystal devices or thin films which are no more than a few tens of microns thick, so placing the ACE in the system will not have a significant effect on the aberrations in the system aside from the corrections introduced. However, as mentioned previously these elements cannot be used in high power systems and so a thicker phase element must be used. As discussed in Chapter 2 a thick phase mask allows the beam to propagate while accumulating the local phase. This can be problematic in that aberrations can change if they pass through a thick plate. To observe this phenomenon consider just the Seidel aberrations. If a beam is not collimated but rather converges, with a given ray converging at an angle  $\theta_c$ , then the Seidel coefficients become [79]

$$S_I = -\frac{n^2-1}{n^3}\theta_c^4 t \quad S_{II} = \frac{\bar{\theta}_c}{\theta_c} S_I \quad S_{III} = \left(\frac{\bar{\theta}_c}{\theta_c}\right)^2 S_I \quad S_{IV} = 0 \quad S_V = \left(\frac{\bar{\theta}_c}{\theta_c}\right)^3 S_I, \quad (4.29)$$

where  $\bar{\theta}_c$  is the convergence angle of the principal ray. Thus the thicker the mask used to correct aberrations, the more likely that the aberrations that need to be corrected will change once the mask has been placed in the system. Unfortunately even if the Seidel aberrations are all that need to be corrected Eq. 4.29 cannot be used to convert the changed profiles into their respective Zernike polynomials due to the lack of uniqueness in the power series description of the wavefront. Furthermore, in high power systems any heating of the phase mask may induce thermal lensing, further altering the phase profile that needs to be corrected. Generally, to measure the aberrations appropriately a PTR blank must be inserted into the system and the system run until a steady state is reached. The aberrations can then be measured and the correcting phase profile determined. Once this is done the phase mask will properly correct the aberrations in the system regardless of the thickness of the sample used.



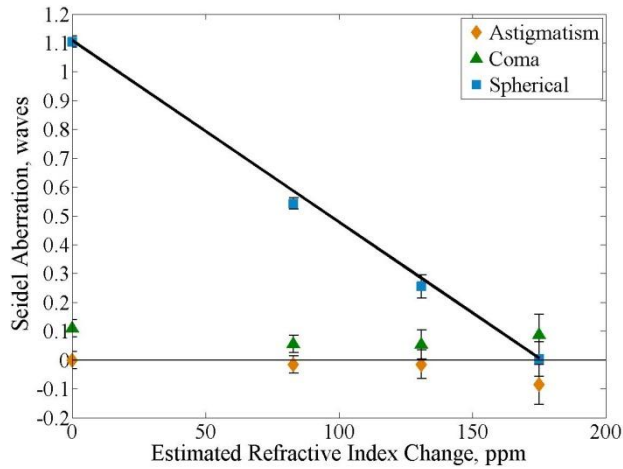


Figure 4.8: The spherical aberration in a system is corrected using a PTR aberration-correcting element without altering the other aberrations in the system.

To demonstrate selectively aberration-correcting elements, two VPMs were recorded: a mask to correct only spherical aberration and a mask which corrects multiple aberrations having different magnitudes. To produce a spherical-correcting mask a 200 mm plano-convex lens was placed in a double-pass interferometer (Zygo) and deliberately misaligned to produce aberrations other than spherical. The aberrations were then measured using commercially available interferogram analysis software (Metropro). A mask was then manufactured to produce the opposite amount of spherical aberration while not altering any of the other aberrations. To monitor the correction of the phase mask the thermal development was broken into several steps. The first step was the standard nucleation described in Chapter 1 but the crystallization phase was only allowed to proceed for approximately 10 minutes. The partially developed sample was placed in the interferometer and the aberrations measured. This was repeated several times until the desired correction was achieved. As shown in Fig. 4.8, over the course of four developments the spherical aberration was reduced in a nearly linear fashion until it was completely eliminated while coma and astigmatism were unchanged (the values shown are the Seidel values for simplicity). The last step shows a slight change in the values for coma and astigmatism; this is

due to increased scattering in the sample caused by repeated thermal developments which makes it difficult for the analysis software to accurately determine the fringe positions in the interferometer. Also note that the refractive index change here is the estimated change rather than the measured value. This is because the phase profile covered the entire sample area with no additional room to record a stripe that could be measured in the shearing interferometer discussed in Chapter 2. The refractive index change was therefore estimated by comparing the thermal development times and temperatures to other samples for which the refractive index change had been measured.

The second aberration-correcting mask was designed to correct different quantities of spherical, coma  $x$ , and coma  $y$  aberrations while not altering astigmatism. Because multiple aberrations must be simultaneously corrected a very specific phase profile must be created in the phase mask. This makes the system very sensitive to alignment, with deviations of even a millimeter being sufficient to produce a completely different characterization of the aberrations. As with the spherical-only ACE the change in the aberration coefficients were measured over several steps, requiring several days to redevelop and re-measure the sample. This increases the odds of misalignment occurring so to minimize this problem the ACE was placed in the Zygo interferometer without any additional beam-distorting elements for characterization. In this configuration the ACE acts as the aberration-inducing element, with the amount of aberration induced being equal to the amount of aberration that would be corrected if this element were placed in the appropriate system.

As seen in Fig. 4.9, the ACE induces (corrects) different amounts of spherical, coma  $x$ , and coma  $y$  while not altering either  $0^\circ$  astigmatism or  $45^\circ$  astigmatism.

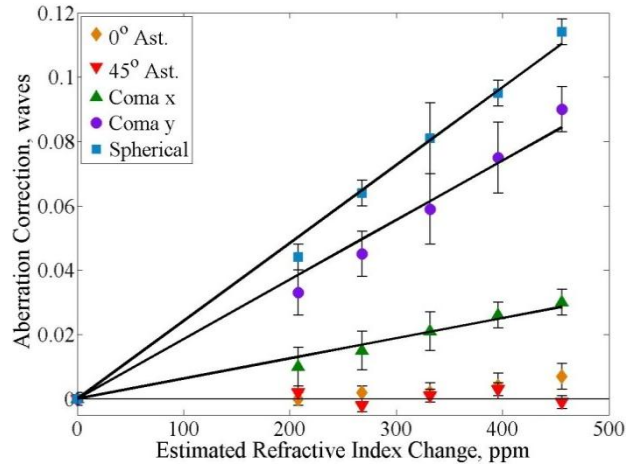


Figure 4.9: Aberration correction for varying amounts of spherical, coma x, and coma y along with linear fits. Astigmatism is not altered by the ACE. Here the aberration correction is given as the Zernike coefficient in waves rather than the Seidel values because the Seidel aberrations, which lack uniqueness, cannot distinguish the components of a given aberration along each axis.

As with the previous ACE, the corrections increase nearly linearly, and the astigmatism increases slightly during the last steps due to the increased scattering caused by the repeated redevelopments of the sample. Note that the third point on the spherical curve and the third and fourth points on the coma y curve have larger error bars than the other points. This is because the sample was misaligned along the y axis (where the y axis is defined as in Fig. 2.2) by approximately 1 mm during the third step, which was not noticed until later. Therefore the data for spherical and coma y during this step is based not on direct measurements but on a comparison of the times that the sample was developed for the third step as compared to the other step. While 45° astigmatism may also have been affected during this step the absolute value of the aberration was so small that any deviation from the expected value due to misalignment is within the uncertainty of measurements. During the fourth step this vertical misalignment was partially corrected, which was sufficient to measure the spherical aberration directly. However, coma y was observed to be more sensitive to misalignment, so the partial

correction was insufficient to provide reasonable data for this point. Therefore the coma  $y$  data was also inferred from the development time at this point.

#### 4.5 Summary

Aberrations in a holographic system can have a significant impact on the performance of a grating, washing out side lobes, decreasing peak efficiency, shifting the resonant wavelength, inducing spectral broadening, etc. While in systems where the recording medium is very thin this problem can be minimized by proper placement of the sample, for thick samples this cannot be achieved because the beams will propagate over several millimeters while recording the grating pattern. To avoid this problem it may be necessary to place an aberration-correcting element into the system. Such masks can be fabricated in PTR glass using the techniques described previously, which allow the selective correction of any aberration that can be properly characterized.

## CHAPTER 5: HOLOGRAPHIC PHASE MASKS

*Note: This chapter contains material which will be published in the following work:*

*M. SeGall, I. Divliansky, and L. B. Glebov, "Simultaneous laser mode conversion and beam combining using multiplexed volume phase elements," Advanced Solid-State Lasers Congress AW2A.9 (2013) (conference proceedings to be published).*

In the previous chapters the applications of volume phase masks have been described where a specific mask is placed in a system to produce the desired beam profile. For closed systems which are not intended to be significantly modified this is all that is required. However, if the system is intended to have multiple configurations and/or outputs, it is necessary to have multiple masks with each mask designed to the needs of the current system requirements. While multiple masks can be designed and then swapped in as needed, this is an inefficient method, requiring realignment and potentially requiring the same material properties such as physical thickness and losses. A more efficient method is to multiplex the phase masks in a single substrate. This can be achieved by creating a transmission hologram which contains the same phase information as the phase mask and utilizing the established techniques of multiplexing volume Bragg gratings [109-112] to multiplex each holographic phase mask.

### 5.1 Recording Complex Phase Structures in Photosensitive Media

Recording complex holograms is a fairly simple modification of the system described in Chapter 4 to produce regular VBGs. As shown in Fig. 5.1, all that is required is to place an element in one of the arms of the two-beam recording system used to create gratings.

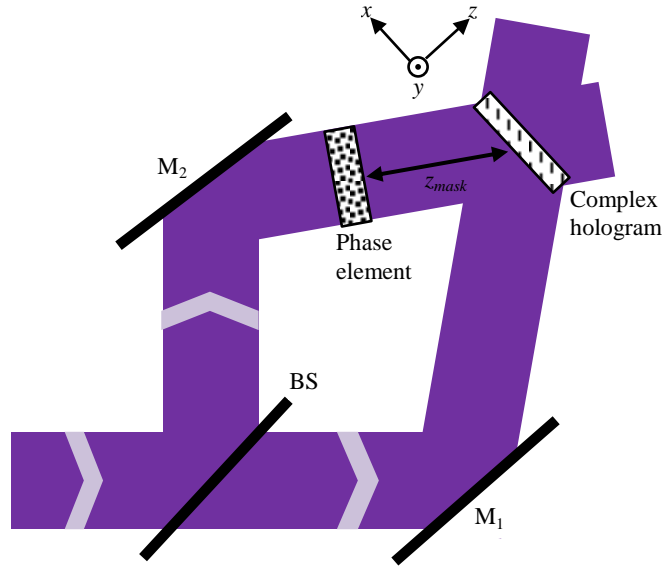


Figure 5.1: A phase element in one arm of the two-beam interference system creates an object beam which, when interfered with the reference beam, produces a complex hologram.

Any object can be placed in the arm, including phase-only elements and amplitude-only elements, though in the case of amplitude-only elements it is necessary to modify the system slightly to allow the reflected light from the object to interfere with the reference beam at the position of the sample. Here only transmitting phase elements will be considered, as it is this phase profile that is to be encoded in a hologram.

Because the phase profile is known, and its distance from the sample also known, it is possible to use the same techniques described in Chapter 4 when considering aberrated recording beams to determine the hologram profile as the phase element can be considered to have induced aberrations in the sample. If the phase mask is located a distance  $z_{mask}$  from the front surface of the recording sample then the electric field at the surface of the sample (before propagating into the sample) is simply the Fresnel diffraction pattern of the phase mask at that distance [43]:

$$E(x, y, z_{mask}) = \frac{e^{ik_0 z}}{i\lambda_0 z} \int_{-\infty}^{\infty} \int_{-\infty}^{\infty} E(x_0, y_0, 0) \exp\left(\frac{ik_0}{2z_{mask}} \left[(x-x_0)^2 + (y-y_0)^2\right]\right) dx_0 dy_0. \quad (5.1)$$

At the air/sample boundary Snell's law and Fresnel reflections must be taken into account, which must be applied locally for each wavevector. Note that if the phase mask used induces a high amount of divergence there may be a significant variation in the amplitude of the field that is transmitted into the sample due to the large variation in Fresnel reflection coefficients. Once the beam has passed the air/sample boundary the interference pattern produced can be calculated using Eqs. 4.14-4.17 to find the local wavevectors in the medium.

Once the hologram has been recorded the phase profile can be extracted by illuminating the beam with the reference wave; the diffracted beam will have the same phase profile as the recording beam. If the wavelength of the reconstructed beam is changed however, it is not possible in general to perfectly reconstruct the desired phase profile without altering the properties of the reconstruction beam in some way [113]. For thick holograms this can be treated as a deviation from the Bragg condition; even for a traditional Bragg grating if the reconstruction wavelength is changed the angle of incidence must also be changed in order to satisfy the Bragg condition. For complex holograms however the constantly changing fringe pattern results in a constantly changing Bragg condition which generally cannot be simultaneously matched by any wavelength other than the recording wavelength, resulting in a degradation of the phase profile in the diffracted beam.

There are exceptions to this however: if for instance the phase profile of the phase mask consists of very low spatial frequencies except at regions of any sharp phase transition (e.g. a binary phase mask) then the fringes of the hologram will have effectively the same grating vector as a grating recorded without the mask present, but contain local phase jumps. This can be seen by considering a plane wave which obtains a phase distribution  $\varphi(\bar{x}, \bar{y})$  after passing through the

phase mask (following the notation used in Chapter 4, where the bars indicate the coordinate system where the beam travels along the  $\bar{z}$  axis). From Eqs. 4.14-4.16 the wavevector will be

$$\bar{k}_g = \frac{k}{\sqrt{k^2 + \left(\frac{\partial \varphi}{\partial \bar{x}}\right)^2 + \left(\frac{\partial \varphi}{\partial \bar{y}}\right)^2}} \begin{pmatrix} -\frac{\partial \varphi}{\partial \bar{x}} \cos \theta + k \sin \theta \\ -\frac{\partial \varphi}{\partial \bar{y}} \\ \frac{\partial \varphi}{\partial \bar{x}} \sin \theta + k \cos \theta \end{pmatrix}. \quad (5.2)$$

If the partial derivatives of  $\varphi$  are small (except at any phase jumps) then the normalization factor is approximately one and the wavefront reduces to the wavefront for a plane wave, similar to a standard plane wave in the absence of any phase mask. Because the grating vector is not altered the hologram will act similar to a Bragg grating, where by proper adjustment of the incident angle one may use any wavelength for the probe beam without degrading the phase information or diffraction efficiency. However, because the phase of the grating is not constant, and as shown in Eq. 4.6 the phase of the diffracted beam depends on the phase difference between the object and reference beam it is therefore possible to encode the phase mask information into the grating. It is this case, where the phase mask profile in the object beam is a binary profile, that will be considered here.

## 5.2 Coupled Wave Equations for Phase Shifted Transmitting Bragg Gratings

To determine the diffraction characteristics of a grating when a binary phase mask has been introduced into a recording arm, consider again the two beam interference equation (Eq. 4.1). With the phase mask in one arm it becomes

$$I(x, y, z) = I_1 + I_2 + 2\sqrt{I_1 I_2} \cos\left(\left(\bar{k}_1 - \bar{k}_2\right) \cdot \bar{r} + \varphi(x \cos \theta - z \sin \theta, y, z \cos \theta - x \sin \theta)\right), \quad (5.3)$$



where  $\varphi(\bar{x}, \bar{y})$  has been rotated into the grating centered coordinates. As a further simplifying assumption it shall be assumed that  $\theta$  and  $z$  are both small so that  $\varphi(\bar{x}, \bar{y}) \approx \varphi(x, y)$ . The refractive index profile is then  $n(x, y, z) = n_0 + \delta n \cos(\bar{K} \cdot \bar{r} + \varphi(x, y))$ . Note that in Chapter 4 it was assumed that there were no phase discontinuities and so the piston term in the wavefront expansion was a constant which could without loss of generality be set to zero (after calculating the local grating wavevector). Here however phase discontinuities must be considered. The coupled wave equations for a probe beam incident on this phase-shifted grating are again calculated using the scalar Helmholtz wave equation (Eq. 4.4) with the general solution of Eq. 4.5. However, because  $\varphi$  is not constant it cannot be assumed that the amplitudes  $A$  and  $B$  of the transmitted and diffracted waves are only functions of  $z$ . The coupled wave equations therefore become

$$\begin{aligned} \frac{\partial^2 A}{\partial x^2} + \frac{\partial^2 A}{\partial y^2} + \frac{\partial^2 A}{\partial z^2} - 2i \left( k_{p,x} \frac{\partial A}{\partial x} + k_{p,y} \frac{\partial A}{\partial y} + k_{p,z} \frac{\partial A}{\partial z} \right) &= -2\kappa k_p e^{-i\varphi(x,y)} B \\ \frac{\partial^2 B}{\partial x^2} + \frac{\partial^2 B}{\partial y^2} + \frac{\partial^2 B}{\partial z^2} - 2i \left( \sigma_x \frac{\partial B}{\partial x} + \sigma_y \frac{\partial B}{\partial y} + \sigma_z \frac{\partial B}{\partial z} \right) + (k_p^2 - \sigma^2) B &= -2\kappa k_p e^{i\varphi(x,y)} A \end{aligned} \quad , \quad (5.4)$$

where again  $k_p$  is the wavenumber of the probe beam and  $\vec{\sigma} = \vec{k}_p - \vec{K}$ .

These coupled-wave equations cannot be solved analytically in the general case. This can be seen by considering Fig. 5.2, where there is a phase discontinuity parallel to the fringes. As the probe beam propagates through the grating, part of the beam may propagate the entire length of the grating without ever encountering the discontinuity in the grating phase. In this case the beam will diffract in the same manner as a regular Bragg grating. The only difference will be the local phase incurred by the diffracted beam.

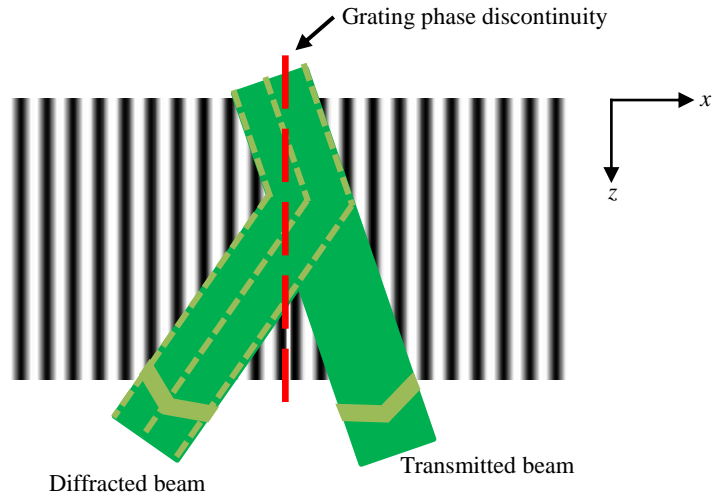


Figure 5.2: Diffraction in the presence of a discontinuity in the grating phase. Different parts of the transmitted and diffracted beams may see the phase discontinuity as the beams propagate throughout the grating.

For instance, the leftmost and rightmost transmitted rays in Fig. 5.2 do not encounter the phase discontinuity so both will diffract normally. However, because the grating phase is different for each ray when they diffract, the diffracted rays will have different phases. In contrast, the centermost ray of the probe beam passes through the phase discontinuity and then diffracts, with the diffracted ray also passing through the discontinuity. For sufficiently thick gratings it is also possible for part of the probe beam to pass through the discontinuity and then diffract but the diffracted ray does not pass through the discontinuity. Because different parts of the transmitted and diffracted beams are subject to different conditions the resulting diffraction profile must be calculated numerically.

To numerically calculate the profiles of the transmitted and diffracted waves it will be assumed that the second derivatives are negligible as before (though the following method can be easily modified to include them if necessary). For simplicity consider the case where the probe beam satisfies the Bragg condition, as this is the condition that is of most interest. Eq. 5.4 then becomes

$$\begin{aligned}
\frac{1}{k_p} \left( k_{p,x} \frac{\partial A}{\partial x} + k_{p,y} \frac{\partial A}{\partial y} + k_{p,z} \frac{\partial A}{\partial z} \right) &= -i\kappa e^{-i\varphi(x,y)} B \\
\frac{1}{k_p} \left( \sigma_x \frac{\partial B}{\partial x} + \sigma_y \frac{\partial B}{\partial y} + \sigma_z \frac{\partial B}{\partial z} \right) &= -i\kappa e^{i\varphi(x,y)} A
\end{aligned} \tag{5.5}$$

To solve these equations they will first be converted to Fourier space along the transverse dimensions and then converted back to coordinate space. Defining the Fourier transform as

$$\begin{aligned}
\mathcal{F}\{f(x, y)\} &= \int_{-\infty}^{\infty} f(x, y) e^{-2\pi i(xf_x + yf_y)} dx dy \\
\mathcal{F}^{-1}\{\tilde{f}(f_x, f_y)\} &= \int_{-\infty}^{\infty} \tilde{f}(f_x, f_y) e^{2\pi i(xf_x + yf_y)} df_x df_y
\end{aligned} \tag{5.6}$$

the coupled wave equations become

$$\begin{aligned}
\frac{2\pi i}{k_p} \tilde{A}(f_x k_{p,x} + f_y k_{p,y}) + \frac{k_{p,z}}{k_p} \frac{\partial \tilde{A}}{\partial z} &= \mathcal{F}\{-i\kappa e^{-i\varphi(x,y)} B(x, y, z)\} \\
\frac{2\pi i}{k_p} \tilde{B}(f_x \sigma_x + f_y \sigma_y) + \frac{\sigma_z}{k_p} \frac{\partial \tilde{B}}{\partial z} &= \mathcal{F}\{-i\kappa e^{i\varphi(x,y)} A(x, y, z)\}
\end{aligned} \tag{5.7}$$

where  $\tilde{A}(f_x, f_y, z)$  is the Fourier transform of  $A$  and  $\tilde{B}$  is the Fourier transform of  $B$ . Note that the partial derivatives with respect to  $x$  and  $y$  have been eliminated by this conversion; this is because  $\mathcal{F}\{f'(r)\} = 2\pi i f \tilde{f}$  [114]. Also note that these equations represent a physical system; therefore negative spatial frequencies must also be considered.

Eq. 5.7 can be solved numerically by splitting the left- and right-hand sides of the equations. For now, assume that the right-hand side of the equations are equal to zero. The first equation then simplifies to

$$2\pi i \tilde{A}(f_x k_{p,x} + f_y k_{p,y}) + k_{p,z} \frac{\partial \tilde{A}}{\partial z} = 0, \tag{5.8}$$

which is a differential equation with a solution of the form  $h(z) = C_1 \exp(-iC_2 z)$ . Note that the second equation will have the same form. Of course, this solution is only valid for the case where the right-hand side of the coupled wave equations actually equals zero, but for small propagation steps this is almost valid and therefore the fields in Fourier space can be written as

$$\begin{aligned}\tilde{A}(f_x, f_y, z + \Delta z) &= \tilde{A}(f_x, f_y, z) \exp\left(-i \frac{2\pi}{k_{p,z}} (f_x k_{p,x} + f_y k_{p,y})\right) \\ \tilde{B}(f_x, f_y, z + \Delta z) &= \tilde{B}(f_x, f_y, z) \exp\left(-i \frac{2\pi}{\sigma_z} (f_x \sigma_x + f_y \sigma_y)\right)\end{aligned}\quad (5.9)$$

These equations represent propagation in the Fourier domain, similar to the propagation equations described in Chapter 2 for the beam propagation method. If the beams were propagating in a homogeneous media the fields in coordinate space would simply be the inverse Fourier transform of Eq. 5.9. However, it is necessary to include the right-hand side of the coupled wave equations at this point in order to conserve energy. Therefore the fields at the next propagation step are

$$\begin{aligned}A(x, y, z + \Delta z) &= \mathcal{F}^{-1} \left\{ \tilde{A}(f_x, f_y, z + \Delta z) \right\} - i\kappa e^{-i\varphi(x,y)} B(x, y, z) \Delta z \\ B(x, y, z + \Delta z) &= \mathcal{F}^{-1} \left\{ \tilde{B}(f_x, f_y, z + \Delta z) \right\} - i\kappa e^{i\varphi(x,y)} A(x, y, z) \Delta z\end{aligned}\quad (5.10)$$

Note that these equations do not strictly conserve energy. This is because this method splits the propagation and the energy conservation into two discrete steps which is generally unphysical. However, by choosing small propagation steps this approximation is reasonable. A propagation step of 100 nm for instance conserves energy to within 0.01%. Thus this method can approximate the field distributions of the transmitted and diffracted waves.

### 5.3 Diffraction with Binary Phase Encoding

From Eq. 5.10 it is possible to calculate the intensity and phase distribution of the diffracted beam when a binary phase profile has been encoded into the grating by the appropriate phase mask. Remember that the phase mask provides the local phase change at the recording wavelength which for all results presented here is 325 nm, the emission wavelength of a He-Cd laser. If the reconstruction wavelength is the same as the recording wavelength then as previously discussed the diffracted beam will have the same phase profile. However, the case of interest is when the reconstruction wavelength is far from the recording wavelength.

To examine this, two cases will be simulated here: the case where there is a binary step in the  $x$ -direction (the grating phase discontinuity is parallel to the fringes, with the grating oriented as in Fig. 5.3) and the  $y$ -direction (the discontinuity is perpendicular to the fringes). In both cases the probe beam wavelength is 1064 nm and the grating period is 8  $\mu\text{m}$ . This grating period is rather large compared to most gratings, but by choosing this period the half angle of interference is minimized, in keeping with the assumption that the phase distribution recorded in the grating is approximately the same as the phase mask. Further, the simulated sample is 2 mm thick to help ensure that there is almost no  $z$ -dependence of the phase discontinuity. The propagation step size is 100 nm and the resolution in coordinate space is 3  $\mu\text{m}$  with a grating aperture of 200 mm.

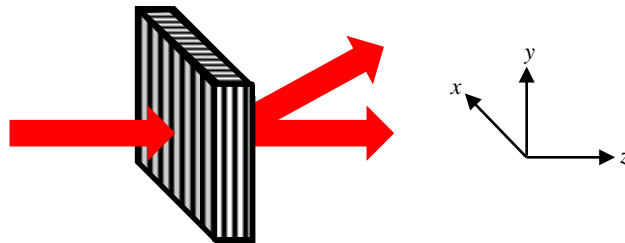


Figure 5.3: Orientation of the holographic phase masks used throughout this chapter. The incident, transmitted, and diffracted beams all lie within the  $x$ - $z$  plane.

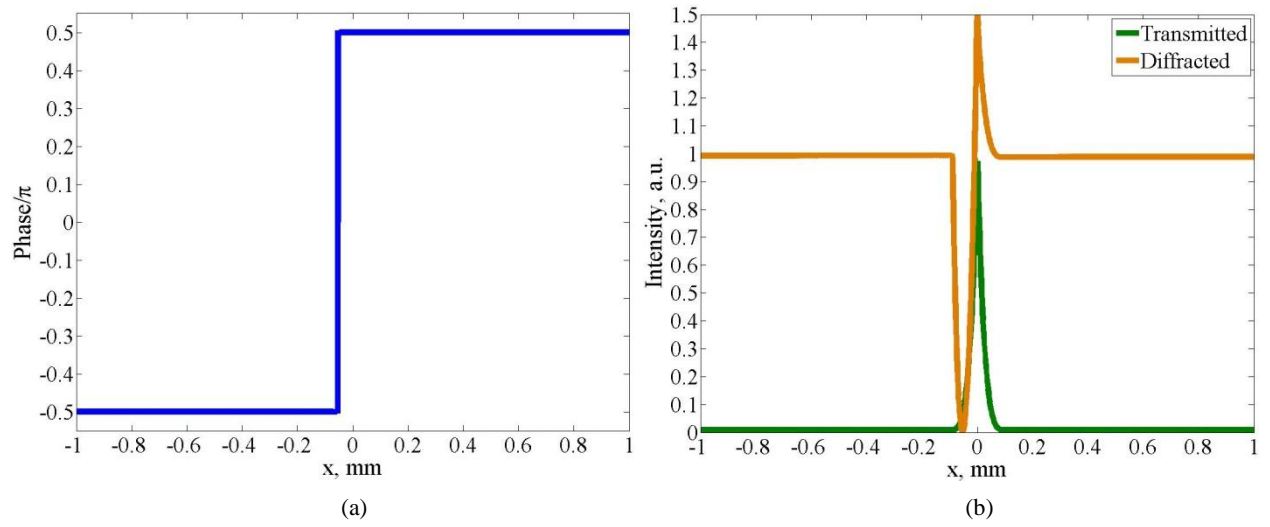


Figure 5.4: (a) Phase distribution of the diffracted beam in the presence of a binary shift in the grating phase along the  $x$ -axis and (b) the intensity distributions of the transmitted and diffracted beams.

This is a very large aperture but in these simulations the incident beam is assumed to be a plane wave in order to more easily illustrate the features in the intensity profiles. As the discrete Fourier transform assumes that a given function is periodic over a certain interval [115], this large grating aperture ensures that any interference effects at the boundary of the sample window do not have any effect at the center of the grating where the phase discontinuity is located. The refractive index modulation in these simulations is 250 ppm, which for a homogenous grating gives a diffraction efficiency of 99.13% at the Bragg angle for a 1064 nm beam.

Fig. 5.4 shows the intensity and phase profiles of the diffracted beam after propagating through the grating when the grating phase discontinuity is along the  $x$ -axis. As seen in Fig. 5.4a the phase profile of the diffracted beam is exactly the binary phase distribution that was encoded by the phase mask at the recording wavelength (the center of the profile is shifted to the left due to the diffracted beam, which is the  $-1$  order, propagating in that direction). Thus a holographic phase mask can be used for any incident beam which can satisfy the Bragg condition to provide the phase profile encoded in the original phase mask to the diffracted beam. Fig. 5.4b shows that

the diffracted profile (which is taken immediately after propagating through the grating) has a similar intensity distribution as the binary phase mask discussed in Chapter 2. This may be partially due to the propagation through a thick media as with the volume phase mask, but notice also that in that region there is some energy which is transmitted. This is of course caused by the grating phase discontinuity, where the incident beam will be slightly deviated from the Bragg condition. This deviation however only results in a small degradation in diffraction efficiency; for the large uniform wave considered here the overall diffraction efficiency is 99.10%, nearly identical to the diffraction efficiency of a homogenous grating. For smaller beams the overall diffraction efficiency decreases by up to a few percent. However, this decrease is on the whole very small and so it can be concluded that a binary phase shift along the  $x$ -axis does not noticeably affect the diffraction efficiency while providing the same phase distribution at the reconstruction wavelength as the phase mask does at the recording wavelength.

If the phase shift of the grating is along the  $y$ -axis then a somewhat different diffraction profile is observed, as seen in Fig. 5.5. As seen in Fig. 5.5a the phase profile is again the binary phase profile that was encoded by the phase mask at the recording wavelength.

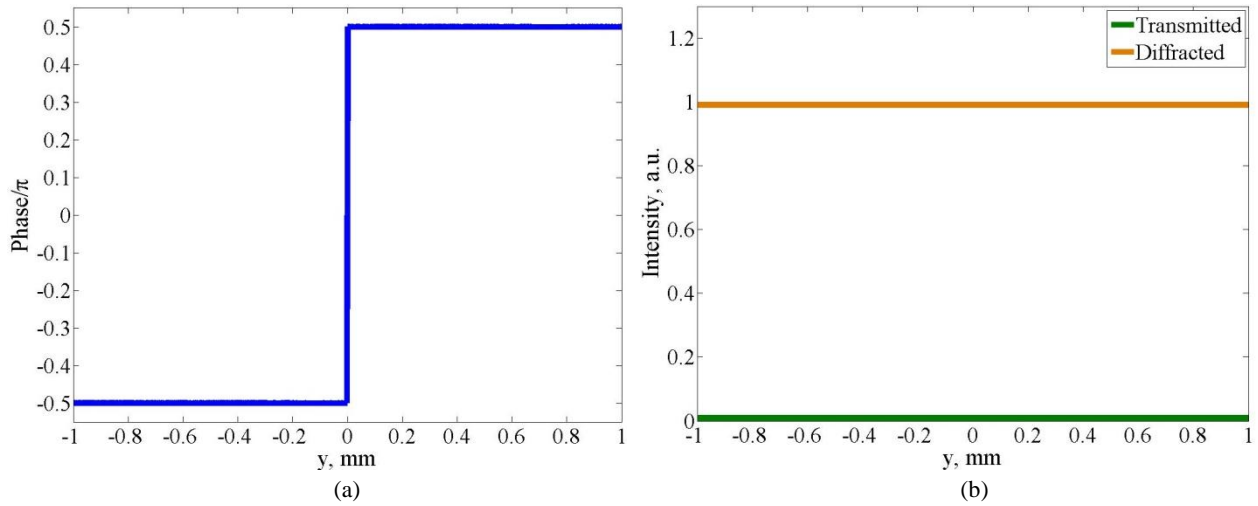


Figure 5.5: (a) Phase distribution of the diffracted beam in the presence of a binary shift in the grating phase along the  $y$ -axis and (b) the intensity distributions of the transmitted and diffracted beams.

Since the probe beam does not have a  $y$ -component to its wavevector the discontinuity is located precisely along the  $y$ -axis. However, as seen in Fig. 5.5b, the intensity profiles of the transmitted and diffracted beams are identical to the profiles expected of a homogenous grating, where the local ratio of the diffracted power to the incident power equals the overall diffraction efficiency of 99.12%. Given the 0.01% uncertainty due to lack of complete conservation of energy in this numerical approach it can be concluded that the diffraction efficiency in this case is identical to that of a homogenous grating. Also, unlike the case where there is a grating phase discontinuity along the  $x$ -axis, this diffraction efficiency is the same regardless of the beam size. This difference between cases comes about because the incident beam does not have a  $y$ -component to its wavevector. Therefore only a single infinitesimal line encounters the phase discontinuity and at no point in the grating will a given ray in the probe beam actually cross the discontinuity; either the ray is always on one side of the discontinuity or the other, and so it will always diffract in the same manner as a homogenous grating, acquiring the local grating phase. Therefore if the incident beam does not have a wavevector component along the direction of the phase discontinuity the grating will have the same diffraction efficiency as a homogenous grating while acquiring the local phase distribution of the phase mask placed in the holographic system.

To experimentally verify these simulations, holograms of a four-sector mode converting mask (chosen to give a binary phase shift along the  $x$ - and  $y$ -axes in a single element) were recorded in 1.97 mm PTR samples using the configuration shown in Fig. 5.6, where a four-sector mode converting mask designed for the recording wavelength of 325 nm was placed in one arm of the setup. This configuration, where the recording setup is converted to a Mach-Zehnder-type interferometer was chosen to best match the assumption that the phase profile of the holographic mask is the same as the phase mask placed into one arm.



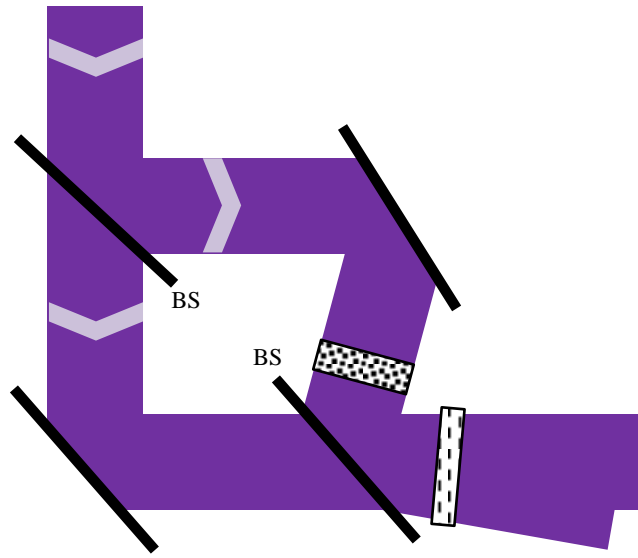


Figure 5.6: Mach-Zehnder configuration for recording large-period gratings with binary phase encoding.

As stated before, for this assumption to be valid the half angle of interference should be minimized. The Mach-Zehnder interferometer can achieve arbitrarily large periods while only rotating a mirror by a small amount since the interferometer is inherently designed to provide a nearly zero-fringe (infinite period) interference pattern. If large periods are desired in a setup similar to the setup shown in Fig. 5.1 the recording arms will need to be very long, which is impractical in terms of space requirements and further increases the chances of air fluctuations distorting the recording profile.

A further consideration is the phase mask itself. It is very likely that any given phase mask will not only introduce a local phase change but also diffract some of the transmitted light and for binary masks this is guaranteed. The diffracted beam, while not really changing its phase profile, will have a noticeable difference in its intensity profile. As seen in Fig. 5.7 diffraction from the four-sector phase mask results in regions of low intensity near the phase transition regions.

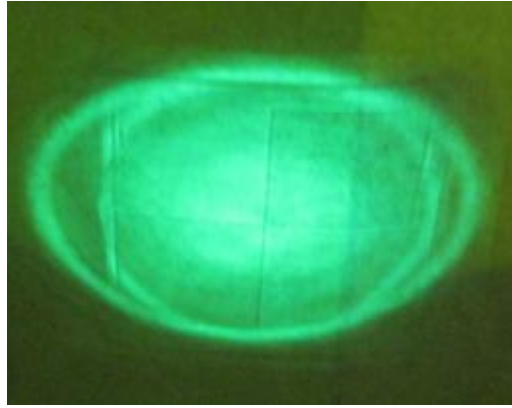


Figure 5.7: Image of overlapped recording beams on luminescent paper with a four-sector mode converting mask in one arm of the system. Note the cross pattern in the middle of the beams; this is due to diffraction from the transition regions of the phase mask in the object beam. Because the intensities of the recording beams are reduced along the cross only a very weak grating can form.

Because there is very low intensity the grating strength near that region will be very low, creating a dead space where a significant fraction of the energy of a probe beam will merely be transmitted. As a dead space is undesirable it is best to place the phase mask as close to the sample as possible so that the dead space is minimized. The Mach-Zehnder setup is the preferred setup since the sample can be placed immediately before the second beam splitter, whereas in the other setup the sample must be placed far enough away that the reference beam does not partially pass through the phase mask. In both cases however the diffraction problem can be avoided through the use of one-to-one imaging of the phase mask onto the sample provided space allows for an imaging system.

To record a holographic phase mask the PTR sample the object and reference beam were first aligned to produce a zero fringe on a screen. This guaranteed that the beams were propagating collinearly after the second beam-splitter and that there was a large region of overlap to record a grating. The mirror in the object beam (the right mirror in Fig. 5.6) was then rotated by  $0.931^\circ$  using an RV120HAT computer-controlled rotation stage (Newport) to create a fringe pattern with an  $8\text{ }\mu\text{m}$  period, chosen to match the period used in the simulations. As this

generally resulted in a reduced region of overlap the second beam-splitter was translated without rotation until full overlap was achieved in the plane of interference. Using a reduced beam intensity to prevent premature exposure the sample was placed in the plane of interference and rotated until the normal of the sample bisected the interference angle of the object and reference beams to produce a grating without any tilt. To check that the normal to the sample bisected the object and reference beams note that part of the reference beam reflected from the first surface of the sample into the object arm and vice versa. This created a Sagnac interferometer with an output visible in the unused port of the first beam-splitter. If the sample was properly aligned a zero-fringe pattern was observed there. The four-sector phase mask was then placed in the object beam, positioned such that the center of the cross seen in Fig. 5.7 was located at the center of the beam, and rotated until the reflection from the first surface aligned with the position of the interference pattern in the output port of the first beam-splitter. After increasing the beam intensity to full power a hologram of the phase mask was then recorded for 700 s, providing the standard dosage for a grating. The sample was then baked following the standard development procedure using a 510° bake temperature for the sodium fluoride nucleation.

After recording the holographic phase mask the diffracted beam was first examined at 632.8 nm in the near field (within the first 20 cm after the holographic mask) in order to determine whether there is any difference in the diffracted profile between the discontinuity oriented parallel to the fringes and the discontinuity oriented perpendicular to the fringes. As shown in Fig. 5.8, when observing the diffracted beam on a screen close to the grating the diffracted beam contains a smaller transition region when the phase discontinuity is along the  $y$ -axis than when the phase discontinuity is along the  $x$ -axis.

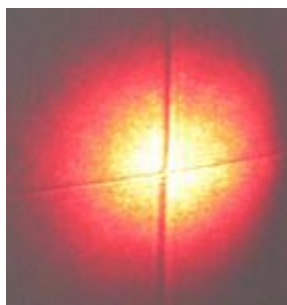


Figure 5.8: Diffracted beam after passing through a holographic phase mask encoded with a four-sector mode converter. This image was taken when the diffracted beam had propagated 7 cm after the mask, and the horizontal line is clearly narrower than the vertical line. Though it was not possible to take an image of the beam closer to the mask, a visual inspection of the beam on a screen brought to within 0.5 cm of the mask showed that the horizontal line is invisible at this distance while the vertical line was the same size as that shown in the above image.

In fact, as the screen is moved to immediately after the sample the horizontal transition region disappears while the vertical transition region remains approximately the same size, which is consistent with the simulation results.

The diffraction efficiency of the diffracted beam when centered on the cross was initially 30-40% weaker than the beam when centered on just a single quadrant where the grating is homogenous. This is due primarily to the combination of the dead space created when recording the phase mask and the small beam size (3 mm), resulting in a significant fraction of power not being diffracted at all. When the original phase mask in the holographic setup was adjusted to minimize the distance between the phase mask and the recording sample this discrepancy dropped to a 7% difference. Part of this difference is due to the residual dead space during recording, but most of it is due to the expected decrease in efficiency when there is a phase discontinuity along the  $x$ -axis. This was verified by shifting the beam so that there was only a phase discontinuity along the  $y$ -axis; in this configuration the diffraction efficiency was nearly identical to the diffraction efficiency of a single quadrant. Thus the experimental observations are in excellent agreement with the simulations.

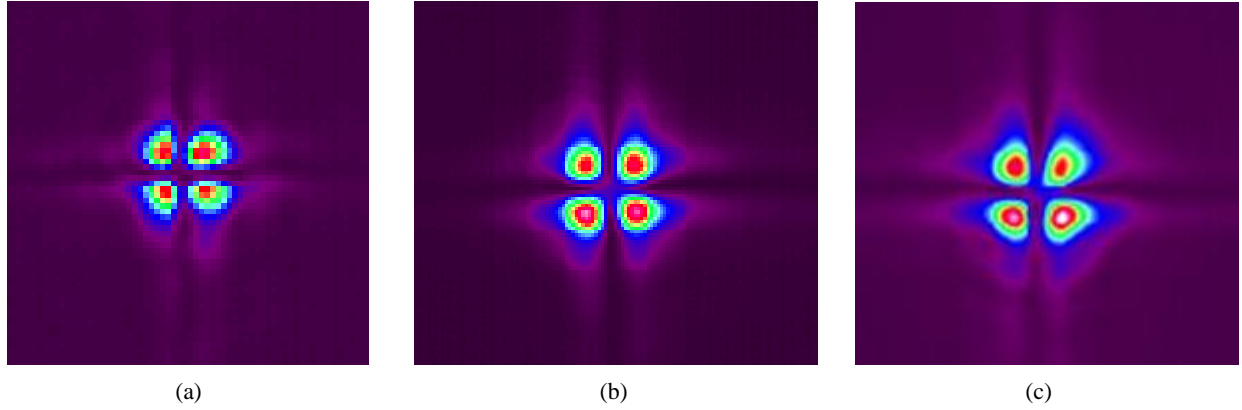


Figure 5.9: Far field profile of the diffracted beam from a four-sector holographic phase mask at (a) 632.8 nm, (b) 975 nm, and (c) 1064 nm. The sizes shown here are not to scale.

The diffracted beam was then examined in the far field (achieved by focusing the beam with a 500 mm lens) at multiple wavelengths in the visible and the infrared regions using a 3 mm probe beam to determine the wavelength dependence of mode conversion. As shown in Fig. 5.9, in all cases the diffracted profile exhibited the same four-lobed pattern. The profiles in Fig. 5.9 are very similar to the far field profiles of the four-sector mask shown in Fig. 2.13, indicating that there is a mode converting element encoded into the volume grating.

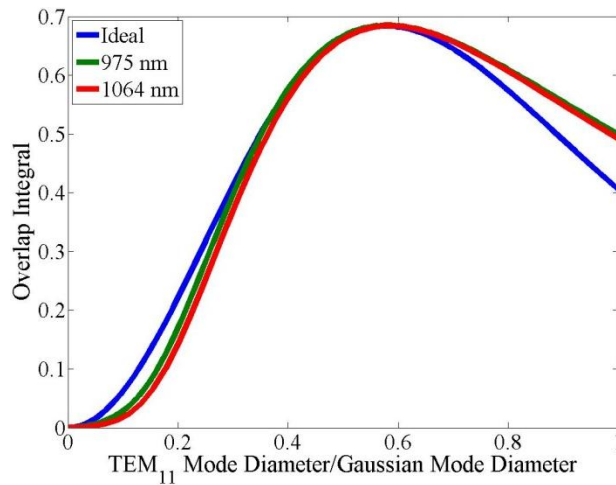


Figure 5.10: Overlap integral of the diffracted beam with the  $TEM_{11}$  mode at 975 nm and 1064 nm. There is not a perfect overlap with the ideal binary phase mask, indicating that the holographic phase profile is not a perfect binary profile. However, the conversion efficiency profiles at 975 nm and 1064 nm are nearly identical, indicating that the phase profile recorded can be extracted at any wavelength which can satisfy the Bragg condition.

In order to quantify the conversion efficiency into the  $\text{TEM}_{11}$  mode the overlap integral (Eq. 2.15) was calculated for the diffracted beam at 975 nm and 1064 nm in the same manner as the transmitted beam was calculated for the phase masks in Chapter 2. As shown in Fig. 5.10 the overlap integral at both wavelengths shows fairly good agreement with the curve predicted for a perfect binary phase mask. Because there is some noticeable discrepancy between the experimental curves and the ideal curve it can be concluded that the phase profile encoded into the volume grating was not a perfect binary profile. However, of greater importance is the fact that the curve at 975 nm is nearly identical to the curve at 1064 nm. Therefore the phase profile which is encoded into the holographic phase mask can be extracted by any probe beam which can satisfy the Bragg condition of the grating, in contrast to the monochromatic nature of the original phase mask used to record the hologram. It should be noted that while the phase profiles are identical, the diffraction efficiencies are not since the diffraction efficiency of a volume grating is wavelength-dependent, as is shown in Eq. 4.8.

The mode converting ability of the phase masks is of course not limited to converting a Gaussian beam to a higher order mode; it is also possible to convert from a higher order mode to a Gaussian profile. To demonstrate this, two 4-sector mode converting holographic phase masks were aligned so that a 3 mm Gaussian beam at 1064 nm was incident on the first mask and the diffracted (converted) beam from this mask was incident on the second converter. This doubly converted beam was then focused by a 500 mm lens to achieve the far field profile. As shown in Fig. 5.11a, the far field profile is a Gaussian spot with some low-energy wings. Cross sections of the beam, shown in Fig. 5.11b and 5.11c, were fitted with Gaussian functions to determine the size of the main spot relative to a diffraction-limited spot.

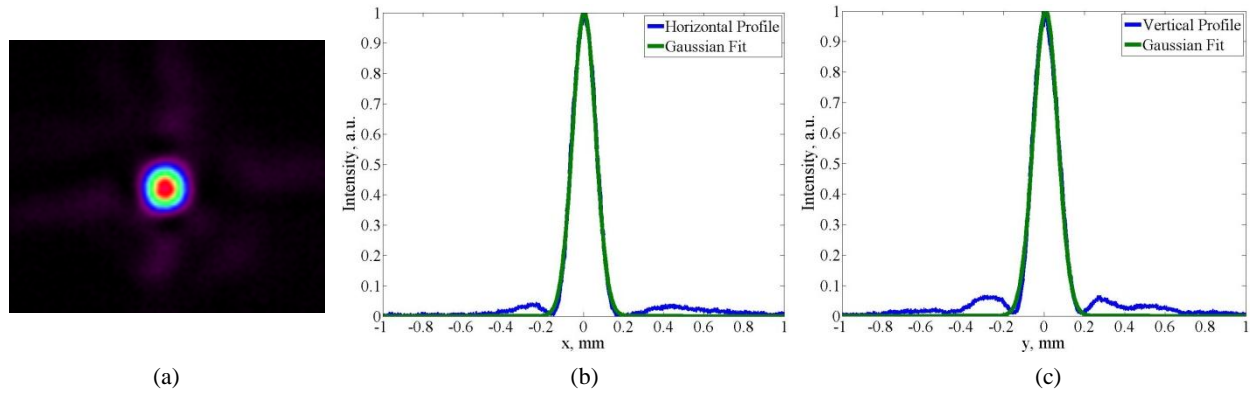


Figure 5.11: (a) Far field profile of a beam converted from a higher order mode to a Gaussian profile. (b) Horizontal and (c) vertical cross-sections of the beam indicate that the main spot has a near-diffraction-limited Gaussian profile.

The fits indicate that the spot size along the  $x$ -axis is  $228 \mu\text{m}$ , nearly identical to the diffraction-limited spot size of  $226 \mu\text{m}$ , while the spot size along the  $y$ -axis is  $240 \mu\text{m}$ , which is close to diffraction-limited. The wings are caused by the finite transition regions at the boundary between the different grating phases and can be reduced by reducing the size of the transition regions in the original phase mask used for recording as well as placing the phase mask closer to the sample during recording.

#### 5.4 Multiplexed Mode-Converting Masks

Having demonstrated that the holographic phase masks will reproduce the desired phase distribution in the diffracted beam with comparable diffraction efficiency as a homogenous grating, consider now the case where multiple gratings are multiplexed in a single element. Ideally these can be used in a system whereby changing the angle of incidence the multiplexed mask will switch from one mode converting element to another without cross-talk. Multiplexing of homogenous volume Bragg gratings has been demonstrated in the literature for use in beam combining [109-112], and multiplexing of complex holograms in spatial light modulators or in thin films for use at the same wavelength as the recording wavelength has been demonstrated for

use as a multiplexer/demultiplexer [116-119], and so by combining these techniques it is expected that a multiplexed holographic phase mask will exhibit both the mode conversion properties of complex holograms while achieving nearly 100% diffraction efficiency, similar to a Bragg grating.

To create a multiplexed holographic phase mask each grating profile was recorded sequentially using the same alignment techniques described previously to produce a single grating. During the first iteration the PTR sample was aligned in the same configuration as before and a hologram of the four-sector mask was recorded using an exposure time of 320 s, providing a dosage of approximately half the standard dosage for a grating. This reduction in exposure time is to ensure that after recording the second grating there will be no points close to saturation in the refractive index profile. The phase mask was then removed from the system and the sample rotated by  $5^\circ$ . The second exposure recorded a traditional Bragg grating with an exposure time of 350 s, again approximately half of the standard dosage of a regular grating. The extra 30 seconds is necessary to account for the change in absorption in the sample caused by the photoionization after the first exposure. The second hologram was chosen to be a traditional Bragg grating in order to verify that there is no cross-talk between the gratings, which can be easily determined by the profile of the diffracted beam when a probe beam satisfies the Bragg condition for the homogenous grating.

After developing the element the far field profiles of the diffracted beam were observed by rotating to the relevant Bragg angle for a 975 nm beam wavelength and focusing the diffracted beam by a 500 mm lens. In the first case the probe beam was shifted off-center so that there was only a phase discontinuity along the y-axis, and in the second case the incident beam was centered on the crossed discontinuity.



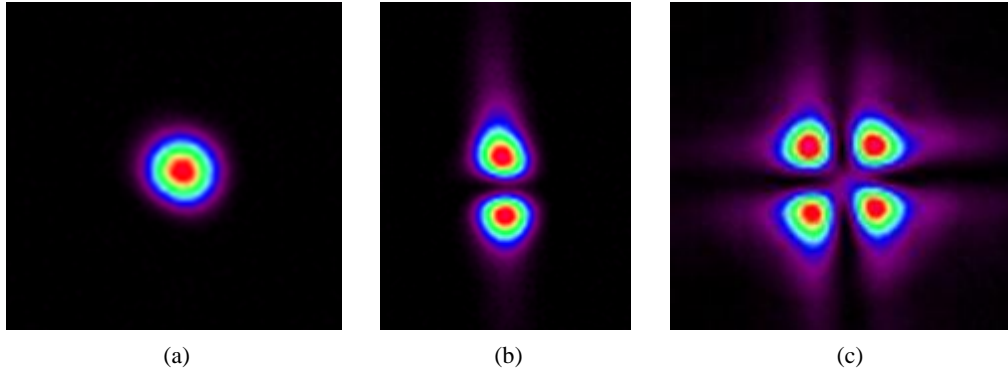


Figure 5.12: Far field profile of the beam diffracted from a multiplexed holographic phase mask when satisfying the Bragg condition for (a) a homogenous grating, (b) a two-sector mode converter, and (c) a four-sector mode converter.

As seen in Fig. 5.12 the far field profiles are exactly the profiles expected if there were only a single grating structure recorded in the sample. Cross-sections of the diffracted beam when satisfying the Bragg condition for the homogenous grating show that the diffracted spot size is identical to the spot size of a diffraction-limited beam, and no wings or other artifacts are observed. Therefore there is no cross-talk between the multiplexed grating structures. The diffraction efficiencies are also consistent with the assumption of no cross-talk: the diffraction efficiency of the homogenous grating when the probe beam is centered on the cross is 81.6% and the diffraction efficiency of the mode-converting grating is 76.2%. Likewise the diffraction efficiencies when the probe beam is shifted off-center are 88.7% and 89.3% respectively. Note that this grating is over-modulated so the higher diffraction efficiency when the probe beam is shifted off-axis actually represents a decrease in refractive index modulation, which may be due to reduced beam intensity during recording.

## 5.5 Summary

Holographic phase masks offer a means to multiplex several phase masks into a single element without cross-talk between the elements. Unlike most complex holograms, binary

holographic phase masks provide an exact replication of the phase profile of the phase mask used during the holographic recording regardless of incident wavelength, provided that the incident angle of the probe beam is properly adjusted. These phase masks can be used to perform the same beam-shaping and mode converting tasks as a binary phase mask, such as converting from a Gaussian beam to a higher order mode and vice versa. In addition, because the holographic mask is in effect a volume Bragg grating, the diffraction efficiency can be adjusted to provide 100% of the energy in the diffracted order.

## CHAPTER 6: SUMMARY AND CONCLUSIONS

In this thesis volume phase elements recorded into PTR glass which provide the same phase profile as traditional phase masks has been demonstrated for the first time. Because these samples are thick however, a beam will propagate while gradually accumulating phase, resulting in a different field distribution upon transmission from the phase mask than the field distribution seen with traditional thin film masks. In the very near field these differences may be significant, but in the far field these differences are negligible, resulting in beam profiles and mode conversion efficiencies identical to those produced by traditional masks. Therefore volume phase elements may be used in similar setups as conventional phase masks, but may also be used in high power systems due to the phase structure being a bulk recording inside glass as opposed to a surface recording.

To create arbitrary phase profiles in thick photosensitive glass plates a new type of amplitude mask, the probabilistic amplitude mask, was created. This mask, by utilizing the diffraction that occurs in the contact copy method, can produce phase elements such as a spiral phase mask with good fidelity. Probabilistic masks are most effective when the pixel size is small, as this increases the diffracted spot size and thus more accurately represents a grayscale profile. However, there are some limitations; probabilistic masks cannot accurately recreate elements which contain high spatial frequencies, such as Fresnel lenses, which results in a decrease in efficiency. This is however a result of using the contact copy method to create phase masks; the phase profile created by a probabilistic mask is very similar to the phase profile recorded by an ideal grayscale amplitude mask. Thus, the probabilistic amplitude mask can be used to create the same phase elements as a grayscale amplitude mask at a fraction of the cost.

Volume phase mask technology is useful in systems where aberrations are present, as aberrations do not generally have high spatial frequency content and therefore there is very little degradation of the phase profile when probabilistic masks are used. When recording holographic elements such as volume Bragg gratings, aberrations in the recording beams can severely degrade the recorded pattern. In the case of a reflecting Bragg grating, aberrations on the order of a wave are sufficient to alter the resonant wavelength, wash out side lobes and lower diffraction efficiency. Removing such aberrations requires either very high quality optics or some form of aberration correction such as aberration-correcting volume phase masks that can be tailored to selectively alter one or more aberrations in a system.

The utility of the phase masks can be further extended by multiplexing multiple phase masks into a single element by creating holograms of the phase masks. By proper alignment during recording it is possible to create multiplexed holographic phase masks which have no cross-talk between them. Binary holographic phase masks offer a wider range of applications than binary phase masks because regular volume phase masks are inherently monochromatic. However, holographic phase masks can provide the same phase profile to any beam that can satisfy the Bragg condition, extending the range of accepted wavelengths into the hundreds of nanometers. Holographic phase masks can be used in the same systems as regular phase masks and mode conversion from a Gaussian beam to higher order modes and vice versa has been demonstrated here.

Future work includes expanding the applications of volume phase masks, such as creating Gaussian to top-hat beam shapers. Furthermore, the applications of volume phase masks in resonators will be considered, especially as pertaining to developing lasers providing a single higher order output. Holographic phase masks may also be used in more advanced systems such

as performing simultaneous beam combining and mode conversion in a single element and in systems requiring a demultiplexer for modal analysis.

## **APPENDIX: MATLAB CODE FOR COMPUTER SIMULATIONS**

### A.1 Code for Propagating a Beam Through a Thick Medium

This code simulates a beam passing through a thick phase mask with a step function in the refractive index profile by using the beam propagation method. It will iteratively calculate the beam profile throughout the depth of the sample and after propagating a given distance after the sample and provide the average absolute difference (see Eq. 2.7) between the beam after accumulating phase with the thick mask and a beam which has accumulated phase with an infinitely thin mask.

```
lambda=632.8E-6; %wavelength in mm
k0=2*pi/lambda;
xstep=0.0001; %grid size in mm, this determines the lateral resolution of the simulation
z1=transpose(0.01:0.01:2); %thickness of sample in mm
z2=transpose(0:0.1:1000); %propagation distance after the sample
w=transpose(0.25:0.25:2); %radius of gaussian beam illuminating the sample

x=transpose(-50:xstep:50);
xp1=transpose((1/xstep)/2*linspace(0,1,floor(size(x,1)/2)));
xp2=transpose((1/xstep)/2*linspace(-1,0,ceil(size(x,1)/2)));
xp=[xp1;xp2];
Abs_Diff=zeros(size(z2,1),size(w,1)); %absolute mean difference, sum(|x-y|)/n
for countw=1:size(w,1)
    error=1E+15;
    error2=error;
    for count=1:size(x,1)
        if abs(x(count,1)-w(countw,1))<error
            right_index=count;
            error=abs(x(count,1)-w(countw,1));
        end
        if abs(x(count,1)+w(countw,1))<error2
            left_index=count;
            error2=abs(x(count,1)+w(countw,1));
        end
    end
    for countt=1:size(z1,1)
        steps=z1(countt,1)/.001;
        dz=z1(countt,1)/steps;
        deltan=-lambda/(2*z1(countt,1))*1; %this determines the refractive index step
```

```

E=ones(size(x));
for count=1:size(x,1)
    E(count,1)=exp(-x(count,1)^2/w(countw,1)^2);
end

n_prof=zeros(size(x)); %refractive index profile of the sample
for count=1:size(n_prof,1)
    if x(count,1)<0
        n_prof(count,1)=1.5;
    else
        n_prof(count,1)=1.5+deltan;
    end
end

% For comparison a distance z2 after the sample
for count=1:steps
    E2=fft(E)/size(x,1);
    for count2=1:size(xp,1)
        E2(count2,1)=E2(count2,1)*exp(-1i*xp(count2,1)^2*dz/(2*k0));
    end
    E=ifft(E2)*size(x,1);
    for count2=1:size(x,1)
        E(count2,1)=E(count2,1)*exp(-1i*k0*n_prof(count2,1)*dz);
    end
end
E_aftersample=E;
E_pma=ones(size(n_prof)); %ideal phase mask approximation field
for count=1:size(n_prof,1)
    E_pma(count,1)=exp(-1i*k0*n_prof(count,1)*z1(countt,1))*...
    exp(-x(count,1)^2/w(countw,1)^2);
end

for countz2=1:size(z2,1)
    E2=fft(E_aftersample)/size(x,1);
    E_pma2=fft(E_pma)/size(x,1);
    for count2=1:size(xp,1)
        E2(count2,1)=E2(count2,1)*exp(-1i*xp(count2,1)*z2(countz2,1)/(2*k0));
        E_pma2(count2,1)=E_pma2(count2,1)*...
        exp(-1i*xp(count2,1)*z2(countz2,1)/(2*k0));
    end
    E=ifft(E2)*size(x,1);
    E_pma2=ifft(E_pma2)*size(x,1);
    I=abs(E).^2;
    I_pma=abs(E_pma2).^2;
end

```



```

%figure,plot(x,I,x,I_pma) %enable this command to plot the beams at a given
                        %propagation distance after the sample

difference=0;
counter=0;
for count=left_index:right_index
    difference=difference+abs(I(count,1)-I_pma(count,1));
    counter=counter+1;
end
Abs_Diff(countz2,countw)=difference/counter;
end
end
end
data=[z2 Abs_Diff];
save('filename.txt','data','-ascii');
figure,plot(z2,Abs_Diff)

```

## A.2 Code to Calculate the Phase Profile of a Vortex Recorded with a Probabilistic Mask

This code will calculate the phase profile produced by a probabilistic mask designed to create an optical vortex. Here the code is broken into three steps: the first step calculates the probabilistic amplitude mask used to create the spiral phase profile. The second step calculates the intensity profile at a single wavelength using Eq. 3.10-3.12. The final step integrates these profiles into a single element taking into account the relative absorption of the glass and spectral brightness of the recording lamp. A similar code can be used to calculate the profile for a Fresnel lens.

### *A.2.1 Step 1*

```
step=0.001; %size of pixels in mm
maxr=3; %radius of SPP in mm
x=transpose(-maxr:step:maxr);
y=x;

phase=zeros(size(x,1),size(y,1)); %phase at each point in the SPP
for count=1:size(x,1)
    for count2=1:size(y,1)
        phase(count,count2)=atan2(y(count2,1),x(count,1))+pi; %vortex phase
    end
end
% contour(phase,'fill','on')
phase=phase/max(max(phase));
phase=phase.^(1/2);

mask=zeros(size(phase));
for count=1:size(x,1)
    for count2=1:size(y,1)
        num=unifrnd(0,1);
        if num<=phase(count,count2)
            mask(count,count2)=1;
        end
    end
end
save('Probabilistic Mask Filename.txt','mask','-ascii')
```

### A.2.2 Step 2

```
n=1.53; %refractive index of glass at lambda;
r_fiber=2.5; %radius of output fiber from the lamp
f_collimator=100; %focal length of collimating lens in mm
z=1; %distance into the PTR sample in mm

step=0.001; %size of mask pixels in mm
maxr=0.5; %radius of SPP in mm
interp=2; %number of points that represent a single pixel

x=transpose(-maxr:step:maxr);
y=x;

x2=transpose(linspace(-maxr,maxr,size(x,1)*interp)); %stretched x axis
y2=x2;

for Index=1:31
    wav=300+Index-1;
    lambda=wav*1E-6; %wavelength in air in mm

    Mask=importdata('Probabilistic Mask Filename.txt');

    Mask_Fill=zeros(size(y2,1),size(x2,1));
    for count=1:size(x2,1)
        for count2=1:size(y2,1)
            if (floor(count/interp)<size(x,1)) && (floor(count2/interp)<size(y,1))
                Mask_Fill(count2,count)=Mask(floor(count2/interp)+1,floor(count/interp+1));
            elseif (floor(count/interp)==size(x,1)) && (floor(count2/interp)<size(y,1))
                Mask_Fill(count2,count)=Mask(floor(count2/interp)+1,floor(count/interp));
            elseif (floor(count/interp)<size(x,1)) && (floor(count2/interp)==size(y,1))
                Mask_Fill(count2,count)=Mask(floor(count2/interp),floor(count/interp+1));
            elseif (floor(count/interp)==size(x,1)) && (floor(count2/interp)==size(y,1))
                Mask_Fill(count2,count)=Mask(floor(count2/interp),floor(count/interp));
            end
        end
    end
    clear Mask

    for count=1:size(x2,1)
        Mask_Fill(:,count)=Mask_Fill(:,count)*exp(1i*pi/(lambda*n*z)*x2(count,1)^2);
    end
    for count2=1:size(y2,1)
        Mask_Fill(count2,:)=Mask_Fill(count2,:)*exp(1i*pi/(lambda*n*z)*y2(count2,1)^2);
    end
end
```

```

profile=fftshift(fft2(Mask_Fill));
clear Mask_Fill
profile=abs(profile).^2;
profile=profile/max(max(profile));

x3=transpose(lambda*z*n*1/(2*(x2(size(x2,1),1)-x2(size(x2,1)-1,1)))*linspace(-1,1,size(x2,1)));
y3=x3;

x0=transpose(0:0.05:r_fiber);
y0=x0;

profile2=zeros(size(profile));
for count=1:size(x0,1)
    for count2=1:size(y0,1)
        if x0(count,1)^2+y0(count2,1)^2<=r_fiber^2
            error_x=1E+15;
            error_y=error_x;
            error_x2=error_x;
            error_y2=error_x;
            for count3=1:size(x3,1)
                if abs(x3(count3,1)-x0(count,1)*z/f_collimator)<error_x
                    temp_x=count3;
                    error_x=abs(x3(count3,1)-x0(count,1)*z/f_collimator);
                end
                if abs(x3(count3,1)+x0(count,1)*z/f_collimator)<error_x2
                    temp_x2=count3;
                    error_x2=abs(x3(count3,1)+x0(count,1)*z/f_collimator);
                end
                if abs(y3(count3,1)-y0(count2,1)*z/f_collimator)<error_y
                    temp_y=count3;
                    error_y=abs(y3(count3,1)-y0(count2,1)*z/f_collimator);
                end
                if abs(y3(count3,1)+y0(count2,1)*z/f_collimator)<error_y2
                    temp_y2=count3;
                    error_y2=abs(y3(count3,1)+y0(count2,1)*z/f_collimator);
                end
            end
        end

        if rem(size(x3,1),2)==1
            temp_x=temp_x-((size(x3,1)-1)/2+1);
            temp_y=temp_y-((size(y3,1)-1)/2+1);
            temp_x2=temp_x2-((size(x3,1)-1)/2+1);
            temp_y2=temp_y2-((size(y3,1)-1)/2+1);
        else
            temp_x=temp_x-size(x3,1)/2;

```

```

    temp_y=temp_y-size(y3,1)/2;
    temp_x2=temp_x2-size(x3,1)/2;
    temp_y2=temp_y2-size(y3,1)/2;
end

if temp_x>=0 && temp_y>=0

profile2(temp_y+1:size(profile,1),temp_x+1:size(profile,2))=profile2(temp_y+1:size(profile,1),t
emp_x+1:size(profile,2))+profile(1:(size(profile,1)-temp_y),1:(size(profile,2)-temp_x));
elseif temp_x<0 && temp_y>=0

profile2(temp_y+1:size(profile,1),1:size(profile,2)+temp_x)=profile2(temp_y+1:size(profile,1),1
:size(profile,2)+temp_x)+profile(1:(size(profile,1)-temp_y),(-1*temp_x+1):size(profile,2));
elseif temp_x>=0 && temp_y<0

profile2(1:size(profile,1)+temp_y,temp_x+1:size(profile,2))=profile2(1:size(profile,1)+temp_y,t
emp_x+1:size(profile,2))+profile((-1*temp_y+1):size(profile,1),1:size(profile,2)-temp_x);
elseif temp_x<0 && temp_y<0

profile2(1:size(profile,1)+temp_y,1:size(profile,2)+temp_x)=profile2(1:size(profile,1)+temp_y,1
:size(profile,2)+temp_x)+profile((-1*temp_y+1):size(profile,1),(-1*temp_x+1):size(profile,2));
end

if temp_x2==temp_x && temp_y2==temp_y

else
    if temp_x2>=0 && temp_y2>=0

profile2(temp_y2+1:size(profile,1),temp_x2+1:size(profile,2))=profile2(temp_y2+1:size(profile,
1),temp_x2+1:size(profile,2))+profile(1:(size(profile,1)-temp_y2),1:(size(profile,2)-temp_x2));
elseif temp_x2<0 && temp_y2>=0

profile2(temp_y2+1:size(profile,1),1:size(profile,2)+temp_x2)=profile2(temp_y2+1:size(profile,
1),1:size(profile,2)+temp_x2)+profile(1:(size(profile,1)-temp_y2),(-
1*temp_x2+1):size(profile,2));
elseif temp_x2>=0 && temp_y2<0

profile2(1:size(profile,1)+temp_y2,temp_x2+1:size(profile,2))=profile2(1:size(profile,1)+temp_
y2,temp_x2+1:size(profile,2))+profile((-1*temp_y2+1):size(profile,1),1:size(profile,2)-
temp_x2);
elseif temp_x2<0 && temp_y2<0

profile2(1:size(profile,1)+temp_y2,1:size(profile,2)+temp_x2)=profile2(1:size(profile,1)+temp_
y2,1:size(profile,2)+temp_x2)+profile((-1*temp_y2+1):size(profile,1),(-
1*temp_x2+1):size(profile,2));

```

```

        end
    end
end
end
clear profile temp_x temp_y x0 y0
temp=max(max(profile2));
profile2=profile2/temp;

error=1E+15;
error2=error;
for count=1:size(x3,1)
    if abs(x3(count,1)+maxr)<error
        index_left=count;
        error=abs(x3(count,1)+maxr);
    end
    if abs(x3(count,1)-maxr)<error2
        index_right=count;
        error2=abs(x3(count,1)-maxr);
    end
end
x3=x3(index_left:index_right,1);
profile2=profile2(index_left:index_right,index_left:index_right);

save('Intensity profile at wavelength x.txt','profile2','-ascii');
save('Axis coordinates.txt','x3','-ascii');
end

```

### A.2.3 Step 3

```

%Relative spectral absorption. Wavelengths go from 300 to 330 nm
wav_eff=zeros(31,1);
wav_eff(1,1)=1.5888;
wav_eff(2,1)=1.62;
wav_eff(3,1)=1.645;
wav_eff(4,1)=1.6627;
wav_eff(5,1)=1.6736;
wav_eff(6,1)=1.6772;
wav_eff(7,1)=1.6717;
wav_eff(8,1)=1.6592;
wav_eff(9,1)=1.6384;
wav_eff(10,1)=1.6067;
wav_eff(11,1)=1.5683;
wav_eff(12,1)=1.5224;

```

```

wav_eff(13,1)=1.4704;
wav_eff(14,1)=1.4134;
wav_eff(15,1)=1.3517;
wav_eff(16,1)=1.2861;
wav_eff(17,1)=1.2177;
wav_eff(18,1)=1.1476;
wav_eff(19,1)=1.0785;
wav_eff(20,1)=1.0119;
wav_eff(21,1)=0.9426;
wav_eff(22,1)=0.8738;
wav_eff(23,1)=0.807;
wav_eff(24,1)=0.7428;
wav_eff(25,1)=0.6815;
wav_eff(26,1)=0.6224;
wav_eff(27,1)=0.5672;
wav_eff(28,1)=0.5156;
wav_eff(29,1)=0.4676;
wav_eff(30,1)=0.4237;
wav_eff(31,1)=0.3826;

```

%Relative intensities and spectral brightness from the lamp (here 300 nm has a relative intensity of 1, not including the lamp). In this formulation the final scaling factor is absorption\*relative %intensity\*spectral brightness from lamp

```

wav_eff(1,1)=wav_eff(1,1)*.92;
wav_eff(2,1)=wav_eff(2,1)*.986777*.98;
wav_eff(3,1)=wav_eff(3,1)*.973772*1.44;
wav_eff(4,1)=wav_eff(4,1)*.96098*1.57;
wav_eff(5,1)=wav_eff(5,1)*.948398*1.28;
wav_eff(6,1)=wav_eff(6,1)*.936021*1.28;
wav_eff(7,1)=wav_eff(7,1)*.923845*1.28;
wav_eff(8,1)=wav_eff(8,1)*.911867*1.28;
wav_eff(9,1)=wav_eff(9,1)*.900082*1.28;
wav_eff(10,1)=wav_eff(10,1)*.888487*1.57;
wav_eff(11,1)=wav_eff(11,1)*.877078*2.22;
wav_eff(12,1)=wav_eff(12,1)*.865852*3.59;
wav_eff(13,1)=wav_eff(13,1)*.854804*5.62;
wav_eff(14,1)=wav_eff(14,1)*.843932*4.84;
wav_eff(15,1)=wav_eff(15,1)*.833233*8.37;
wav_eff(16,1)=wav_eff(16,1)*.822702*8.63;
wav_eff(17,1)=wav_eff(17,1)*.812338*7.32;
wav_eff(18,1)=wav_eff(18,1)*.802136*5.88;
wav_eff(19,1)=wav_eff(19,1)*.792094*5.23;
wav_eff(20,1)=wav_eff(20,1)*.782208*4.71;
wav_eff(21,1)=wav_eff(21,1)*.772476*4.31;
wav_eff(22,1)=wav_eff(22,1)*.762895*4.25;

```

```

wav_eff(23,1)=wav_eff(23,1)*.753462*4.05;
wav_eff(24,1)=wav_eff(24,1)*.744175*3.9;
wav_eff(25,1)=wav_eff(25,1)*.73503*3.79;
wav_eff(26,1)=wav_eff(26,1)*.726025*3.92;
wav_eff(27,1)=wav_eff(27,1)*.717158*3.92;
wav_eff(28,1)=wav_eff(28,1)*.708425*3.92;
wav_eff(29,1)=wav_eff(29,1)*.699825*3.92;
wav_eff(30,1)=wav_eff(30,1)*.691356*3.92;
wav_eff(31,1)=wav_eff(31,1)*.683013*4.44;

for count=1:31
    wav=300+count-1;
    temp_profile=importdata('Intensity profile at wavelength x.txt');
    temp_coord=importdata('Axis coordinates.txt');

    temp_profile=wav_eff(count,1)*temp_profile;

    if count==1
        profile=temp_profile;
        x=temp_coord;
    elseif size(profile,1)==size(temp_profile,1)
        profile=profile+temp_profile;
    elseif size(profile,1)>size(temp_profile,1)
        temp2=100*ones(size(profile));
        for count2=1:size(temp_profile,1)
            for count3=1:size(temp_profile,2)

temp2(round(count2*size(profile,1)/size(temp_profile,1)),round(count3*size(profile,2)/size(temp
p_profile,2)))=temp_profile(count2,count3);
                end
            end
            for count2=1:size(temp2,1)
                for count3=1:size(temp2,2)
                    if temp2(count2,count3)==100 && temp2(count2,1)<100
                        temp2(count2,count3)=1/2*(temp2(count2,count3-1)+temp2(count2,count3+1));
                    end
                end
            end
            for count2=1:size(temp2,1)
                for count3=1:size(temp2,2)
                    if temp2(count2,count3)==100
                        temp2(count2,count3)=1/2*(temp2(count2-1,count3)+temp2(count2+1,count3));
                    end
                end
            end
        end
    end
end

```



```

    profile=profile+temp2;
else
    temp2=100*ones(size(temp_profile));
    for count2=1:size(profile,1)
        for count3=1:size(profile,2)

temp2(round(count2*size(temp_profile,1)/size(profile,1)),round(count3*size(temp_profile,2)/size(profile,2)))=profile(count2,count3);
            end
        end
        for count2=1:size(temp2,1)
            for count3=1:size(temp2,2)
                if temp2(count2,count3)==100 && temp2(count2,1)<100
                    temp2(count2,count3)=1/2*(temp2(count2,count3-1)+temp2(count2,count3+1));
                end
            end
        end
        for count2=1:size(temp2,1)
            for count3=1:size(temp2,2)
                if temp2(count2,count3)==100
                    temp2(count2,count3)=1/2*(temp2(count2-1,count3)+temp2(count2+1,count3));
                end
            end
        end
        profile=temp2+temp_profile;
        x=temp_coord;
    end
end
clear temp_profile temp_coord
temp=max(max(profile));
profile=profile/temp;
profile=profile(130:1873,130:1873);
profile=profile-min((min(profile)));
profile=profile/max(max(profile));
x=x(130:1873,1);
y=x;

%taking into account the nonlinearity of the refractive index change
for count=1:size(profile,1)
    for count2=1:size(profile,2)

profile(count,count2)=880*profile(count,count2)*3.3375/(3.76+profile(count,count2)*3.3375);
        end
    end
temp=max(max(profile));

```

```
profile=profile/temp;  
  
figure,contour(x,y,profile,512,'fill','on')  
xlabel('x, mm')  
ylabel('y, mm')
```

### A.3 Code for Calculating the Spectral Response of a Grating in the Presence of Aberrations

This code calculates the spectral response of a grating at every single point across the grating aperture for every single wavelength near the Bragg condition in the presence of a set amount of aberrations. In order to find the overall spectral response it is necessary to integrate these spectra together using Eq. 4.24.

% The following calculations assume everything is given in waves %

```
theta=17.1857*pi/180; %ideal half angle of interference of two beams in rad
n=1.53; %refractive index of the recording medium at the recording wavelength
n_b=1.48; %refractive index of the recording medium at the bragg wavelength
R_rec=12.5*1E+6; %radius of the recording beam aperture in nm
k=2*pi*n/325; %wavenumber of the recording beams in the material (in nm^-1)
z=transpose(-3:0.025:3)*1E+6; %propagation distance in nm
z(121,1)=0;

t=5.5*1E+6; %thickness of the grating in nm (as seen by the probe beam)
N_sec=100; %number of sections the grating will be divided into for the transfer matrix
theta_test=0; %angle of the test beam inside the grating in rad (theta_x_probe_beam)
theta_test_y=pi/2; %y angle of probe beam (equals pi/2 for a horizontal beam)
dn=200*1E-6; %RIM
pol=1; %polarization factor; equals 1 for TE and 2*cos(theta_test) for TM
% for 99.4 % reflectance, use dn = 200*1E-6, t = 5.5*1E+6, N_sec=100
% for 68.5 % reflectance, use dn = 20*1E-6, t=20*1E+6, N_sec=500

%Peak-to-valley Zernike Terms Using Noll notation
z_ptv_1=zeros(16,1); %Zernike polynomial coefficients in waves for beam 1
z_ptv_1(1,1)=0; %piston
z_ptv_1(2,1)=0; %tilt x
z_ptv_1(3,1)=0; %tilt y
z_ptv_1(4,1)=1; %defocus
z_ptv_1(5,1)=0; %0 deg primary astigmatism
z_ptv_1(6,1)=0; %45 deg primary astigmatism
z_ptv_1(7,1)=0; %primary coma x
z_ptv_1(8,1)=0; %primary coma y
z_ptv_1(9,1)=0; %30 deg trefoil
z_ptv_1(10,1)=0; %0 deg trefoil
z_ptv_1(11,1)=0; %primary spherical

z_ptv_2=zeros(16,1); %Zernike polynomial coefficients in waves for beam 2
```

```

z_ptv_2(1,1)=0; %piston
z_ptv_2(2,1)=0; %tilt x
z_ptv_2(3,1)=0; %tilt y
z_ptv_2(4,1)=1; %defocus
z_ptv_2(5,1)=0; %0 deg primary astigmatism
z_ptv_2(6,1)=0; %45 deg primary astigmatism
z_ptv_2(7,1)=0; %primary coma x
z_ptv_2(8,1)=0; %primary coma y
z_ptv_2(9,1)=0; %30 deg trefoil
z_ptv_2(10,1)=0; %0 deg trefoil
z_ptv_2(11,1)=0; %primary spherical

% Construction of Wavefront
r_aperture=1; %radius of the aperture which is always <=1
x=transpose(-r_aperture:0.002:r_aperture); %normalized dimension for the Zernike polynomials
y=x;
W_1=zeros(size(y,1),size(x,1)); %Wavefront of beam 1. Note that in this Cartesian system, the
wavefront will be slightly off for values of x and y larger than sqrt(x^2+y^2)=1
W_2=W_1;

%This calculates the wavefront at z=0
for count=1:size(y,1)
    for count2=1:size(x,1)
        W_1(count,count2)=z_ptv_1(1,1)+z_ptv_1(2,1)*x(count2,1)+z_ptv_1(3,1)*y(count,1)+...
            z_ptv_1(4,1)*(2*(x(count2,1)^2+y(count,1)^2)-1)+z_ptv_1(5,1)*(x(count2,1)^2-
y(count,1)^2)+...

z_ptv_1(6,1)*2*x(count2,1)*y(count,1)+z_ptv_1(7,1)*(3*x(count2,1)^3+3*x(count2,1)*y(count
,1)^2-2*x(count2,1))+...
            z_ptv_1(8,1)*(3*x(count2,1)^2*y(count,1)+3*y(count,1)^3-
2*y(count,1))+z_ptv_1(9,1)*(x(count2,1)^3-3*x(count2,1)*y(count,1)^2)+...
            z_ptv_1(10,1)*(3*x(count2,1)^2*y(count,1)-
y(count,1)^3)+z_ptv_1(11,1)*(6*(x(count2,1)^4+y(count,1)^4-x(count2,1)^2-
y(count,1)^2)+12*x(count2,1)^2*y(count,1)^2-1);
        W_2(count,count2)=z_ptv_2(1,1)+z_ptv_2(2,1)*-
1*x(count2,1)+z_ptv_2(3,1)*y(count,1)+...
            z_ptv_2(4,1)*(2*(x(count2,1)^2+y(count,1)^2)-1)+z_ptv_2(5,1)*(x(count2,1)^2-
y(count,1)^2)+...
            z_ptv_2(6,1)*2*-1*x(count2,1)*y(count,1)+z_ptv_2(7,1)*(3*-1*x(count2,1)^3+3*-
1*x(count2,1)*y(count,1)^2-2*-1*x(count2,1))+...
            z_ptv_2(8,1)*(3*x(count2,1)^2*y(count,1)+3*y(count,1)^3-
2*y(count,1))+z_ptv_2(9,1)*(-1*x(count2,1)^3-3*-1*x(count2,1)*y(count,1)^2)+...
            z_ptv_2(10,1)*(3*x(count2,1)^2*y(count,1)-
y(count,1)^3)+z_ptv_2(11,1)*(6*(x(count2,1)^4+y(count,1)^4-x(count2,1)^2-
y(count,1)^2)+12*x(count2,1)^2*y(count,1)^2-1);
    end
end

```

```

end
end

W_1=2*pi/k*W_1; %converts to distance scale
W_2=2*pi/k*W_2;
x=x*R_rec; %conversion of nondimensionalized axis into actual axis
y=x;
for count=1:size(z,1)
    %this calculates the wavevectors for the two beams in the
    %grating-centered coordinate system
    W_1b=W_1;

    [del_x1,del_y1]=gradient(W_1b,x(2,1)-x(1,1),y(2,1)-y(1,1));
    kx1=-1*del_x1*cos(theta)+sin(theta)*ones(size(del_x1));
    ky1=-1*del_y1;
    kz1=cos(theta)*ones(size(del_x1))-sin(theta)*del_x1;
    clear del_x1 del_y1 W_1b W_1

    W_2b=W_2;

    [del_x2,del_y2]=gradient(W_2b,x(2,1)-x(1,1),y(2,1)-y(1,1));
    kx2=-1*del_x2*cos(-1*theta)+sin(-1*theta)*ones(size(del_x2));
    ky2=-1*del_y2;
    kz2=cos(-1*theta)*ones(size(del_x2))-sin(-1*theta)*del_x2;
    clear del_x2 del_y2 W_2b W_2

    for count2=1:size(kx1,1)
        for count3=1:size(kx1,2)
            temp=k/sqrt(kx1(count2,count3)^2+ky1(count2,count3)^2+kz1(count2,count3)^2);
            kx1(count2,count3)=kx1(count2,count3)*temp;
            ky1(count2,count3)=ky1(count2,count3)*temp;
            kz1(count2,count3)=kz1(count2,count3)*temp;

            temp=k/sqrt(kx2(count2,count3)^2+ky2(count2,count3)^2+kz2(count2,count3)^2);
            kx2(count2,count3)=kx2(count2,count3)*temp;
            ky2(count2,count3)=ky2(count2,count3)*temp;
            kz2(count2,count3)=kz2(count2,count3)*temp;

        end
    end

    theta_eff_x=atan(kx1((size(x,1)-1)/2+1,(size(x,1)-1)/2+1)/kz1((size(x,1)-1)/2+1,(size(x,1)-1)/2+1));
    x=x/cos(theta_eff_x);
    %theta_eff_y=acos(ky1((size(x,1)-1)/2+1,(size(x,1)-1)/2+1)/k);

```

```

%y=y/sin(theta_eff_y)
error1=1E+10;
error2=1E+10;
for count2=1:size(x,1)
    if abs(x(count2,1)-(-1*t/2))<error1
        pos1=count2;
        error1=abs(x(count2,1)-(-1*t/2));
    end
    if abs(x(count2,1)-t/2)<error2
        pos2=count2;
        error2=abs(x(count2,1)-t/2);
    end
end
x_shift=z(count,1)*tan(theta_eff_x);
%y_shift=z(count,1)*cot(theta_eff_y);

error1=1E+10;
error2=1E+10;
for count2=1:size(x,1)
    %for beam 1 which propagates left to right (+theta)
    if abs(x(count2,1)-x_shift)<error1
        shift1=count2-(size(kx1,2)-1)/2+1;
        error1=abs(x(count2,1)-x_shift);
    end
    %for beam 2 which propagates right to left (-theta)
    if abs(x(count2,1)+x_shift)<error2
        shift2=count2-(size(kx2,2)-1)/2+1;
        error2=abs(x(count2,1)+x_shift);
    end
end

x=x(pos1:pos2,1);
kx1=kx1(:,pos1-shift1:pos2-shift1);
ky1=ky1(:,pos1-shift1:pos2-shift1);
kz1=kz1(:,pos1-shift1:pos2-shift1);

kx2=kx2(:,pos1-shift2:pos2-shift2);
ky2=ky2(:,pos1-shift2:pos2-shift2);
kz2=kz2(:,pos1-shift2:pos2-shift2);

Period=zeros(size(kz1));
tilt_x=Period;
tilt_y=tilt_x;

for count2=1:size(y,1)

```

```

for count3=1:size(x,1)
    Period(count2,count3)=2*pi/sqrt((kx1(count2,count3)-
kx2(count2,count3))^2+(ky1(count2,count3)-ky2(count2,count3))^2+(kz1(count2,count3)-
kz2(count2,count3))^2);
    tilt_x(count2,count3)=atan((kx1(count2,count3)-
kx2(count2,count3))/(kz1(count2,count3)-kz2(count2,count3)))-pi/2; %the -pi/2 is for the probe
beam propagating along the x-axis
    tilt_y(count2,count3)=acos((ky1(count2,count3)-
ky2(count2,count3))/sqrt((kx1(count2,count3)-kx2(count2,count3))^2+(ky1(count2,count3)-
ky2(count2,count3))^2+(kz1(count2,count3)-kz2(count2,count3))^2));
end
end

clear kx1 kx2 ky1 ky2 kz1 kz2

res_wave_ideal=2*n_b*2*pi/(2*k*sin(theta));
lambda=transpose((res_wave_ideal-
0.0005*res_wave_ideal):(0.0000025*res_wave_ideal):(res_wave_ideal+0.0005*res_wave_ideal)
);
refl_point=zeros(size(y,1),size(lambda,1)); %reflectance at each y point at a specific z plane
for a given lambda
t_i=t/N_sec; %thickness of each subpiece

for count2=1:size(y,1)
    temp=floor((pos2-pos1)/N_sec);
    Period2=zeros(N_sec,1);
    tilt_x2=Period2;
    tilt_y2=Period2;
    for count3=1:size(Period2,1)
        Period2(count3,1)=Period(count2,(count3-1)*temp+round(temp/2));
        tilt_x2(count3,1)=tilt_x(count2,(count3-1)*temp+round(temp/2));
        if tilt_x2(count3,1)<-pi/2
            tilt_x2(count3,1)=tilt_x2(count3,1)+2*pi;
        end
        if tilt_x2(count3,1)>pi/2 && tilt_x2(count3,1)<3*pi/2
            tilt_x2(count3,1)=pi-tilt_x2(count3,1);
        end
        tilt_y2(count3,1)=tilt_y(count2,(count3-1)*temp+round(temp/2));
    end

for count4=1:size(lambda,1)
    for count5=1:N_sec
        kappa=2*pi*dn/(2*pol*lambda(count4,1)*cos(theta_test));

```

```

        beta_Bragg=(2*pi/Period2(count5,1)-
cos(theta_test_y)*cos(tilt_y2(count5,1)))/(2*sin(theta_test_y)*sin(tilt_y2(count5,1))*cos(tilt_x2(
count5,1)-theta_test));
        dB=2*pi*n_b/lambda(count4,1)-beta_Bragg;
        gamma=sqrt(kappa^2-dB^2);
        if count5==1
            phase=0;
        else
            phase=phase+2*(2*pi/Period2(count5-1,1)-cos(theta_test_y)*cos(tilt_y2(count5-
1,1)))/(2*sin(theta_test_y)*sin(tilt_y2(count5-1,1))*cos(tilt_x2(count5-1,1)-theta_test))*t_i;
        end
        T11=(cosh(gamma*t_i)+1i*dB*sinh(gamma*t_i)/gamma)*exp(1i*t_i*beta_Bragg);
        T12=-kappa*t_i*sinh(gamma*t_i)*exp(-1i*(beta_Bragg*t_i+phase))/(gamma*t_i);
        T21=-kappa*t_i*sinh(gamma*t_i)*exp(1i*(beta_Bragg*t_i+phase))/(gamma*t_i);
        T22=(cosh(gamma*t_i)-1i*dB*sinh(gamma*t_i)/gamma)*exp(-1i*beta_Bragg*t_i);
        if count5==1
            T=[T11 T12;T21 T22];
        else
            T=T*[T11 T12;T21 T22];
        end
    end
    refl_point(count2,count4)=T(2,1)/T(1,1)*conj(T(2,1)/T(1,1));
end
end
save('Reflectance spectrum at every point in z-plane x.mat','refl_point');
end

```



#### A.4 Code to Calculate the Transmitted and Diffracted Profiles of a Holographic Phase Mask

This code calculates the transmitted and diffracted intensity distributions of a holographic phase mask immediately after propagating through the grating for the case where the binary phase discontinuity is along the  $x$ -axis. The total diffraction efficiency and energy conservation checks are also provided. This code can be easily extended to include phase discontinuities along the  $y$ -axis.

```
% This simulation only applies at Bragg condition

n=1.48; %background refractive index
k=2*pi*n/1064E-6; %wavenumber in mm^-1
RIM=250E-6; %refractive index modulation
z=2; %grating thickness in mm
Period=8.03627E-3; %grating period in mm
kappa=pi*RIM*k/(2*pi*n);
tilt=pi/2; %tilt of the grating, equals pi/2 for an untilted TBG
theta=tilt-acos((2*pi/Period)/(2*k)); %angle of incidence, rad

kpx=sin(theta);
kpz=cos(theta);
kdx=kpx-(2*pi/Period)/k*sin(tilt);
kdz=kpz-(2*pi/Period)/k*cos(tilt);
dz=0.0001; %step size in mm

x=transpose(linspace(-200,200,2^18));
q1=transpose(2*pi/(2*(x(2,1)-x(1,1)))*linspace(0,1,floor(size(x,1)/2)));
q2=transpose(2*pi/(2*(x(2,1)-x(1,1)))*linspace(-1,0,ceil(size(x,1)/2)));
q=[q1;q2];

phi=pi*heaviside(x);

A_old=ones(size(x));
B_old=zeros(size(phi));

energy_in_A=sum(abs(A_old).^2);

t=0;
while t<=z
    A_bar=fft(A_old)/size(A_old,1).*exp(-1i*q*kpx/kpz*dz);
```

```

A_new=ifft(A_bar)*size(A_old,1)-1i*kappa*dz*B_old.*exp(-1i*phi);

B_bar=fft(B_old)/size(B_old,1).*exp(-1i*q*kdx/kdz*dz);
B_new=ifft(B_bar)*size(B_old,1)-1i*kappa*dz*A_old.*exp(1i*phi);
A_old=A_new;
B_old=B_new;

t=t+dz;
end
clear A_old B_old A_bar B_bar
test=max(abs(A_new).^2+abs(B_new).^2);
test2=min(abs(A_new).^2+abs(B_new).^2);
figure,plot(x,abs(A_new).^2,x,abs(B_new).^2,x,abs(A_new).^2+abs(B_new).^2)
legend('Transmitted','Diffracted','Sum')
figure,plot(x,angle(B_new)./pi)
energy_out=sum(abs(A_new).^2+abs(B_new).^2);
energy_out_A=sum(abs(A_new).^2);
energy_out_B=sum(abs(B_new).^2);
diff_eff=energy_out_B/energy_in_A
energy=energy_out/energy_in_A

```

## REFERENCES

1. A. Castro, Y. Frauel, and B. Javidi, "Integral imaging with large depth of field using an asymmetric phase mask," *Optics Express* **15**, 10266-10273 (2007).
2. N. Caron and Y. Sheng, "Polynomial phase masks for extending the depth of field of a microscope," *Applied Optics* **22**, E39-E43 (2008).
3. H. Zhao, Y. Li, H. Feng, Z. Xu, and Q. Li, "Cubic sinusoidal phase mask: Another choice to extend the depth of field of incoherent imaging system," *Optics & Laser Technology* **42**, 561-569 (2010).
4. M. Shibuya, "Resolution enhancement techniques for optical lithography and optical imaging theory," *Optical Review* **4**, 151-160 (1997).
5. B. Javidi and J. Horner, "Optical pattern recognition for validation and security verification," *Optical Engineering* **33**, 1752-1756 (1994).
6. L. Neto and Y. Sheng, "Optical implementation of image encryption using random phase encoding," *Optical Engineering* **35**, 2459-2463 (1996).
7. C. Cheng, L. Lin, C. Wang, and C. Chen, "Optical joint transform encryption using binary phase difference key mask," *Physical Review* **12**, 367-371 (2005).
8. P. Kumar, J. Joseph, and K. Singh, "Impulse attack-free four random phase mask encryption based on a 4-f optical system," *Applied Optics* **48**, 2356-2363 (2009).
9. D. Rouan, P. Riaud, A. Boccaletti, Y. Clenet, and A. Labeyrie, "The four-quadrant phase-mask coronagraph. I. Principle," *Publications of the Astronomical Society of the Pacific* **112**, 1479-1486 (2000).
10. A. Boccaletti, P. Riaud, P. Baudoz, J. Baudrand, D. Rouan, D. Gratadour, F. Lacombe, and A. Lagrange, "The four-quadrant phase-mask coronagraph. IV. First light at the Very Large Telescope," *Publications of the Astronomical Society of the Pacific* **116**, 1061-1071 (2004).
11. E. Bloemhof, "Achromatic four-quadrant phase mask (FQPM) coronagraphy using natural beam splitter phase shifts," *Optics Express* **13**, 10055-10060 (2005).
12. C. Smelser, S. Mihailov, and D. Grobncic, "Rouard's method modeling of type I-IR fiber Bragg gratings made using an ultrafast IR laser and a phase mask," *J. Optical Society of America B* **23**, 2011-2017 (2006).

13. A. Basu and J. M. Ballantyne, "Random fluctuations in first-order waveguide grating filters," *Applied Optics* **18**, 2575-2579 (1979).
14. M. Moharam, T. K. Gaylord, G. T. Sincerbox, H. Werlich, and B. Yung, "Diffraction characteristics of photoresist surface-relief gratings," *Applied Optics* **23**, 3214-3220 (1984).
15. D. O'Shea, "Reduction of the zero-order intensity in binary Dammann gratings," *Applied Optics* **34**, 6533-6537 (1995).
16. A. Yan, L. Liu, E. Dai, J. Sun, and Y. Zhou, "Simultaneous beam combination and aperture filling of coherent laser arrays by conjugate Dammann gratings," *Optics Letters* **35**, 1251-1253 (2010).
17. L. Glebov, "Volume diffractive elements in photosensitive inorganic glass for beam combining," *Proc. Solid State and Diode Lasers Technical Review*, FA-5 (2001).
18. V. Smirnov, E. Flecher, L. Glebov, K. Liao, and A. Galvanauskas, "Chirped bulk Bragg gratings in PTR glass for ultrashort pulse stretching and compression," *Proc. Solid State and Diode Lasers Technical Review*, SS2-1 (2005).
19. J. Yang and M. Wang, "Analysis and optimization on single-zone binary flat-top beam shaper," *Optical Engineering* **42**, 3106-3113 (2003).
20. X. Huang, M. Wang, and C. Yu, "High-efficiency flat-top beam shaper fabricated by a nonlithographic technique," *Optical Engineering* **38**, 208-213 (1999).
21. M. Wang, C. Yu, and A. Varela, "Efficient pseudo-nondiffracting beam shaping using a quasicontinuous-phase diffractive element," *Optical Engineering* **40**, 517-524 (2001).
22. J. Rosen, B. Salik, and A. Yariv, "Pseudo-nondiffracting beams generated by radial harmonic function," *J. Optical Society of America A* **12**, 2446-2457 (1995).
23. J. Rosen, B. Salik, and A. Yariv, "Pseudo-nondiffracting beams generated by radial harmonic function: erratum," *J. Optical Society of America A* **13**, 387 (1996).
24. W. Mohammed, M. Pitchumani, A. Mehta, and E. Johnson, "Selective excitation of the LP<sub>11</sub> mode in step index fiber using a phase mask," *Optical Engineering* **45**, 074602 (2006).
25. A. Shyouji, K. Kurihara, A. Otomo, and S. Saito, "Diffraction-grating-type phase converters for conversion of Hermite-Laguerre-Gaussian mode into Gaussian mode," *Applied Optics* **49**, 1513-1517 (2010).

26. M. Beesley and J. Castledine, "The use of photoresist as a holographic recording medium," *Applied Optics* **9**, 2720-2724 (1970).
27. J. G. Harris and M. Brandt, "Visualization of Nd:YAG laser beams using black PMMA," *Proceedings of Profiles of Industrial Research: Knowledge and Innovation*, 162-170 (2002).
28. J. A. Abdulnabi, T. A. Tawfiq, A. A. Al-Dergazly, Z. A. Taha, and K. I. Hajim, "Precise hole drilling in PMMA using 1064 nm diode laser CNC machine," *Advances in Materials Science and Engineering* **2011**, 137407 (2011).
29. M. J. Assael, S. Botsios, K. Gialou, and I. N. Metaxa, "Thermal conductivity of polymethyl methacrylate (PMMA) and borosilicate crown glass BK7," *International Journal of Thermophysics* **26**, 1595-1605 (2005).
30. S. N. Kasarova, N. G. Sultanova, C. D. Ivanov, and I. D. Nikolov, "Analysis of the dispersion of optical plastic materials," *Optical Materials* **29**, 1481-1490 (2007).
31. O. Ziemann, J. Krauser, P. E. Zamzow, and W. Daum, *POF Handbook: Optical Short Range Transmission Systems 2<sup>nd</sup> Ed.*, Springer, Berlin (2008).
32. W. F. Smith and J. Hashemi, *Foundations of Materials Science and Engineering 4<sup>th</sup> Ed.*, McGraw-Hill (2006).
33. B. Chang and C. Leonard, "Dichromated gelatin for the fabrication of holographic optical elements," *Applied Optics* **18**, 2407-2417 (1979).
34. Kirk-Othmer, *Food and Feed Technology Vol. 1*, Wiley (2007).
35. K. Buse, "Light-induced charge transport processes in photorefractive crystals II: Materials," *Applied Physics B* **64**, 391-407 (1997).
36. B. Sturman, M. Carrascosa, and F. Agullo-Lopez, "Light-induced charge transport in LiNbO<sub>3</sub> crystals," *Physical Review B* **78**, 245144 (2008).
37. M. Moharam and L. Young, "Reading and optical erasure of holograms stored by the photoelectric effect in lithium niobate," *Applied Optics* **17**, 2773-2778 (1978).
38. J. Lumeau, L. Glebova, V. Golubkov, E. D. Zanotto, and L. B. Glebov, "Origin of crystallization-induced refractive index changes in photo-thermo-refractive glass," *Optical Materials* **32**, 139-146 (2009).

39. L. B. Glebov, "Photochromic and photo-thermo-refractive (PTR) glasses," *Encyclopedia of Smart Materials*, John Wiley & Sons, NY, 770-780 (2002).
40. B. Anderson, S. Kaim, G. Venus, J. Lumeau, V. Smirnov, B. Zeldovich, and L. Glebov, "Forced air cooling of volume Bragg gratings for spectral beam combining," *Proceedings of SPIE* **8601**, 86013D (2013).
41. L. B. Glebov, "Kinetics modeling in photosensitive glass," *Optical Materials* **25**, 413-418 (2004).
42. J. Lumeau, L. Glebov, G. Souza, E. Zanotto, and L. Glebov, "Effect of cooling on the optical properties and crystallization of UV-exposed photo-thermo-refractive glass," *J. of Non-Crystalline Solids* **354**, 4730-4736 (2008).
43. J. Goodman, *Introduction to Fourier Optics 3rd Ed.*, Roberts & Company, Greenwood Village, CO (USA) (2005).
44. H. Kogelnik, "Coupled wave theory for thick volume holograms," *Bell System Tech. J.* **45**, 2909-2944 (1969).
45. R. Syms, *Practical Volume Holography*, Oxford University Press, Oxford (UK) (1990).
46. L. B. Glebov, J. Lumeau, S. Mokhov, V. Smirnov, and B. Ya. Zeldovich, "Reflection of light by composite volume holograms: Fresnel corrections and Fabry-Perot spectral filtering," *Journal of Optical Society of America A* **25**, 751-764 (2008).
47. J. Harvey, A. Krywonos, and D. Bugunovic, "Nonparaxial scalar treatment of sinusoidal phase gratings," *Journal of Optical Society of America A* **23**, 858-865 (2006).
48. M. G. Moharam and L. Young, "Criterion for Bragg and Raman-Nath diffraction regimes," *Applied Optics* **17**, 1757-1759 (1978).
49. M. G. Moharam, T. K. Gaylord, and R. Magnusson, "Criteria for Bragg regime diffraction by phase gratings," *Optics Communications* **32**, 14-18 (1980).
50. M. G. Moharam, T. K. Gaylord, and R. Magnusson, "Criteria for Raman-Nath regime diffraction by phase gratings," *Optics Communications* **32**, 19-23 (1980).
51. T. K. Gaylord and M. G. Moharam, "Analysis and applications of optical diffraction by gratings," *Proc. Of IEEE* **73**, 894-937 (1985).

52. T. Jääskeläinen and T. Hytonen, “Diffraction regimes of phase gratings,” *Optics Communications* **64**, 19-22 (1987).
53. J. Yang and N. Wang, “Analysis and optimization on single-zone binary flat-top beam shaper,” *Optical Engineering* **42**, 3106-3113 (2003).
54. N. Murakami, J. Nishikawa, K. Yokochi, M. Tamura, N. Baba, and L. Abe, “Achromatic eight-octant phase-mask coronagraph using photonic crystal,” *Astrophysical J.* **714**, 772-777 (2010).
55. P. Suresh, C. Mariyal, K. B. Rajesh, T. V. S. Pillai, and Z. Jaroszewicz, “Generation of a strong uniform transversely polarized non-diffracting beam using a high-numerical-aperture lens axicon with a binary phase mask,” *Applied Optics* **52**, 849-853 (2013).
56. J. Jarem and P. Banerjee, *Computational Methods for Electromagnetic and Optical Systems*, Marcel Dekker, Inc. NY (2000).
57. O. Efimov, L. Glebov, and H. Andre, “Measurement of induced refractive index in a photothermorefractive glass by a liquid-cell shearing interferometer,” *Applied Optics* **41**, 1864-1871 (2002).
58. L. Glebov and V. Smirnov, “Interaction of photo-thermo-refractive glass with nanosecond pulses at 532 nm,” *Proceedings of SPIE* **5273**, 396-401 (2004).
59. L. Dong, P. Yang, B. Xu, X. Lei, Y. Ning, W. Liu, and H. Yan, “High-order mode Laguerre-Gaussian beam transformation using a 127-actuator deformable mirror: numerical simulations,” *Applied Physics B* **104**, 725-733 (2011).
60. A. Yariv and P. Yeh, *Photonics: Optical Electronics in Modern Communications*, Oxford University Press (2007).
61. A. Jeffrey, *Handbook of Mathematical Formulas and Integrals*, Academic Press, San Diego CA (USA) (1995).
62. W. Beyer, *CRC Standard Mathematical Tables 28<sup>th</sup> Ed.*, CRC Press, Boca Raton FL (USA) (1987).
63. Dymax Corp., “Blue wave 200 version 1.1 operation manual,” (2006), available online at [www.dymax.com/pdf/manuals/man015\\_bluewave\\_200ce\\_ia\\_version\\_1.1.pdf](http://www.dymax.com/pdf/manuals/man015_bluewave_200ce_ia_version_1.1.pdf).
64. K. Reimer, H. J. Quenzer, M. Jürss, and B. Wagner, “Micro-optic fabrication using one-level gray-tone lithography,” *Proceedings of SPIE* **3008**, 279-288 (1997).

65. C. K. Wu, "Method of making high energy beam sensitive glasses," U.S. Patent, No. 5,078,771 (1992).
66. M. Christophersen, and B. F. Philips, "Gray-tone lithography using an optical diffuser and a contact aligner," *Applied Physics Letters* **92**, 194102 (2008).
67. Y.-T. Lu, C.-S. Chu, and H.-Y. Lin, "Characterization of the gray-scale photolithography with high-resolution gray steps for the precise fabrication of diffractive optics," *Optics Engineering* **43**, 2666–2670, (2004).
68. L. Mosher, C. Waits, B. Morgan, and R. Ghodzzi, "Double-exposure grayscale photolithography," *Journal of Microelectromechanical Systems* **18**, 308-315 (2009).
69. W. Däschner, P. Long, R. Stein, C. Wu, and S. H. Lee, "General aspheric refractive microoptics fabricated by optical lithography using a high energy beam sensitive glass gray-level mask," *Journal of Vacuum Science and Technology B* **14**, 3730 (1996).
70. T. Dillon, A. Sure, J. Murakowski, and D. Prather, "Continuous-tone grayscale mask fabrication using high-energy-beam-sensitive glass," *Journal of Micro/Nanolithography, MEMS, and MOEMS* **3**, 550-554 (2004).
71. C. F. Guo, S. Cao, P. Jiang, Y. Fang, J. Zhang, Y. Fan, Y. Wang, W. Xu, Z. Zhao, and Q. Liu, "Grayscale photomask fabricated by laser direct writing in metallic nano-films," *Optics Express* **17**, 19981 (2009).
72. K. Ladavac and D. Grier, "Microoptomechanical pumps assembled and driven by holographic optical vortex arrays," *Optics Express* **12**, 1144-1149 (2004).
73. S. Gröblacher, T. Jennewein, A. Vaziri, G. Weihs, and A. Zeilinger, "Experimental quantum cryptography with qutrits," *New Journal of Physics* **8**, 75 (2006).
74. I. Basistiy, V. A. Pas'ko, V. V. Slyusar, M. S. Soskin, and M. V. Vasnetsov, "Synthesis and analysis of optical vortices with fractional topological charge," *Journal of Applied Optics A* **6**, S166-S169 (2004).
75. H. Garcia-Gracia and J. Gutierrez-Vega, "Diffraction of plane waves by finite-radius spiral phase plates of integer and fractional topological charge," *Journal of Optical Society of America* **26**, 794-803 (2009).
76. C. Rotschild, S. Zommer, S. Moed, O. Hershcovitz, and S. Lipson, "Adjustable spiral phase plate," *Applied Optics* **43**, 2397-2399 (2004).



77. M. Prasciolu, F. Tamburini, G. Anzolin, E. Mari, M. Melli, A. Carpentiero, C. Barbieri, and F. Romanato, "Fabrication of a three-dimensional optical vortices phase mask for astronomy by means of electron-beam lithography," *Microelectronic Engineering* **86**, 1103-1106 (2009).
78. W. J. Lai, B. C. Lim, P. B. Phua, K. S. Tiaw, H. H. Teo, and M. H. Hong, "Generation of radially polarized with a segmented spiral varying retarder," *Optics Express* **16**, 15694-15699 (2008).
79. W. T. Welford, *Aberrations of Optical Systems*, Adam Hilger (IOP Publishing) , Bristol (UK) (1991).
80. C. K. Sieracki, C. G. Levey, and E. W. Hansen, "Simple binary optical elements for aberration correction in confocal microscopy," *Optics Letters* **20**, 1213-1215 (1995).
81. N. Chen, "Aberrations of volume holographic grating," *Optics Letters* **10**, 472-474 (1985).
82. Y. Suzaki, J. Mohri, K. Nakayama, M. Ando, K. Sakamoto, M. Yamauchi, Y. Mizutani, T. Yokouchi, and S. Ejima, "Effect of Spherical Aberration on Fabrication of Fiber Bragg Gratings," *Jap. J. Appl. Phys.* **45**, 5035-5038 (2006).
83. M. Ma, X. Wang, and F. Wang, "Aberration measurement of projection optics in lithographic tools based on two-beam interference theory," *Applied Optics* **45**, 8200-8208 (2006).
84. A. Siegman, "Analysis of laser beam quality degradation caused by quartic phase aberrations," *Applied Optics* **30**, 5893-5901 (1993).
85. B. Neubert and B. Eppich, "Influences on the beam propagation ratio M2," *Optics Communications* **250**, 241-251 (2005).
86. R. S. Sirohi, *Optical Methods of Measurement: Wholefield Techniques, 2nd Ed.*, CRC Press, Boca Raton FL (USA) (2009).
87. L. B. Glebov, J. Lumeau, S. Mokhov, V. Smirnov, and B. Ya. Zeldovich, "Reflection of light by composite volume holograms: Fresnel corrections and Fabry–Perot spectral filtering," *Journal of Optical Society America A* **25**, 751-764 (2008).
88. J. Wyant and K. Creath, "Basic wavefront aberration theory for optical metrology," in *Applied Optics and Optical Engineering Vol. XI*, R. Shannon and J. Wyant, Eds., Academic Press, 1-53 (1992).

89. R. J. Noll, "Zernike polynomials and atmospheric turbulence," *Journal of Optical Society of America* **66**, 207-211 (1976).
90. G. Dai, *Wavefront Optics for Vision Correction*, SPIE Press, Bellingham WA (USA) (2008).
91. A. Sevia, O. Andrusyak, I. Ciapurin, V. Smirnov, G. Venus, and L. Glebov, "Efficient power scaling of laser radiation by spectral beam combining," *Optics Letters* **33**, 384-386 (2008).
92. O. Andrusyak, V. Smirnov, G. Venus, V. Rotar, and L. Glebov, "Spectral combining and coherent coupling of lasers by volume Bragg gratings," *IEEE Journal of Selected Topics in Quantum Electronics* **15**, 344-353 (2009).
93. Z. Sun, Q. Li, H. Lei, Y. Hui, and M. Jiang, "Sub-nanosecond pulse, single longitudinal mode Q-switched Nd:YVO<sub>4</sub> laser controlled by reflecting Bragg gratings," *Optics & Laser Technology* **48**, 475-479 (2013).
94. D. Ott, V. Rotar, J. Lumeau, S. Mokhov, I. Divliansky, A. Rysanyanskiy, N. Vorobiev, V. Smirnov, C. Spiegelberg, L. Glebov, "Longitudinal mode selection in laser cavity by moiré volume Bragg grating," *Proceedings of SPIE* **8236**, 823621, (2012).
95. Lumeau, L. B. Glebov, and V. Smirnov, "Tunable narrowband filter based on a combination of Fabry–Perot etalon and volume Bragg grating," *Optics Letters* **31**, 2417-2419 (2006).
96. V. Smirnov, J. Lumeau, S. Mokhov, B. Ya. Zeldovich, and L. B. Glebov, "Ultrannarrow bandwidth moiré reflecting Bragg gratings recorded in photo-thermo-refractive glass," *Optics Letters* **35**, 592-594 (2010).
97. J. Lumeau, C. Koc, O. Mokhun, V. Smirnov, M. Lequime, and L. B. Glebov, "Single resonance monolithic Fabry–Perot filters formed by volume Bragg gratings and multilayer dielectric mirrors," *Optics Letters* **36**, 1773-1775 (2011).
98. T. Hieta, M. Vainio, C. Moser, and E. Ikonen, "External-cavity lasers based on a volume holographic grating at normal incidence for spectroscopy in the visible range," *Optics Communications* **282**, 3119–3123 (2009).
99. J. Saikawa, M. Fujii, H. Ishizuki, and T. Taira, "High-energy, narrow-bandwidth periodically poled Mg-doped LiNbO<sub>3</sub> optical parametric oscillator with a volume Bragg grating," *Optics Letters* **32**, 2996-2998 (2007).
100. M. Yamada and K. Sakuda, "Analysis of almost-periodic distributed feedback slab waveguides via a fundamental matrix approach," *Applied Optics* **26**, 3474-3478 (1987).

101. R. Ragazzoni, M. Tordi, and E. Diolaiti, "A fixed plate to remove spherical aberration in Rayleigh guide stars," *Optics Communications* **194**, 243-250 (2001).
102. R. Navarro, E. Moreno-Barriuso, S. Bará, and T. Mancebo, "Phase plates for wave-aberration compensation in the human eye," *Optics Letters* **25**, 236-238 (2000).
103. F. Vargas Martín, P. Prieto, and P. Artal, "Correction of the aberrations in the human eye with a liquid-crystal spatial light modulator: limits to performance," *Journal of the Optical Society of America A* **15**, 2552-2562 (1998).
104. T. Kelly and J. Munch, "Phase-aberration correction with dual liquid-crystal spatial light modulators," *Applied Optics* **37**, 5184-5189 (1998).
105. R. Dou and M. Giles, "Closed-loop adaptive-optics system with a liquid-crystal television as a phase retarder," *Optics Letters* **20**, 1583-1585 (1997).
106. G. Love, "Wave-front correction and production of Zernike modes with a liquid-crystal spatial light modulator," *Applied Optics* **7**, 1517-1524 (1997).
107. W. Cowan, M. Lee, B. Welsh, V. Bright, and M. Roggemann, "Optical phase modulation using a refractive lenslet array and microelectromechanical deformable mirror," *Optical Engineering* **37**, 3237-3247 (1998).
108. W. Sweatt, "Reduction of Zernike wavefront errors using a micromirror array," *Optical Engineering* **44**, 098001 (2005).
109. I. Divliansky, D. Ott, B. Anderson, D. Drachenberg, V. Rotar, G. Venus, and L. Glebov, "Multiplexed volume Bragg gratings for spectral beam combining of high power fiber lasers," *Proceedings of SPIE* **8237**, 823705 (2012).
110. C. A. Lu, A. Flores, E. Bochove, W. Roach, V. Smirnov, and L. Glebov, "Coherent beam combination of fiber laser arrays via multiplexed volume Bragg gratings," *CLEO: Science and Innovations*, OSA Technical Digest, CF2N.2 (2012).
111. A. Jain, C. Spiegelberg, V. Smirnov, L. Glebov, and E. Bochove, "Efficient coherent beam combining of fiber lasers using multiplexed volume Bragg gratings," *CLEO: Science and Innovations*, OSA Technical Digest, CF2N.8 (2012).
112. C. A. Lu, A. Flores, E. Bochove, W. Roach, V. Smirnov, and L. Glebov, "Active coherent superposition of five fiber amplifiers at 670W using multiplexed volume Bragg gratings," *Proceedings of SPIE* **8601**, 86011 (2013).

- 113. P. Hariharan, *Basics of Holography*, Cambridge University Press, Cambridge (UK) (2002).
- 114. B. V. Ramana, *Higher Engineering Mathematics*, Tata McGraw-Hill, New Delhi (India) (2007).
- 115. D. Sundararajan, *The Discrete Fourier Transform: Theory, Algorithms, and Applications*, World Scientific Publishing, Singapore (2001).
- 116. Y. Ishii and T. Kubota, "Wavelength demultiplexer in multimode fiber that uses optimized holographic optical elements," *Applied Optics* **32**, 4415-4422 (1993).
- 117. K. Aoki, A. Okamoto, Y. Wakayama, A. Tomita, and S. Honma, "Selective multimode excitation using volume holographic mode multiplexer," *Optics Letters* **38**, 769-771 (2013).
- 118. D. Flamm, C. Schulze, D. Naidoo, S. Schroter, A. Forbes, and M. Duparre, "All-digital holographic tool for mode excitation and analysis in optical fibers," *Journal of Lightwave Technology* **31**, 1023-1032 (2013).
- 119. Y. Wakayama, A. Okamoto, K. Kawabata, A. Tomita, and K. Sato, "Mode demultiplexer using angularly multiplexed volume holograms," *Optics Express* **21**, 012920 (2013).